Norwegian University of
Science and Technology

# Pressure Tolerant Power Electronics

**Øystein Holt**

Master of Science in Electric Power Engineering
Submission date: June 2009
Supervisor: Tore Marvin Undeland, ELKRAFT

Norwegian University of Science and Technology
Department of Electrical Power Engineering

# Problem Description

In the future, it is expected that oil and gas extraction will have to take place at greater depths than today. Beyond a certain depth, one will have to use pure subsea installations, that is, the extraction equipment will be placed on the seabed. To avoid expensive pressure vessels, it is interesting to investigate the possibility of exposing the power electronics equipment to the high ambient pressure at the bottom of the sea. The power electronics equipment is then placed in a container filled with dielectric oil, which has the same ambient pressure as the surrounding sea water.

The practical part of the project will emphasize laboratory testing of an IGBT module when submerged in dielectric oil. Submerging the IGBT module in oil may affect the operating behaviour of the device compared to when operating in normal environment. These differences should be investigated. It is of interest to investigate the thermal conditions for the device when it is submerged in oil. The theoretical part of the project will emphasize modelling the thermal characteristics under different operating conditions, also considering possible theoretical explanations for observed phenomena. Considerations regarding the stray inductance in the test setup should also be made.

Assignment given: 15. January 2009
Supervisor: Tore Marvin Undeland, ELKRAFT

# PREFACE

This is a report for the Master project in the 5$^{th}$ year of the Master programme of the department of Electric Power Engineering at NTNU. The project has a weight of 30 ECTS credits.

This report deals mostly with the thermal aspects of immersing an IGBT module in dielectric liquid. The module is tested in the active mode of operation to look at the thermal behaviour. Temperature sensors and thermocamera is used in order to document the temperature conditions. Attempts at making simple equivalents representing the thermal behaviour have been made.

In addition, the module has been immersed fully in oil during double-pulse and normal switching in order to compare with the switching in air that was performed in the autumn specialization project. The testing in oil represents a reference to possible future testing in a pressurized environment.

Simple models for some of the thermal behaviour were developed as thermal equivalent networks in a circuit simulator. Basic thermal behaviour was also studied using finite element methods in the software package COMSOL Multiphysics.

A brief literature study regarding the inductance considerations for the bus bar connections in the test setup was performed.

The work described in this report is a part of an ongoing research effort by SINTEF Energy Research to build knowledge about the pressurization of power electronics.

I would like to take this opportunity to thank the people that have helped me during this work:

Professor Tore Undeland who has been my supervisor.

Researchers Kjell Ljøkelsøy, Astrid Petterteig, Magnar Hernes, Riccardo Pittini and Stian Ingebrigtsen at SINTEF Energy Research.

Trondheim, 11.06.2009

……………………………………

Øystein Holt

NTNU
Norwegian University of
Science and Technology

NTNU
Norwegian University of Science and Technology

# SUMMARY


The thermal behaviour of an IGBT module was investigated, especially with respect to the module being immersed in dielectric oil. An equivalent thermal model was built using thermal transients and network synthesis. The thermal behaviour was further investigated using thermocamera measurements and simple finite element models.

Passive pressure testing of electronic components relevant for the test setup was performed. The testing showed no significant influence on the electrical behaviour of the components.

An IGBT module without gel covering the chips was switched while immersed in dielectric oil. The switching transients were compared to the case of a normal module switching in air. Only minor differences were found between the switching waveforms from the two cases.

A test was performed where water was added to the dielectric oil in order to reduce the breakdown voltage of the oil. No breakdown phenomena were observed for the voltages that were tested.

A brief litterature study regarding stray inductance considerations in the test setup was performed.

# TABLE OF CONTENTS

1 INTRODUCTION ..... 2
2 THEORY ..... 4
2.1 Principal operation of the IGBT ..... 4
2.2 Principal turn-on waveforms of the IGBT ..... 7
2.3 Principal turn-off waveforms of the IGBT ..... 8
3 DESCRIPTION OF TEST OBJECT ..... 9
3.1 IGBT module ..... 9
3.2 Dielectric oil ..... 10
4 THERMAL TESTING OF THE IGBT MODULE IN ACTIVE MODE OF OPERATION ..... 11
4.1 Description of the test setup and initial testing ..... 11
4.2 Active testing of module without gel in air ..... 14
4.3 Testing of module without gel in Midel 7131 ..... 19
4.4 Estimation of heat flow in the module ..... 20
4.5 Effects of movement of the oil ..... 22
5 THERMAL MODELING OF THE IGBT MODULE ..... 26
5.1 Modeling with thermal equivalent networks ..... 26
5.1.1 Basic theory ..... 26
5.1.2 Description of available methods for time constant extraction ..... 28
5.1.3 Extraction of the time constants for the cooling transient ..... 28
5.1.4 Foster thermal equivalent network construction ..... 30
5.1.5 Cauer thermal equivalent network construction by network synthesis ..... 31
5.1.6 Verification of the Cauer equivalent network ..... 33
5.2 Modeling in COMSOL Multiphysics ..... 35
5.2.1 Basic model ..... 35
5.2.2 Model with simple flow of cooling medium ..... 36
5.2.3 Stationary cooling medium ..... 40
6 THERMOCAMERA MEASUREMENTS ..... 42
6.1 Initial testing of the thermocamera ..... 42
6.2 Testing of IGBT module without heatsink ..... 43
6.3 Testing of IGBT module with heatsink ..... 44
7 STRAY INDUCTANCE CONSIDERATIONS IN THE TEST SETUP ..... 47
7.1 Background of inductance considerations ..... 47
7.2 Inductance calculation methods ..... 47
7.3 COMSOL Multiphysics modelling for assessment of stray inductance ..... 51
8 PASSIVE PRESSURE TESTING OF COMPONENTS ..... 56
8.1 Description of passive pressure testing ..... 56
8.2 Results from passive pressure testing ..... 57
9 SWITCHING OF OPEN MODULE IN OIL ..... 60
9.1 Description of test setup for double-pulse switching ..... 60
9.2 Description of double-pulse switching ..... 64
9.3 Description of test programme for double-pulse switching of open module in oil at 25 degrees Celsius ..... 65
9.4 Results from double-pulse switching in oil at 25 degrees Celsius ..... 65
9.6 Continuous switching ..... 69
9.6.1 Description of continuous switching ..... 69
9.6.2 Description of changes to test setup for the continuous switching ..... 70
10 BREAKDOWN VOLTAGE CONSIDERATIONS ..... 72
11 DISCUSSION ..... 77
12 CONCLUSIONS ..... 79

REFERENCES ........ 81
APPENDIX A: IXYS MII400-12E4 [18] ........ 84
APPENDIX B: EFI Gate Driver [4] ........ 86
APPENDIX C: 20kW Laboratory Inverter [3] ........ 87
APPENDIX D: Analog Current Control Board [13] ........ 88
APPENDIX E: Midel 7131 datasheet [22] ........ 91

# 1 INTRODUCTION

In the future, it is expected that oil and gas extraction will have to take place at greater depths than today. Beyond a certain depth, one will have to use pure subsea installations, that is, the extraction equipment will be placed on the seabed floor. Some of this equipment, i.e. compressors, needs to be driven by electrical motor drives.

The current solution for this drive is to mount it inside a pressure vessel at 1 bar pressure. At a certain depth, the walls of this pressure vessel become unreasonably thick. Apart from being expensive, the pressure vessel does not conduct the heat generated by the motor drive into the sea water very well. If forced cooling is not employed, the temperature inside the pressure vessel will therefore be relatively high, and the lifetime of the electronics will suffer because of this. It is therefore interesting to examine the possibility of avoiding the pressure vessel entirely, by exposing some parts of the motor drive directly to the ambient pressure of the sea.

The work done in this project is part of an ongoing long-term project at SINTEF Energy Research. Considering the long time span of the SINTEF project, it is not expected that the test object will be energized while under pressure during the project.

Much of the freely available papers on the subject of pressurizing electronics are old [5,6,10,11], but some of the general conclusions from these papers are still valid. Generally speaking, one of the most usual challenges encountered in these papers were the handling of voids in the electronic components. Voids in capacitors, transistors and other components will almost certainly lead to the destruction of the device in question when it is subjected to pressure. One paper [5], also mentions possible void formation between semiconductor material and metallization as a reason for breakdown of some components. It is not known whether this may be a problem today, with presumably more advanced production techniques.

It is also useful to have in mind that some part of the electronic system which generates less heat than the power electronics may be placed inside a pressure vessel, i.e. electronics for measurement and signalling. One paper [6] gives this as a possible method to reduce costs in cases where the pressure tolerant devices are more expensive.

One paper [11] gives screening procedures as an important part of the commissioning of pressure tolerant devices. Although this may seem obvious, it may be especially important with good screening procedures when pressure tolerant devices will be employed in applications where they are not easily accessible after installations, i.e. in motor drives located on the seabed floor.

As this Master project is part of a larger research project at SINTEF Energy Research, it was of interest to investigate several aspects of the pressurization of power electronics. Because proper pressurization facilities were not acquired during the project, pressurization of live components was not performed during the project. The emphasis was therefore put on investigating the components while operating in the same dielectric liquid as will be used during pressurization.

Firstly, the placement of electronics in dielectric liquid should have an effect on the cooling of the components. The thermal aspects of placing an IGBT module in dielectric oil have therefore been treated in chapter 4. Furthermore, since models are essential to describe and simulate physical systems, thermal modelling of the IGBT module is described in chapter 5. Thermocamera measurements give a useful alternative view of the thermal conditions in the IGBT when it is being heated, and this is therefore described in chapter 6.

Chapter 7 deals with stray inductance considerations in the test setup. Stray inductance will have an impact on the switching waveforms of the IGBT. It is therefore important to be aware of the impact of the bus bar geometry on the stray inductance.

Although no power electronics were pressurized while supplied with power during this project, passive pressure testing is the first milestone on the road to pressurization of switching components. Passive pressure testing as performed in this project is therefore described in chapter 8.

Also, it was not known whether the switching waveforms of the IGBT module would be affected when the module was placed in dielectric oil. The module was therefore switched before and after placement in dielectric oil, and the switching waveforms compared. The description of the test setup and the results of this testing can be found in chapter 9.

Finally, it was interesting to investigate if adding of water to the dielectric oil would have any impact on the operation of the IGBT. Breakdown voltage considerations were of special interest in this respect. This is described in chapter 10.

Discussion of the results is done immediately following the presentation of each result, but there is also a discussion chapter at the end of the report, which summarizes the discussion about the results. Graphs and pictures are primarily shown in the report itself, instead of in appendices, for easy reading.

As can be seen, the report deals with several of the aspects of placing power electronics in dielectric oil. Given the width of the investigations, the report will therefore also be relatively wide with respect to topics treated, and the organization of the report may be done in several different ways. It should however be noted that all of the topics is investigated with one goal in mind, and that is the eventual pressurization of power electronics. The purpose of this report is consequently to shed light on these different topics.

# 2 THEORY

## *2.1 Principal operation of the IGBT*

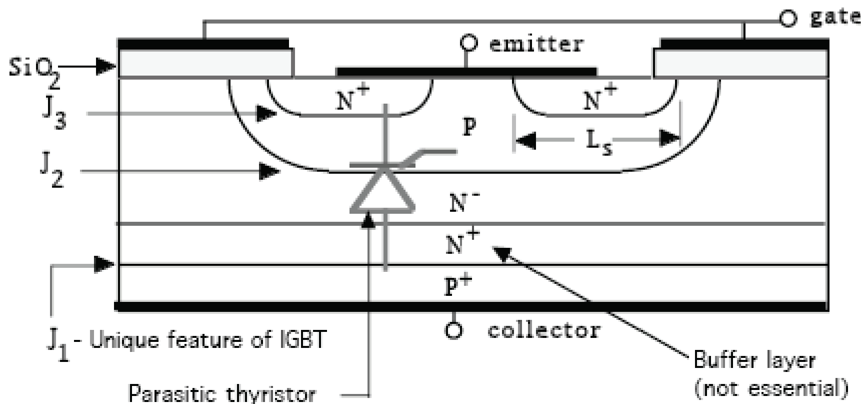


**Figure 1 Principal drawing of an IGBT [2]**

The generic operation of the Insulated Gate Bipolar Transistor, IGBT, is well described in literature, [2, 12] and only a short description will be given here, for the sake of completeness. Referring to Figure 1, the emitter of the IGBT is connected to the top N+ layer, while the collector is connected to the P+ layer at the bottom of the chip. When the IGBT is off, the gate is shorted to the emitter or a negative gate-emitter voltage is established. It can be seen from the figure that no current will flow in either direction through the device in this mode of operation, as both possible paths from collector to emitter contains a negatively biased junction.

An IGBT can be said to consist of a MOSFET type input stage, and a BJT type output stage, combining the best from the two technologies. That means using voltage as the controlling parameter on the MOSFET input, and using conductivity modulation in the BJT output stage. This gives fast switching of the MOSFET part in combination with low on-state losses. Although latch-up of the parasitic thyristor can be a problem in the IGBT, the modules used in the testing for this project are considered to be essentially latch-up proof for the currents and voltages involved. Latch-up will therefore not be treated further here.[2, 12]

In order to turn on the IGBT, a voltage is applied between the gate and emitter terminals in such a way that the gate attains a higher potential than the emitter. It is evident that the layer of oxide beneath the gate conductor will now act as a capacitor, with charge building up on both sides of the oxide. This build-up of charge in the P-layer underneath the gate oxide, will in turn invert the polarity of this layer, forming a continuous N-layer from the emitter until the P+ layer connected to the collector. The device will thus be able to lead current from collector to emitter.

The minimum value of $V_{GE}$ which will lead to current flowing through the device is termed the threshold value of the gate-emitter voltage, $V_{GE(th)}$. When the device is in the active mode of operation, the collector-emitter current $I_{CE}$ will depend on the values of gate-emitter voltage, $V_{GE}$, and collector-emitter voltage, $V_{CE}$. The typical output characteristic of an IGBT can be seen in Figure 2.[21]

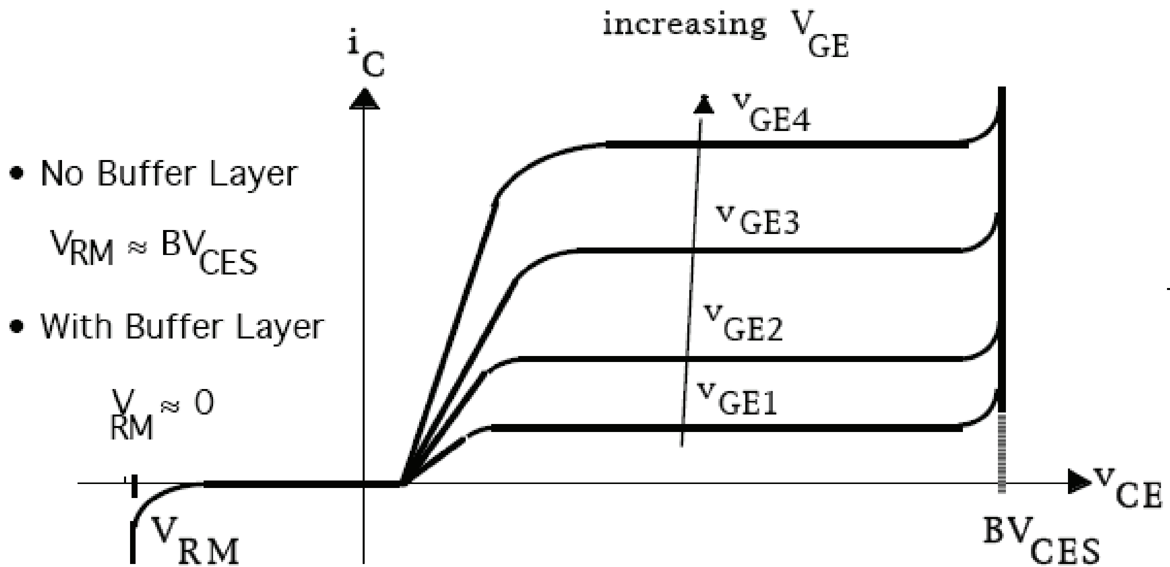


**Figure 2 Typical output characteristic of an IGBT [2]**

Unlike a MOSFET, the turn-off of an IGBT can not be forced, as recombination is necessary for all carriers to be removed. This leads to a tail current for the IGBT after turn-off. In order to turn off the IGBT, a negative gate-emitter voltage is applied, such that the capacitor formed by the oxide layer underneath the gate will be de-energized. This will lead to a rapid decline in the main current of the device, but since the BJT portion of the device relies on recombination for turn-off, the turn-off time will be longer than for a MOSFET.[2, 12]

Although different symbols for the IGBT are used today, the symbol shown in Figure 3 will be used in this text.

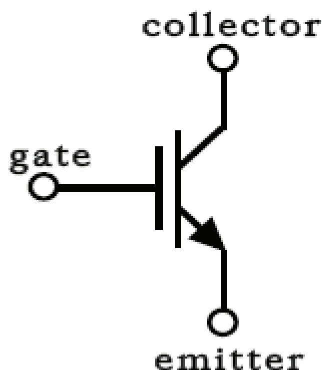


**Figure 3 Circuit symbol of the IGBT [2]**

Some understanding of the switching waveforms of the IGBT is useful when evaluating the curves which are recorded in the double-pulse switching. The capacitances of the device will be discussed first, as these have a significant impact on the switching waveforms. The capacitances existing between the terminals of an IGBT is shown in Figure 4. These capacitances consist of stray capacitances and depletion layer capacitances. . Some other important capacitances are defined as combinations of the terminal capacitances, summarized in Table 1. [2, 14, 16, 21]

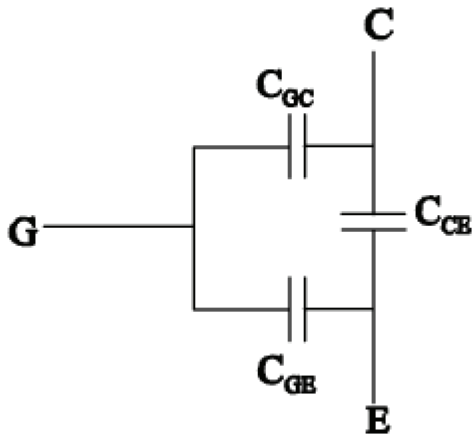


**Figure 4 Terminal capacitances of the IGBT**

**Table 1 Overview of capacitances in the IGBT [16]**

| | Symbol | Given as | Description |
|---|---|---|---|
| Input capacitance | $C_{ies}$ | $C_{GE}+C_{GC}$ | Must be charged/discharged before the device can begin to turn on/turn off. Will therefore have impact on the delay when switching |
| Output capacitance | $C_{oes}$ | $C_{CE}+C_{GC}$ | Can affect resonance in soft-switching |
| Reverse transfer capacitance | $C_{res}$ | $C_{GC}$ | Have impact on voltage rise and fall times when the device is switching. Also known as the Miller capacitance. |

It should be noted that especially the Miller capacitance have a significant impact on the switching performance of the device, e.g. the maximum switching speed.

## *2.2 Principal turn-on waveforms of the IGBT*

The turn-on of the IGBT can be summarized as follows, referring to Figure 5.

- When the step voltage is applied to the gate-emitter terminals, the input capacitance will begin to charge.
- When $C_{GE}$ is charged to the threshold value of $V_{GE,}$ given as $V_{GE(th)}$ in the figure, the collector current $I_C$ of the device will begin to increase in a linear manner
- When $I_C$ has reached its final value $I_L$, the collector-emitter voltage $V_{CE}$ will begin to decrease.
- $V_{GE}$ will remain at a constant value of $V_{GE(t)}$ , until $V_{CE}$ has decreased to its final value $V_{CE(on)}$. This is due to the fact that the IGBT is still in the active region, and $V_{GE}$ will therefore be given from the transfer curve of the device as a function of $I_C$. Achieving full conductivity modulation in the BJT portion of the IGBT may take longer time than for the MOSFET portion to turn fully on. The fast drop in $V_{CE}$ in $t_{fv1}$, primarily due to the MOSFET portion, will be followed by a slower drop during $t_{fv2}$ due to the BJT portion of the transistor going into saturation.
- After the MOSFET part of the IGBT has turned fully on, $V_{GE}$ will continue its increase to the value of the applied voltage at the gate-emitter terminals. The device is now fully on. [2, 21]

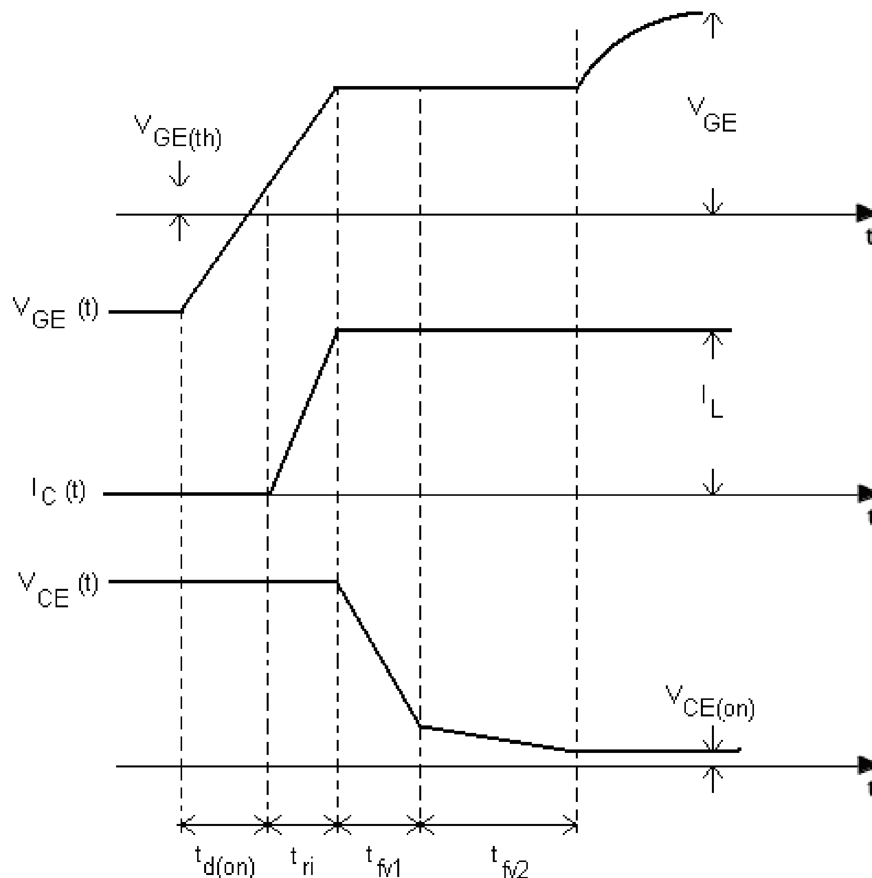


**Figure 5 Turn-on waveforms assuming a step positive voltage applied to gate-emitter terminals [1]**

## *2.3 Principal turn-off waveforms of the IGBT*

The turn-off of the IGBT can be summarized as follows, referring to Figure 6.

- A negative gate-emitter voltage is applied, and the gate-emitter capacitance will begin to discharge, lowering the value of $V_{GE}$
- When the IGBT enters the active region, the voltage over the device begins to increase, while $V_{GE}$ is constant and given by the transfer characteristic and the current through the device
- When $V_{CE}$ has reached its final value, the collector current $I_C$, will begin to decrease transferring the current to the freewheeling diode.
- The decrease of the collector current will be affected by two mechanisms. The MOSFET portion of the device will be turned off quickly, leading to a rapid decrease of the current in the first part of the transient. The MOSFET portion will have turned off when $V_{GE}$ reaches $V_{GE(th)}$. The minority carriers in the device will have to be removed by recombination, leading to a so-called tail current in the last part of the switching process. The length of this tail current will be influenced by the carrier lifetime in BJT section of the device. [2, 21]

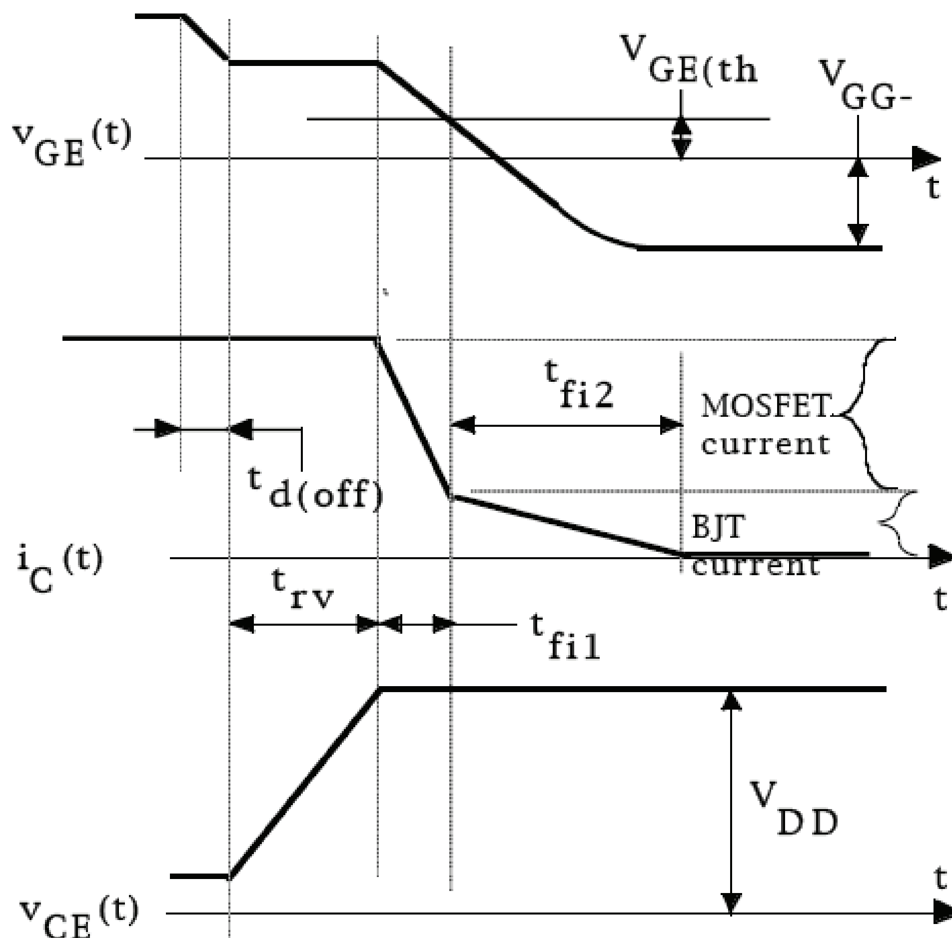


**Figure 6 Turn-off waveforms assuming a step negative voltage applied to the gate-emitter terminals [2]**

# 3 DESCRIPTION OF TEST OBJECT

## *3.1 IGBT module*

During the project an IGBT module from IXYS will be used for the thermal testing in the active mode of operation in addition to the double-pulse switching tests. The IXYS module is of type IXYS MII400-12E4. The module can be seen in Figure 7. Most of the tests in the project will be performed on a module with the top lid removed and without the dielectric gel that normally covers the electronic components. A picture of such a module can be seen in Figure 8. The datasheet for the module is enclosed in Appendix A.

**Figure 7 The IXYS module [18]**

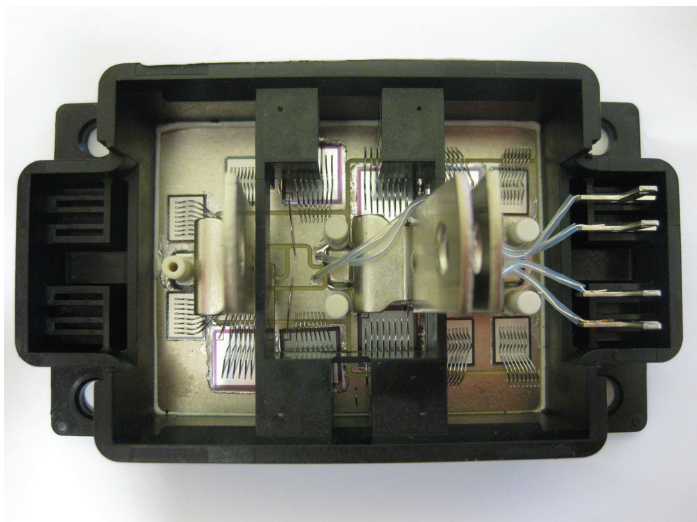

**Figure 8 Picture of a IXYS module without dielectric gel. The chips and wire bonding can be seen**

### 3.2 Dielectric oil

For some part of the testing, a module without dielectric gel will be covered in varying degrees by dielectric oil. Firstly, this is to investigate the effect of the dielectric oil on the thermal and switching behaviour. Secondly, the dielectric oil will provide the necessary insulation, normally provided by the dielectric gel, between the different live parts of the module. The dielectric insulating oil used in the testing is a synthetic ester of type Midel® 7131. This is a dielectric oil which is said to be suitable for transformers, tapchangers, electrical control equipment, etc. According to the manufacturer, Midel 7131 is a biodegradable, non-hazardous oil, with favourable thermal, fire resistance and dielectric properties. In addition, ester oils like Midel is, despite being hygroscopic, able to take up much more water than mineral oil without the breakdown voltage being compromised. [22, Appendix E]

# 4 THERMAL TESTING OF THE IGBT MODULE IN ACTIVE MODE OF OPERATION

## *4.1 Description of the test setup and initial testing*

In order to be able to measure the temperature behaviour of the IGBT module while at the same time having good control over the amount of dissipated power in the module, it was decided that one of the IGBT's in the bridgeleg should be run in the active mode of operation, conducting a DC-current. Since the DC-current running through the device and the DC-voltage over the device will be fairly constant, it is very convenient to calculate the dissipated power in the module as the product of these two quantities.

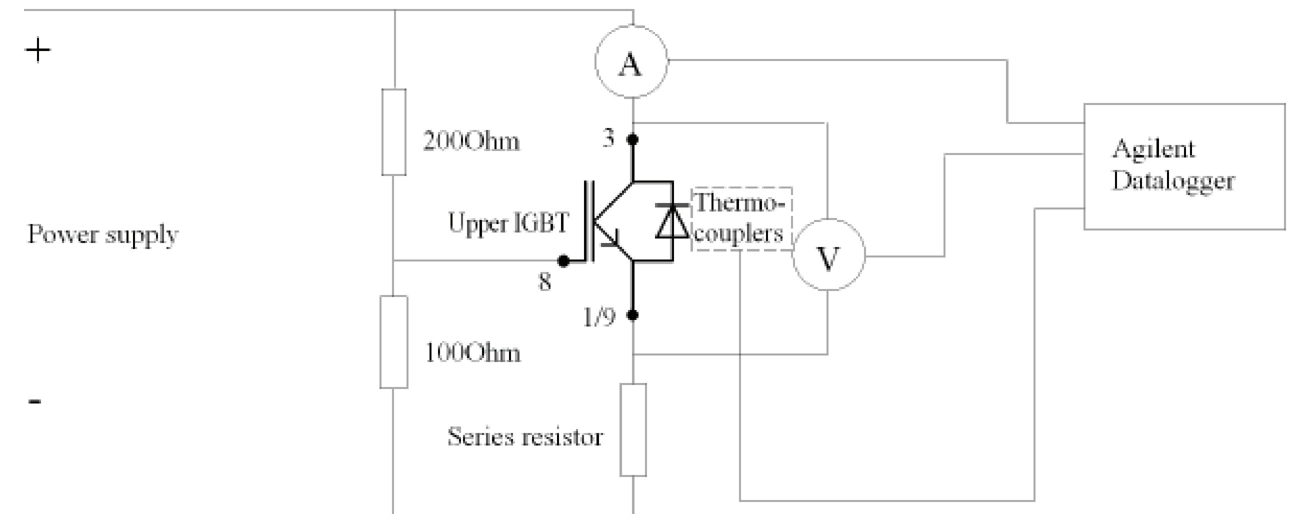


**Figure 9 Electrical test setup for power dissipation test in active mode of operation**

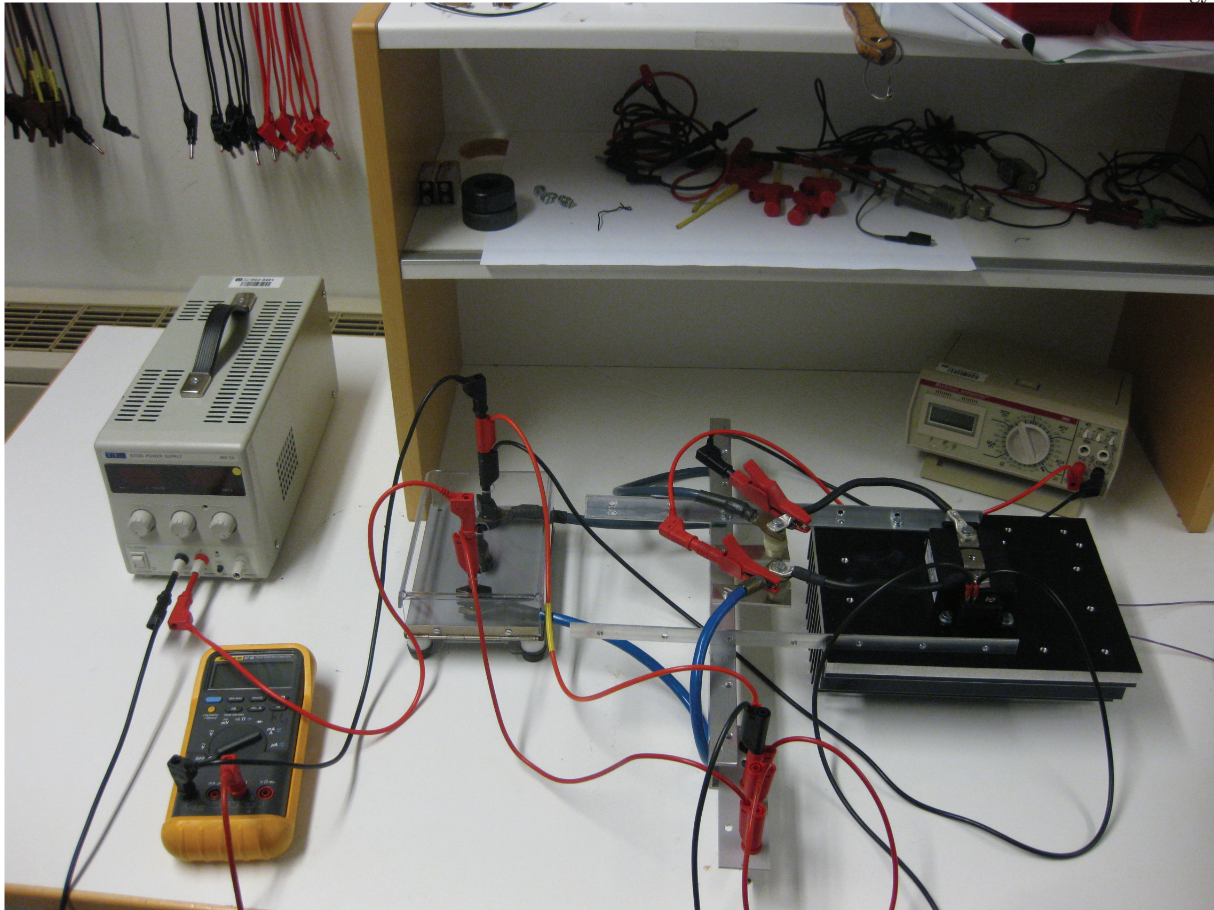

**Figure 10 Picture of the test setup for testing the IGBT module in the active mode of operation**

A picture of the test setup can be seen in Figure 10. During the initial testing an entirely standard IGBT module is used. The electrical test setup for the active testing of the module can be seen in Figure 9. As can be seen, the gate voltage for the IGBT is given by a voltage divider that is adjusted so that the IGBT will be only slightly on, so that much of the voltage from the power supply will be over the IGBT. The variable series resistor is used for easy adjustment of the current running through the IGBT. The temperature rise of the IGBT is recorded with thermocouplers and data logger. Two of the thermocouplers are located in the heatsink beneath the module. One of the thermocouplers is located on the middle power terminal of the module, and one at the overside of the heatsink. Initial testing showed a considerable difference in time constant when the heatsink was placed horizontally as opposed to when it was placed vertically.

During the testing, an approximately constant power is dissipated in the IGBT throughout the rising part of the transient until steady-state has been reached. The power supply is then turned off, and the falling part of the transient is recorded. Table 2 shows an example of the additional data that is recorded for the rising part of the transient. The module is heated, and the data is recorded at different points in time. It can be seen that even though the power supply is unregulated, the dissipated power in the IGBT is quite constant throughout. As might be expected, the middle power terminal measurement point has the fastest rise in the beginning because of the lower thermal capacitance from the junction to the measuring point. The middle power terminal measurement is also the one closest to the real junction temperature as this is the one which gives the highest temperature in steady state conditions.

**Table 2 Data from active testing of the IGBT**

| Temperature measurement 1 [°C] | Transistor voltage [V] | Transistor current [A] | Source voltage [V] | Source current [A] | Transistor power [W] |
|---|---|---|---|---|---|
| 30 | 18,8 | 5,04 | 19,9 | 5,05 | 94,75 |
| 44 | 18,6 | 5,04 | 19,6 | 5,05 | 93,74 |
| 50 | 18,5 | 5,04 | 19,5 | 5,05 | 93,24 |

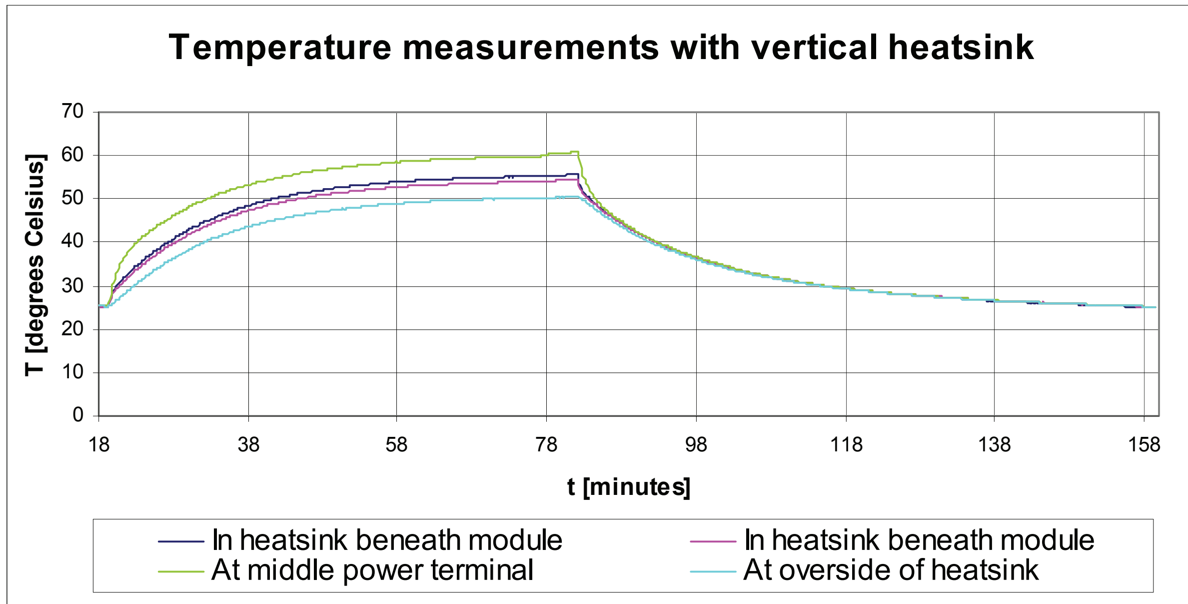


**Figure 11 Temperature transient for vertical heatsink at a dissipated power of approximately 94W**

To get an estimation of the temperature transient for the IGBT module alone, the heatsink is removed from the test setup. The IGBT is then run in active mode as before. Without the heatsink, power has to be applied cautiously, since the IGBT by itself has a very low heat dissipation capability.

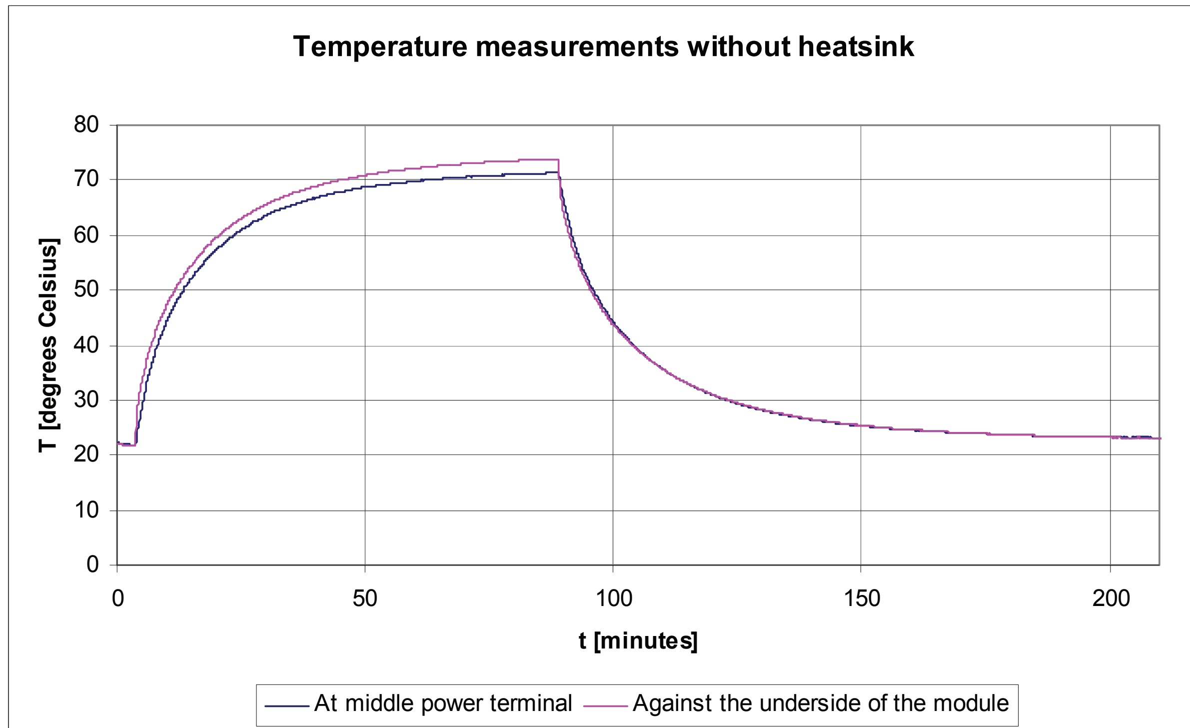


**Figure 12 Temperature transient for module without heatsink at a dissipated power of approximately 10W**

As can be seen from Figure 12, both measurements reach temperatures in excess of 70 degrees Celsius for a dissipated power of only 10W. This shows that the thermal resistance from case to ambient for the module without heatsink is quite high, more than 5K/W. It is also worth noting that the measurement under the substrate have a faster rise in the beginning of the transient and gives a higher stationary temperature. This is a sign that there is less thermal capacitance and resistance between the junction and the measurement point under the substrate compared to the power terminal measurement point. This can be expected, as the power terminal it self contains much copper and thereby heat capacitance compared to the layers of the substrate. The layers are also quite thin compared to the length of the power terminal, giving a smaller thermal resistance.

## *4.2 Active testing of module without gel in air*

After the initial testing with the standard module had been finished, testing was started on the module without gel, as shown in Figure 8 and Figure 13. To get a temperature measurement as close as possible to the junction, a temperature sensor was placed on top of the copper substrate, close to one of the chips conducting current. To get an accurate measurement, an active temperature sensor of type Analog Devices 590 was used. A picture of the placement of the AD590 temperature sensor can be seen in Figure 14. The temperature sensor was calibrated against a reference temperature source. As with the testing with the standard module, two thermocouplers are mounted in the heat sink as described in [21]. Initial testing showed that the temperature sensor on the chip gave much faster response to applied power than the two others. This was to be expected, as the thermal resistance and thermal capacitance between this sensor and the junction is less than for the two others.

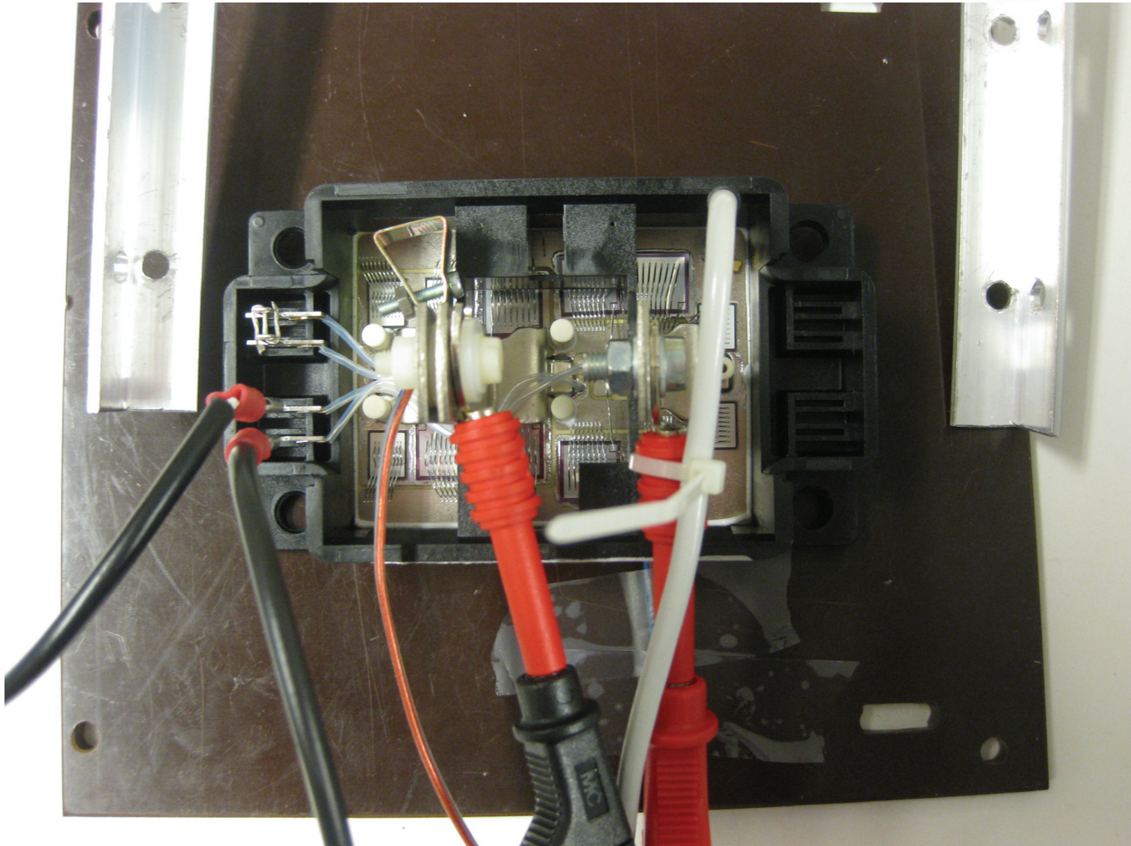

**Figure 13 Picture of IXYS module without gel under testing**

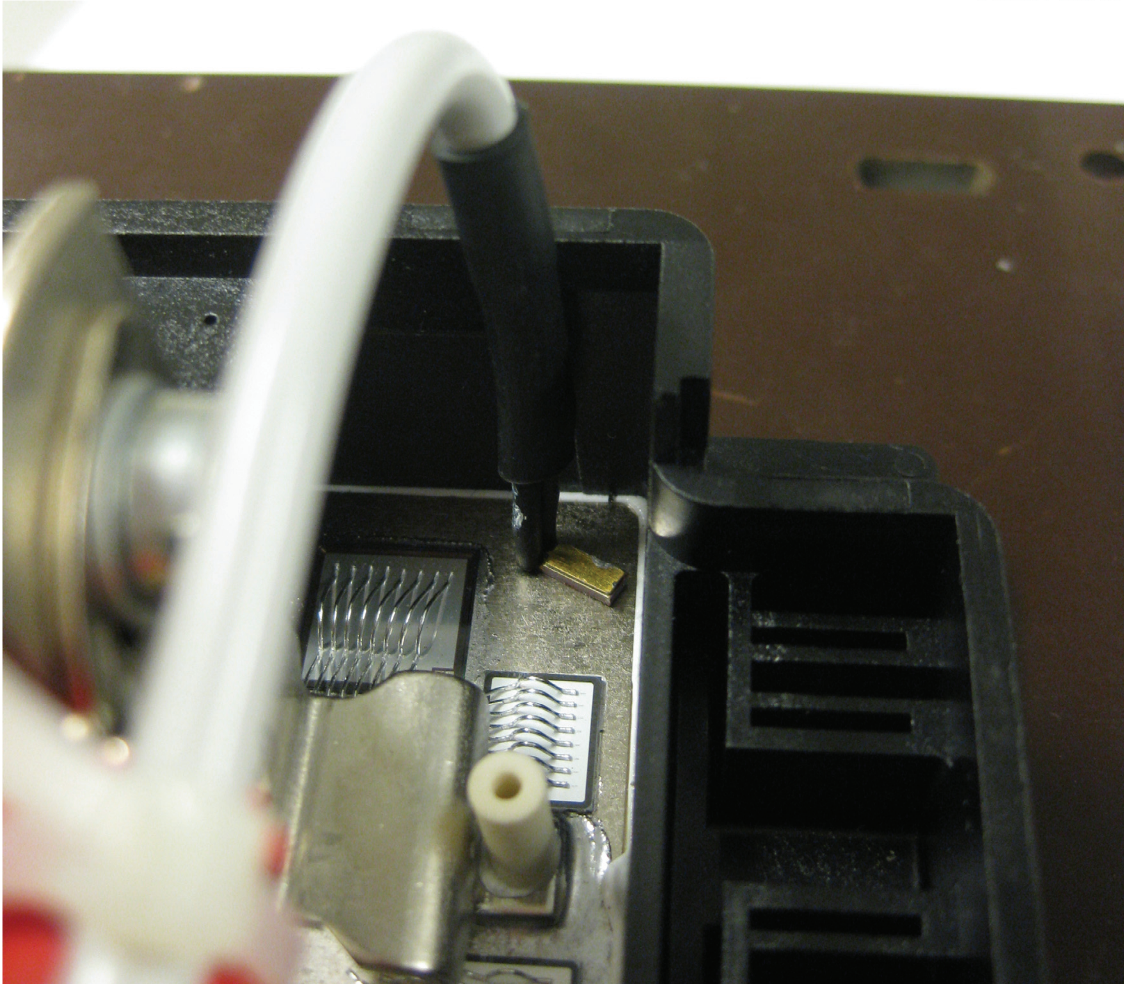

**Figure 14 Close-up picture of AD590 temperature sensor located on top of the substrate close to one of the IGBT chips. During actual testing a clamping arrangement holds the temperature sensor in place nearby the chip; this is not shown here for the sake of clarity**

The source and the resistors in the test setup were adjusted so that approximately 10W would be dissipated in one of the IGBT's. The temperature transient can be seen in Figure 15. As was expected the temperature sensor mounted directly on top of the substrate gave a much faster response for both the heating and cooling transients. Since it is not possible to mount a temperature sensor directly on the chip surface because of the bonding wires, this temperature measurement is probably the closest one can come to measuring the junction temperature for this module. It is also worth noting that the heat dissipation capability of the IGBT without heatsink is very small, with only 10W giving more than 80 degrees Celsius at the top of the substrate.

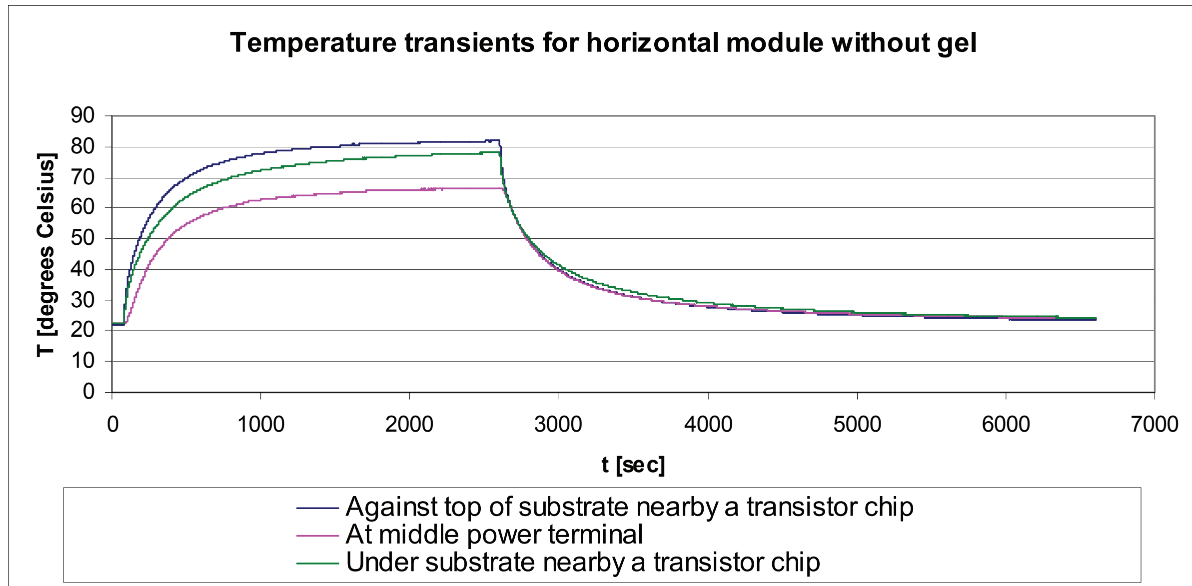


**Figure 15 Temperature measurements for horizontal IGBT module without gel**

In order to have a better understanding of the lateral temperature gradients in the substrate, it was decided to mount a second AD590 active temperature sensor on top of the substrate. The additional temperature sensor is mounted by the diode chips of the IGBT that is being heated, and a significant lateral distance from the IGBT chips. The placement of the AD590 temperature sensors in relation to the IGBT chips can be seen in Figure 16. In addition, thermal insulation in the form of isopor is placed underneath the module in order to minimize the heat flow in this direction. The temperature transient for this test is shown in Figure 17. It can be seen that the measurements at the top of the substrate away from the chip, and under the substrate, are almost equal throughout the transient.

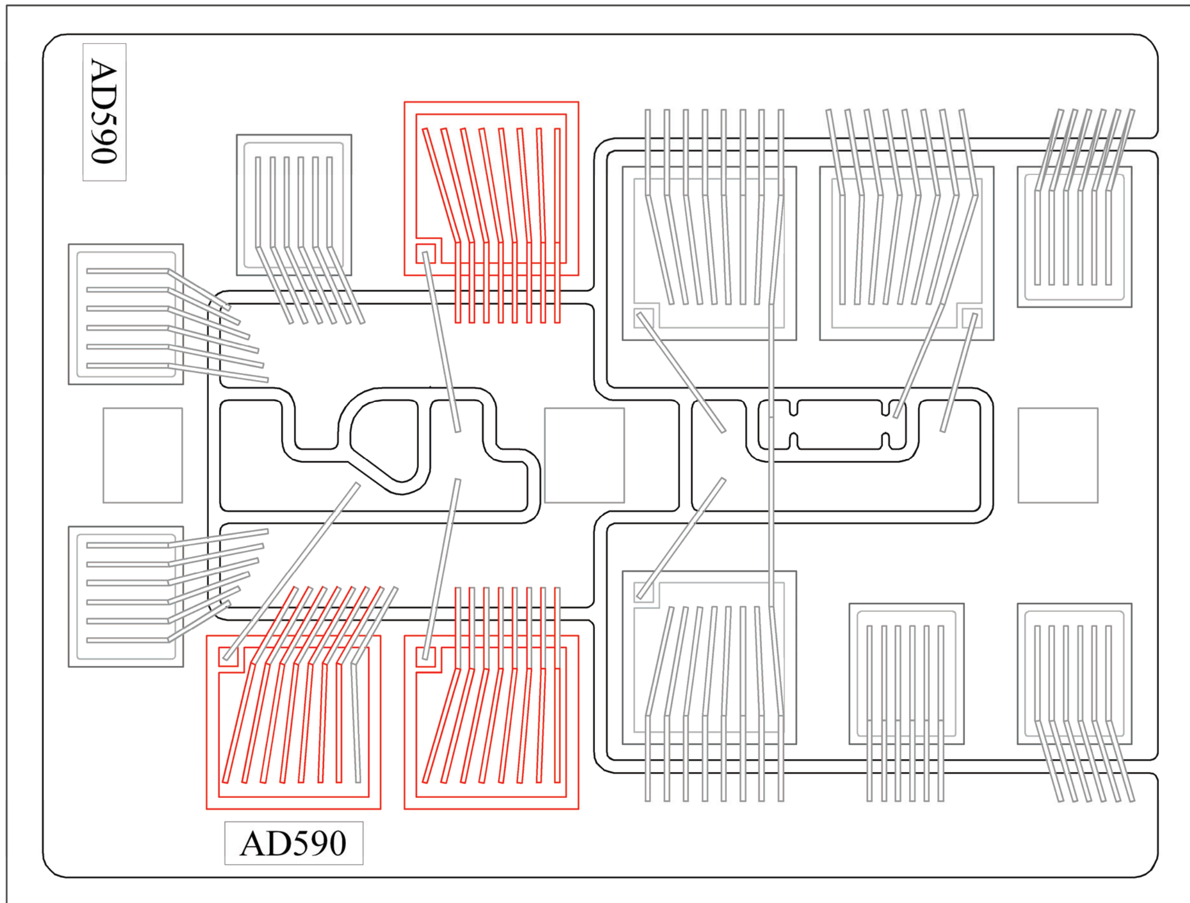


**Figure 16 Internal layout of IXYS module, with placement of AD590 temperature sensors. IGBT chips which are heated during active testing are shown in red**

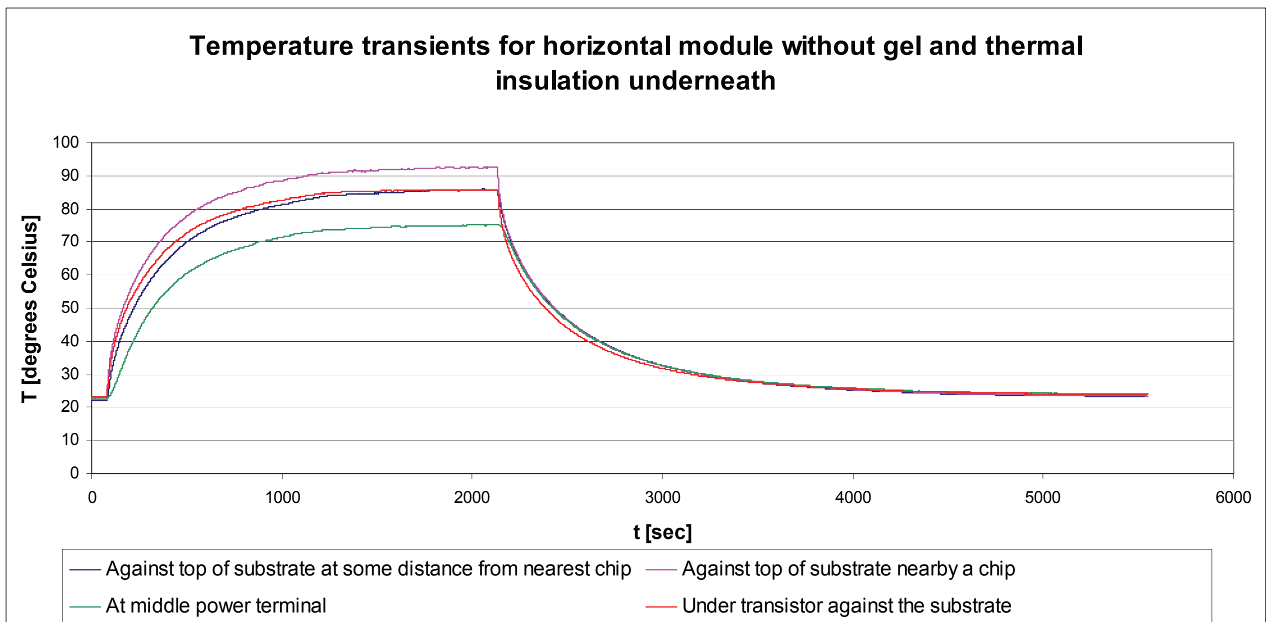


**Figure 17 Temperature transients including a measurement at top of substrate at some distance from nearest IGBT chip**

## 4.3 Testing of module without gel in Midel 7131

The module is now filled with 29mL of Midel 7131. The same test with insulated underside as described before is run again. The temperature transients for the AD590 sensor close by the chip can be seen in Figure 18. It can be seen that the heating of the module to steady state temperature takes much longer time with Midel inside the module. This is to be expected because of the added heat capacitance of the Midel. The steady state temperature difference however is relatively small at about 3 degrees Celsius.

**Figure 18 Temperature transients for module with thermally insulated underside, with and without Midel 7131**

The temperature transients when the module is filled with Midel can be seen in Figure 19. Comparing Figure 19 with Figure 17 some differences can be observed. It can be seen that the measurement under the substrate is much closer in temperature to the chip temperature when the module is filled with Midel than without. This is a sign that when the module is filled with Midel, more of the generated heat will be transported upwards. This in turn gives less heat transport down through the substrate layers, and thereby less temperature difference between the top and bottom of the substrate.

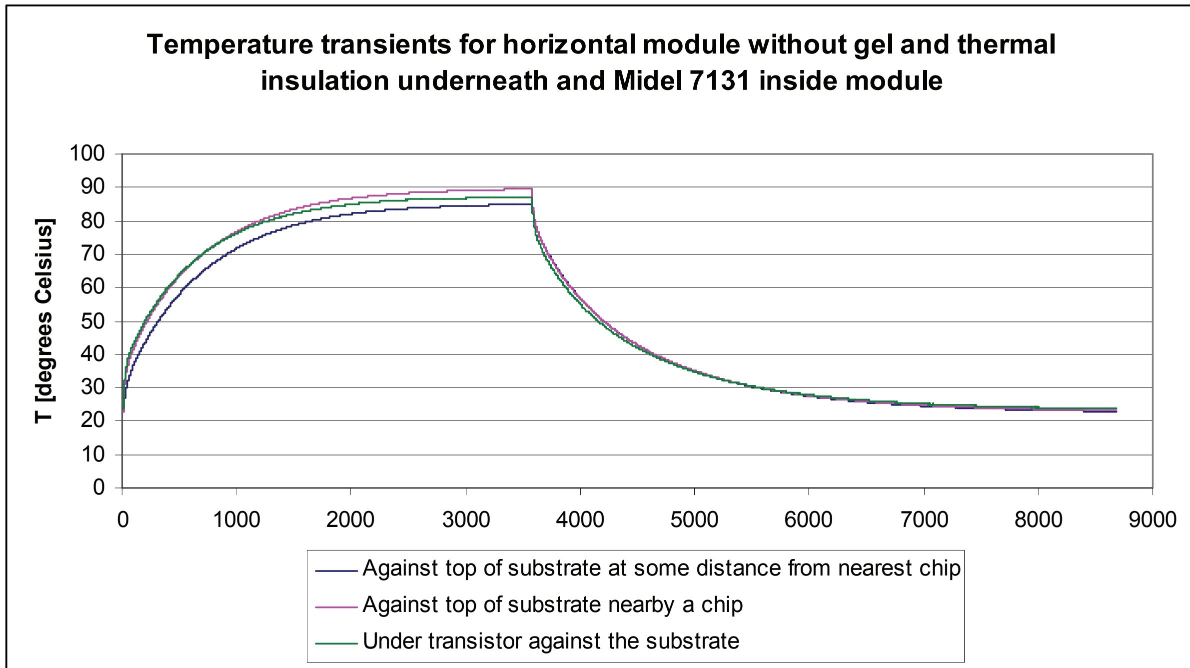


**Figure 19 Temperature transients when the module is filled with Midel 7131**

## *4.4 Estimation of heat flow in the module*

It was of interest to try to compare the heat flow in the module when it exposed to air as compared to when it is exposed to Midel. Although the real heat flow is not so easy to calculate for the two cases, this relatively easy calculation may say something about the difference between the two cases, which is interesting. The temperature difference in steady state is read from Figure 19. The readings are summarized in Table 3.

**Table 3 Summary of temperature readings from Figure 19**

| Steady state temperature nearby the chip | 89,6 degrees Celsius |
|---|---|
| Steady state temperature under the substrate | 87,1 degrees Celsius |
| Approximate temperature difference between chip and underside of substrate | 2,5 degrees Celsius |
| Applied power | 9,1 W |

Since each IGBT consists of 3 chips, the power that is dissipated in each chip can be calculated as in (1)

$$P_{chip} = \frac{P_{IGBT}}{3} \qquad (1)$$

Furthermore, if we consider a purely 2-dimensional heat flow down through the layers from the chip, we can use the chip area for computing the thermal resistance of the layers. Even though this will not be entirely correct because of the lateral heat spreading in the layers, the calculation will still represent a worst case scenario regarding thermal resistance. The thermal resistance calculation for each layer using chip area has already been performed in Table 14. Remembering that there are two layers of copper in the substrate, the thermal resistance of the substrate can be calculated as in (2)

$$R_{substrate} = R_{solder} + R_{ceramic} + 2 * R_{copper} \quad (2)$$

In addition, an estimation of the thermal resistance from case to the thermocoupler in the isopor has to be performed. Total thermal resistance will then be given as in (3).

$$R_{j-h} = R_{substrate} + R_{c-h} \quad (3)$$

$$P_{j-h} = \frac{\Delta T_{j-h}}{R_{j-h}} \quad (4)$$

Assuming a value of 3W/K for the thermal resistance between the case and the thermocoupler in the isopor, (1),(2),(3) and (4) can be used to calculate the power going down through the substrate layers. This is summarized in Table 4.

**Table 4 Summary of power flow calculations for module with Midel**

| Variable | Value |
|---|---|
| Thermal resistance of substrate layers | 0,2516 K/W |
| Thermal resistance from underside of substrate to isopor | 3 K/W |
| Power dissipation per chip | 3,0 W |
| Power flow down through the substrate | 0,769W |
| Percent of chip power flowing down through the substrate | 26% |

Similarly, the temperature difference for the case without Midel can be read from Figure 17. The readings are summarized in Table 5.

**Table 5 Summary of temperature readings from Figure 17**

| | |
|---|---|
| Steady state temperature nearby the chip | 92,5 degrees Celsius |
| Steady state temperature under the substrate | 85,6 degrees Celsius |
| Approximate temperature difference between chip and underside of substrate | 6,9 degrees Celsius |
| Applied power | 9 W |

**Table 6 Summary of power flow calculations for module without Midel**

| Variable | Value |
|---|---|
| Thermal resistance of substrate layers | 0,2516 K/W |
| Thermal resistance from underside of substrate to isopor | 3 K/W |
| Power dissipation per chip | 3,0 W |
| Power flow down through the substrate | 2,1 W |
| Percent of chip power flowing down through the substrate | 70% |

It can be seen that the power flow down through the substrate is larger when there is air above the chip. This means that there is more power flowing upwards when there is Midel on top of the chip than when air is used. Stationary cooling conditions will not be significantly better because both cases attain approximately the same steady state chip temperature. The Midel

case will be better for pulsed power, as the higher thermal capacitance of the Midel limits the short-term temperature increase.

### *4.5 Effects of movement of the oil*

It was decided to perform a test while the module was shaken manually, in order to increase the flow of oil inside the module, thereby increasing the cooling. Additional Midel 7131 was also added to the module, filling it to the rim. First, the module was heated without shaking it, to investigate the effect of adding more Midel 7131. The result of this test can be seen in Figure 20. As can be seen from this figure, the measurement under the substrate is actually a bit higher than the chip temperature measurement. This is taken as a sign that the additional cooling of the Midel will lead to very little heat flow down through the substrate. This will in turn mean that the temperature measurement at the underside of the substrate will be very close to the real chip temperature.

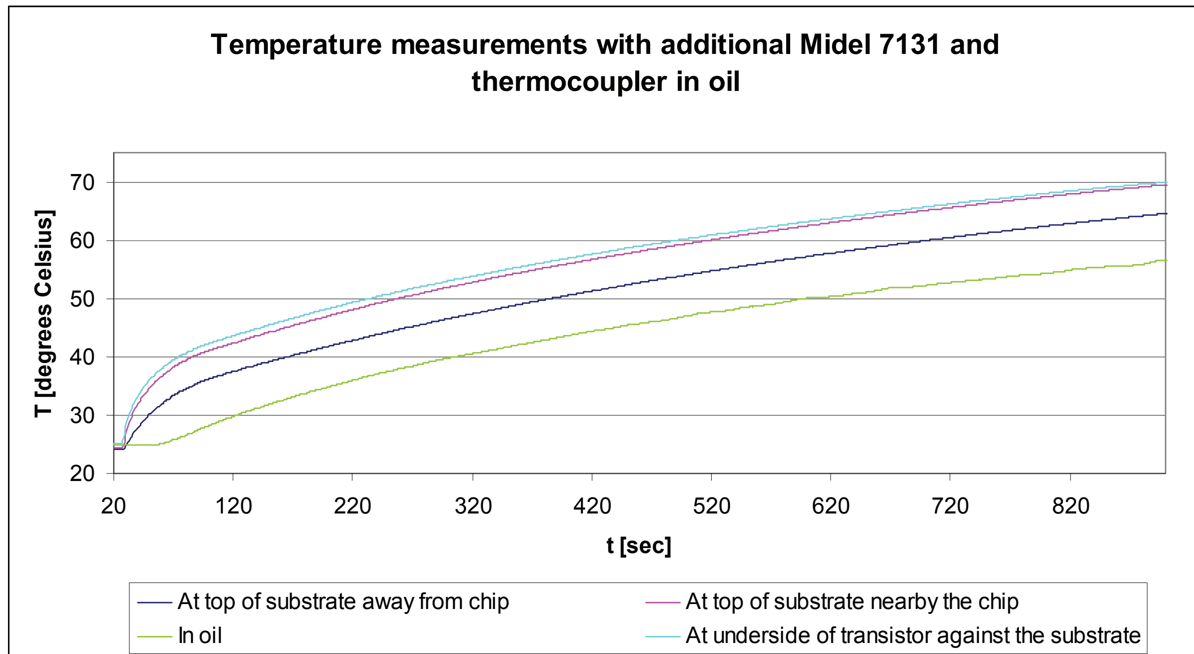


**Figure 20 Temperature measurements with additional Midel 7131 and thermocoupler in oil**

The thermal resistance between the chip and the oil will consist of a contact resistance at the interface and a distributed RC-network inside the oil itself. If one consider that the contact resistance is dominant when the oil is circulated, it is possible to estimate the thermal contact resistance between the chip and the oil. A simplified drawing of the situation during testing is shown in
Figure 21. It was shown in Figure 20 that the heat flow down through the substrate was very small, that is $P_{SUB} << P_{OIL}$. $R_{C\text{-}O}$ is the chip to oil thermal contact resistance and $R_{C\text{-}S}$ is the thermal resistance from chip to underside of substrate.

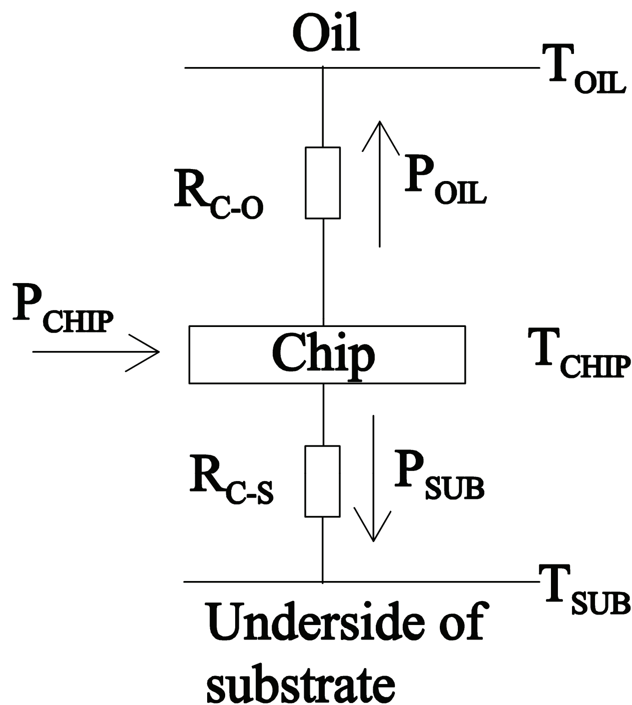


**Figure 21 Primary thermal flow paths during testing**

The module was shaken and the temperature transient was recorded until a steady increase was attained. This is shown in Figure 22. As can be seen from the figure, the difference between the oil temperature and the chip temperature is relatively stable once the initial transient is over. It can also be noted that the oil temperature is equal to its start value for a time after power has been applied, and does not start to rise before the initial transient in the chip temperature has passed. This difference was measured for a case where the oil temperature measurement was located close to a chip and for a case where it was located far from a chip. The results are summarized in Table 7.

**Table 7 Summary of temperature and power measurements**

| | Average temperature difference chip-oil [degrees Celsius] | Average power [W] |
|---|---|---|
| Oil measurement nearby chip | 11,29 | 9,68 |
| Oil measurement far from chip | 13,51 | 9,68 |
| Average | 12,4 | 9,68 |

Using the average values from Table 7, the thermal contact resistance from chip to oil can then be calculated according to (5), if one assumes that all the power goes into the oil.

$$R_{C-O} = \frac{T_{CHIP} - T_{OIL}}{P_{CHIP}} \tag{5}$$

Giving for the actual case:

$$R_{C-O} = \frac{12{,}4}{9{,}68} = 1{,}3\frac{K}{W}$$

To find support for this value of thermal contact resistance in literature is difficult, as this value depends much on geometry, and will thus vary from case to case. The number should therefore be treated as a rough estimate.

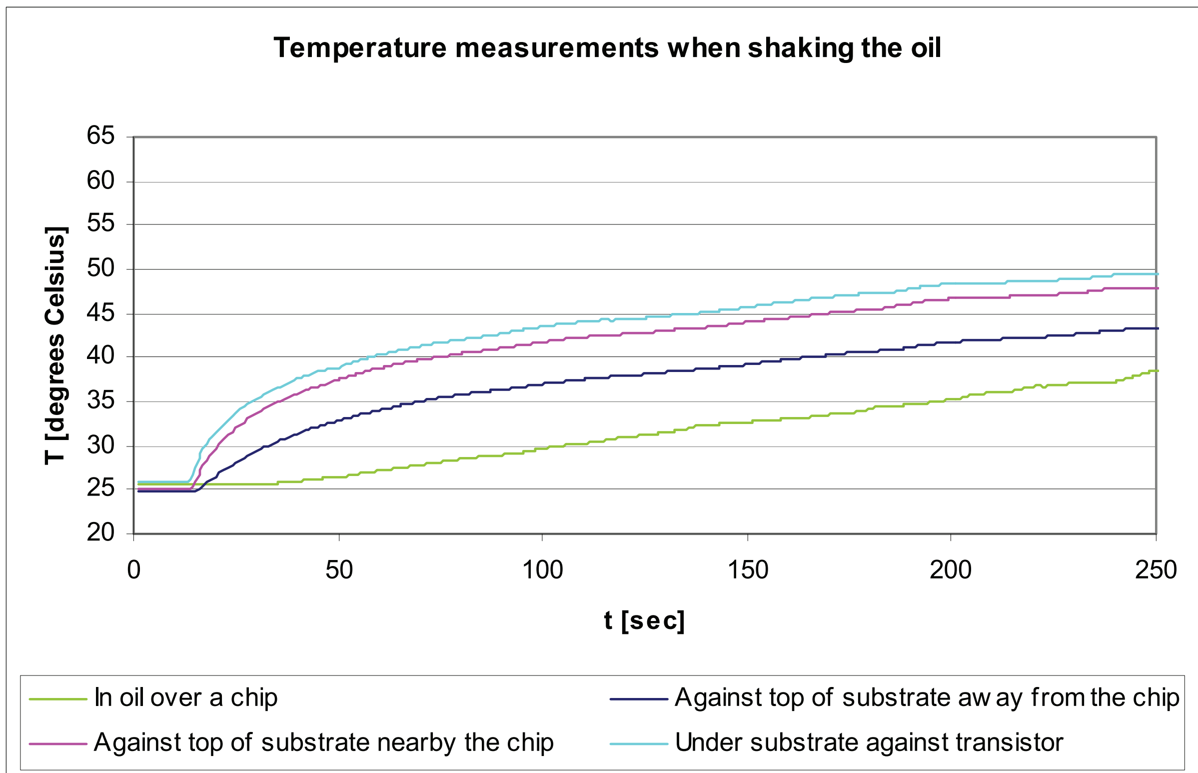


**Figure 22 Temperature measurements when shaking the oil**

The effect of shaking the module can be clearly seen in the temperature measurements. This is illustrated in Figure 23. “A” denotes time spans where the module is shaken, while “B” denotes time spans where the module is still. As can be seen from the figure, the rate of increase in the chip temperature is higher when the module is still; this is to be expected, as the transfer of heat through the oil is lower when it is still. It can be seen that the oil temperature actually goes a bit down at the instant that the shaking is stopped. This is probably due to the placement of the thermocoupler in oil being such that the thermal voltage drop between the chip and the thermocoupler being larger when the oil is still.

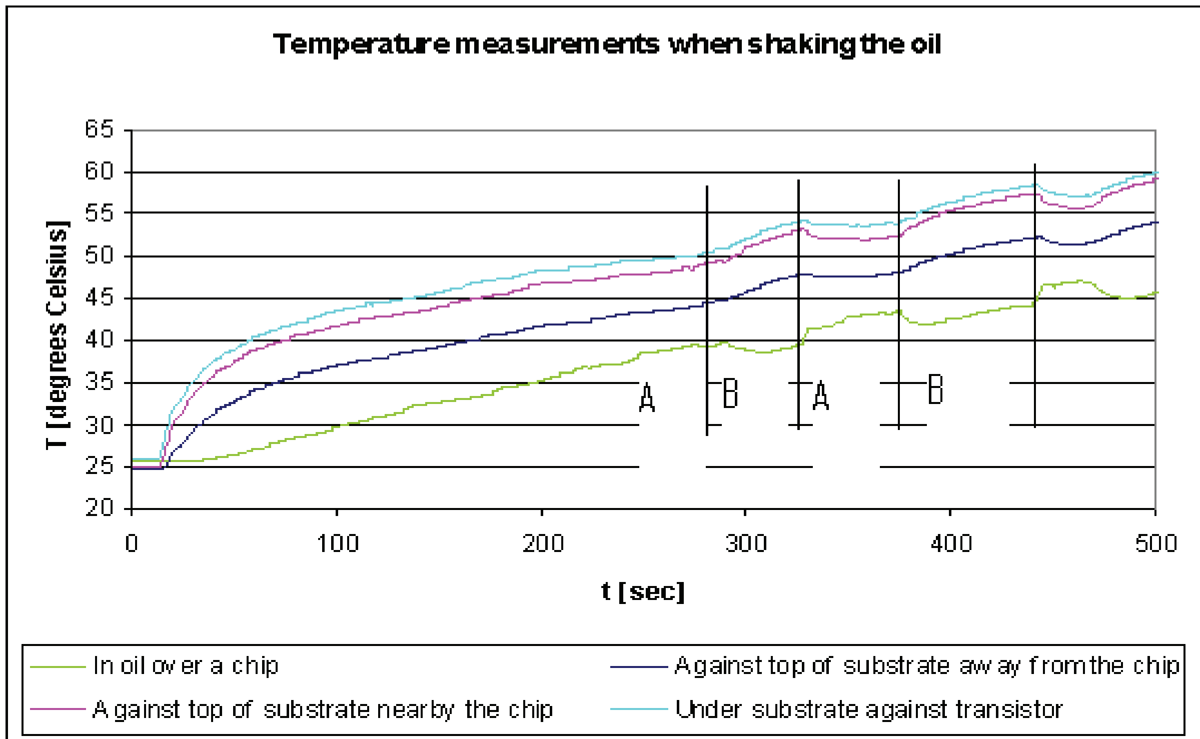


**Figure 23 Effect of shaking the module on the temperature measurements. "A" denotes time spans where the module is shaken, "B" denotes time spans where the module is still**

# 5 THERMAL MODELING OF THE IGBT MODULE

## 5.1 Modeling with thermal equivalent networks

### 5.1.1 Basic theory

Given the heating and cooling transient for the temperature measurements as given in Figure 15, it is possible to compute the associated time constants for the transient. The heating and cooling transients should be a mirror image of each other for ideal conditions. Assuming ideal conditions, the following discussion of time constant extraction will consider the cooling transient only, but it will be shown that the heating transient can be described with the same parameters as those extracted for the cooling transient.

Generally, the cooling transient for a power electronics package will consist of a sum of exponentially decaying functions. Because of the distributed nature of the problem, the theoretical number of exponentially decaying functions and associated time constants is infinite. That is, the theoretical time constant spectrum of the transient is continuous. The dynamic part of the cooling transient can be described as in equation (6). [33, 38]

$$\Delta T(t) = \sum_{i=0}^{\infty} T_i \cdot \exp(\frac{-t}{\tau_i}) \tag{6}$$

In practice, the time constant spectrum of the cooling transient is often regarded as discrete, consisting of a number of time constants. The number of time constants will in turn depend on the desired resolution or attainable resolution of the thermal problem. This will give a modified version of (6), shown in (7).

$$\Delta T(t) = \sum_{i=0}^{N} T_i \cdot \exp(\frac{-t}{\tau_i}) \tag{7}$$

When the exponential expressions describing the transient thermal behaviour are known, electrical-thermal equivalent diagrams can be constructed. The equivalent diagrams are a way of describing thermal behaviour by means of an electrical circuit. The reader may refer to [33] for a good introduction to this kind of modelling, but a brief description will be given also here.

Mainly two configurations of thermal equivalent networks are found in literature, the Foster network and the Cauer network. An example of a Foster network configuration can be seen in Figure 24. The main advantage of the Foster network is that each parallel connection of a resistor and a capacitor corresponds to one exponential term in (7). The network is thus quite easy to establish once the mathematical description of the transient behaviour is known. However, it is very important to be aware that the Foster network only gives a correct representation of the thermal response seen from the input and the output of the network. It is a behavioural equivalent circuit. That means that the equivalent circuit describes the overall behaviour rather than representing the geometrical structure of the system. Any attempt at measuring values inside the network will produce meaningless results.

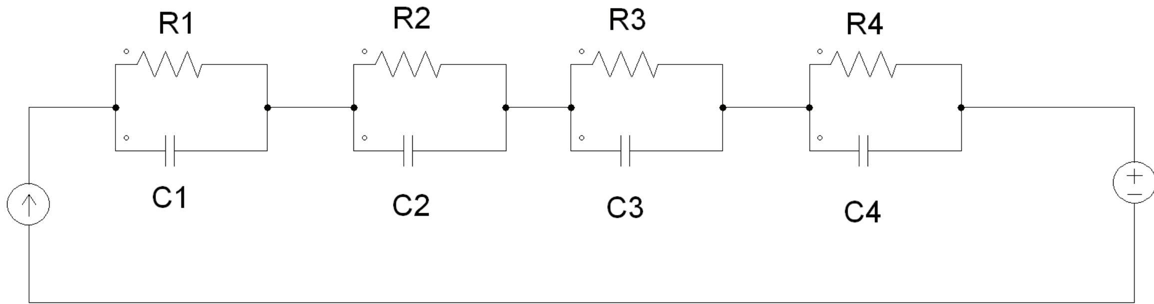


**Figure 24 Example of Foster thermal equivalent network**

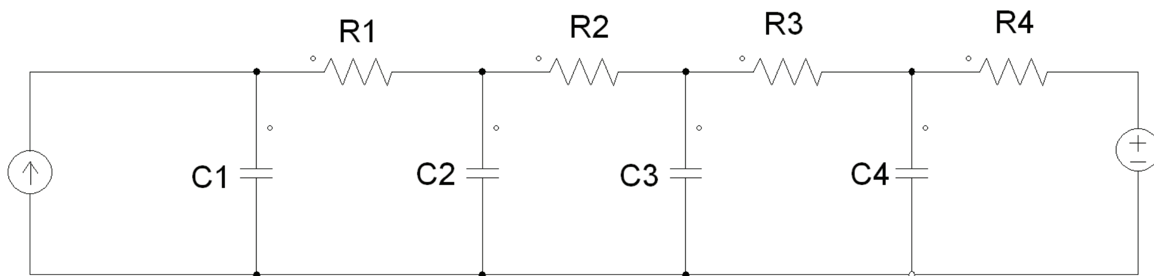


**Figure 25 Example of Cauer thermal equivalent network**

An example of a Cauer network configuration can be seen in Figure 25. In opposition to the Foster network, this network has a more complicated relation between the total mathematical expression and the circuit element values. One reason for this is that in the Cauer network each time constant depends on all the resistors and capacitors in the network, and each amplitude factor depends on all the resistors in the network. It can then be understood that going directly from a mathematical transient description as given by (7) to a Cauer network description is difficult. However, once the Cauer thermal equivalent has been established, this has a direct physical interpretation. Each node in the Cauer network represents a point in the thermal flow path of the device under testing. Consequently, if the number of RC-nodes in the network increases, also the resolution of the equivalent with relation to the physical device increases. In practice, if the number of RC-cells is small, it may be difficult to relate a specific RC-cell to a specific layer of the device under testing. This is because of the distributed nature of the time constant spectrum. [33, 34, 38].

During the modelling a certain correspondence between the thermal properties of the device and electrical circuit elements is assumed. When constructing the circuit, thermal variables will therefore be related to electrical ones according to Table 8.

**Table 8 Relations between electrical and thermal properties**

| Electrical property | Thermal property |
|---|---|
| Current [A] | Power [W] |
| Voltage [V] | Temperature [°C] |
| Resistance [Ohm] | Thermal resistance [°C/W] |
| Capacitance [F] | Heat capacity [J/°C] |

### 5.1.2 Description of available methods for time constant extraction

Several methods exist for extracting the time constants from thermal transients. Some of the methods involve a 3D finite element modelling of the device. The temperature transients of the device are then simulated and the thermal conditions in each layer of the device can be measured. These measurements can then be used to construct the thermal equivalent circuit of the device. An example of such an approach is given in [39]. Since a 3D finite element model of the IXYS module is expected to be time consuming, this approach will not be investigated further in this project. The complex structure of the IXYS module chip layout with many cross-connected bonding wires forming thermal bridges contribute to the expected complexity of the 3D modelling.

Other methods utilize advanced numerical methods for curve fitting of the cooling transient, and the sum of exponential expressions will then be given by the calculated approximation of the measured transient. An example of such a method is given in [33]. The time constant spectrum of the cooling transient is also possible to compute using convolution theorems. Numerical operations involving convolution and deconvolution are performed on the measured temperature transient. This gives the time-constant spectrum of a lumped element network representing the thermal behaviour of the device under testing. Examples of such an approach are given in [34] and [35]. Both these approaches are quite interesting when characterizing the thermal behaviour of a power electronic module. However, due to the limited time available in this project, a simpler method described in [38] is used to characterize the thermal response of the module with reasonable accuracy.

### 5.1.3 Extraction of the time constants for the cooling transient

Since no direct measurement of the junction temperature of the device is available, the temperature measurement as given by the AD590 temperature sensor mounted on top of the surface nearby the chip will be treated as the approximate junction temperature. This is assumed to be a reasonable approximation, as the sensor is mounted very close to the chip and in direct metallic contact. The heat capacitance between the chip and the sensor is also expected to be small because of the small thickness of the layers.

A thermal transient as in Figure 15 is then recorded, with the data logger set to a relatively high resolution i.e. 1 scan/sec.

Taking the natural logarithm to the measured cooling transient, it is possible to draw the plot of logarithmic temperature versus time, as shown in Figure 26. The ambient temperature is subtracted throughout the transient before the natural logarithm is taken, in order to investigate only the exponential decay.

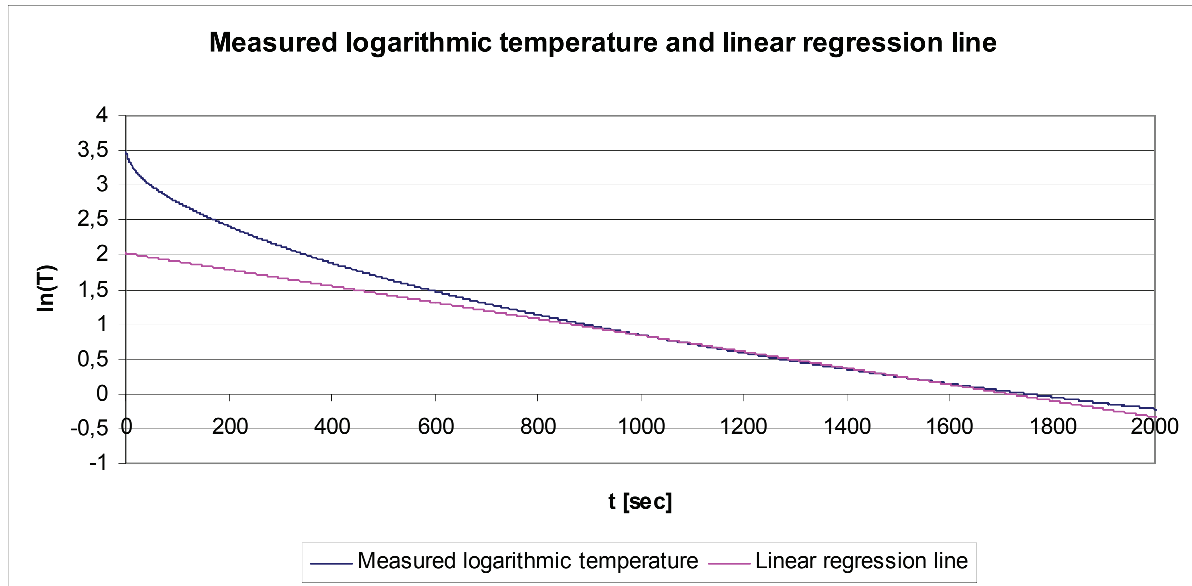


**Figure 26 Logarithmic temperature versus time and linear regression line**

As can be seen from Figure 26, the later part of the measured curve is quite linear, and it is possible to approximate the curve in this area with a linear regression line. Recalling the mathematical expression for the cooling transient as given in (7), this expression can be expanded, shown in (8).

$$\Delta T(t) = T_1 \cdot \exp(\frac{-t}{\tau_1}) + T_2 \cdot \exp(\frac{-t}{\tau_2}) + \ldots + T_n \cdot \exp(\frac{-t}{\tau_n}) \tag{8}$$

It is obvious from (8), that if one considers a time span very late in the transient, only the last time constant expression will have a significant value, as all the fast transients have decayed. For this condition, (8) can be approximated by (9)

$$\Delta T(t) \approx T_n \cdot \exp(\frac{-t}{\tau_n}) \tag{9}$$

And taking the natural logarithm on both sides yields:

$$\ln(\Delta T(t)) = \ln(T_n) - \frac{t}{\tau_n} \tag{10}$$

In (10) it can immediately be seen that the expression on the right hand side describes the line. This will actually be equal to the expression for the regression line shown in Figure 26. This is emphasized in (11)

$$b_n - a_n \cdot t = \ln(T_n) - \frac{t}{\tau_n} \tag{11}$$

Which gives

$$T_n = e^{b_n} \text{ and } \tau_n = \frac{1}{a_n} \tag{12}$$

When the first exponential expression has been calculated from (12), it has to be subtracted from the original cooling transient. The procedure will then continue with second-most slowest decay expression according to (13).

$$T_2 \cdot \exp(\frac{-t}{\tau_2}) \approx \Delta T(t) - T_1 \cdot \exp(\frac{-t}{\tau_1}) \tag{13}$$

These iterative calculations will reveal a number of time constant expressions describing the transient thermal behaviour. Since this procedure may give a good approximation in some parts of the transient while deviating in other parts, it may be necessary to add one or more extra time constants to give a better fit to the measured transient. In this project a simple trial and error approach was used for this.[33, 38].

Conducting the procedure described in the preceding paragraphs to the recorded transient yields the expressions described in Table 9.

**Table 9 Overview of extracted exponential expressions**

| n | T | τ | Total expression |
|---|---|---|---|
| 1 | 0,1737 | 847 | $0{,}1737 * \exp(\frac{-t}{847})$ |
| 2 | 0,1557 | 600 | $0{,}1557 * \exp(\frac{-t}{600})$ |
| 3 | 0,458 | 193 | $0{,}458 * \exp(\frac{-t}{193})$ |
| 4 | 0,213 | 30 | $0{,}213 * \exp(\frac{-t}{30})$ |

### 5.1.4 Foster thermal equivalent network construction

From Table 9 it is possible to calculate the thermal resistances and capacitances of the Foster equivalent network, given that one knows the steady state temperature drop and the applied power before the power is disconnected.

$$R_{tot} = \frac{\Delta T}{P} = \frac{80 - 23.5}{9} = 6{,}28 \left[\frac{K}{W}\right] \tag{14}$$

It is evident that each T in Table 9 is a weighting factor to the result obtained in (14). Each weighting factor will give the resistance for that particular Foster RC-cell. The calculation of the capacitance value thus becomes trivial, since the time constant is known. The result of this calculation for the actual case is presented in Table 10.

**Table 10 Overview of extracted values for thermal resistances and capacitances for the Foster equivalent network**

| n | R | C |
|---|---|---|
| 1 | 1,090 | 777 |
| 2 | 0,977 | 614 |
| 3 | 2,875 | 67,1 |
| 4 | 1,337 | 22,4 |

### 5.1.5 Cauer thermal equivalent network construction by network synthesis

In order for the equivalent circuit to have a physical meaning in addition to the two-port functionality provided by the Foster network, it has to be transformed into a Cauer equivalent network. Synthesizing a Cauer equivalent network as shown in Figure 25 from a sum of exponential terms is known from network synthesis theory. A thorough and generic description can be found in [40], but here the specific solution according to Figure 25 will be discussed. Examples of papers utilizing a similar approach can be found in [36] and [37].

The method that is used to synthesize the network is called continuous fraction expansion. It utilizes the property that a continuous fraction may be expanded into a form which is a direct description of a Cauer network. The first step is to transform the mathematical expression for the transient behaviour into the s-domain. This is done by way of the thermal transient impedance, defined as in (15).

$$Z_{th} = \frac{\Delta T}{P} \tag{15}$$

Transforming the transient impedance into the s-domain gives

$$Z_{th} = \sum_{n=1}^{N} \frac{1}{C_n \cdot \left( s + \frac{1}{R_n \cdot C_n} \right)} \tag{16}$$

Expanding and inserting the actual values

$$Z_{th} = \frac{1}{777 \cdot \left( s + \frac{1}{847} \right)} + \frac{1}{614 \cdot \left( s + \frac{1}{600} \right)} + \frac{1}{67{,}1 \cdot \left( s + \frac{1}{193} \right)} + \frac{1}{22{,}4 \cdot \left( s + \frac{1}{30} \right)} \tag{17}$$

The further calculations are iterative and will not be described in detail here; the reader is again referred to literature on network synthesis, i.e. [40]. Briefly, the procedure is as follows.

1. Arrange the expression in equation (17) on a common denominator
2. Invert the expression, that is take 1 divided by the expression
3. Make a proper fraction

4. The s-term in the rest will be the capacitor value for the leftmost undetermined capacitor in the equivalent circuit. Subtract this s-term from the inverted expression that was obtained in 2.
5. Invert the expression gained from 4.
6. Make a proper fraction
7. The constant term in the rest will be the resistor value for the leftmost undetermined resistor in the equivalent circuit. Subtract this constant term from the inverted expression gained from 5.
8. Go to 2.

Mathematically, this procedure gives the following result:

$$Z_{th} = \cfrac{1}{s \cdot C_1 + \cfrac{1}{R_2 + \cfrac{1}{s \cdot C_2 + \cfrac{1}{R_3 + \cfrac{1}{s \cdot C_3 + \dots\dots}}}}} \tag{18}$$

**Table 11 Overview of extracted values for thermal resistances and capacitances for the Cauer equivalent network**

| n | R | C |
|---|---|---|
| 1 | 2,5091 | 15,80 |
| 2 | 2,8540 | 59,85 |
| 3 | 0,9185 | 657,0 |
| 4 | 0,02941 | 24464 |

Using the procedure as described on the actual case yields the results as presented in Table 11. It can be seen that the last term involves a very small resistance coupled with a very large capacitance. This term will behave approximately as an ideal voltage source. Since we already have an ideal voltage source in parallel with this term, representing the ambient temperature, this term may be neglected. Simulation has confirmed that the circuit behaviour is practically equal for the cases with and without this term included. The equivalent circuit is thus reduced to three RC-cells. The corresponding Cauer network can be seen in Figure 27.

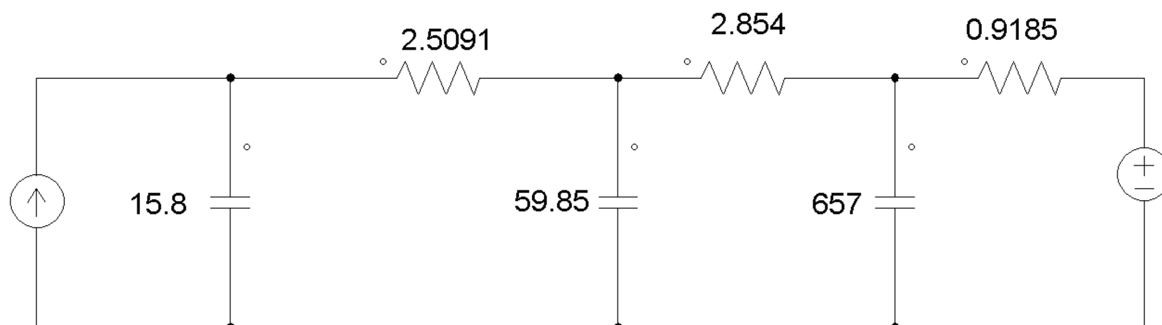


**Figure 27 Extracted thermal equivalent network**

### 5.1.6 Verification of the Cauer equivalent network

The calculated Cauer network was implemented in the circuit simulator PSIM™. The temperature drop over the three RC-cells was recorded when applying a power pulse similar to the one used in the actual laboratory experiment. Figure 28 shows the comparison of the measured, calculated and simulated heating transient. As can be seen, there is a good correspondence between the there curves. The calculated and simulated curves are practically identical, meaning that the synthesis of the Cauer network was successful. Maximum deviation between measurements and simulation is about 2-3 degrees Celsius.

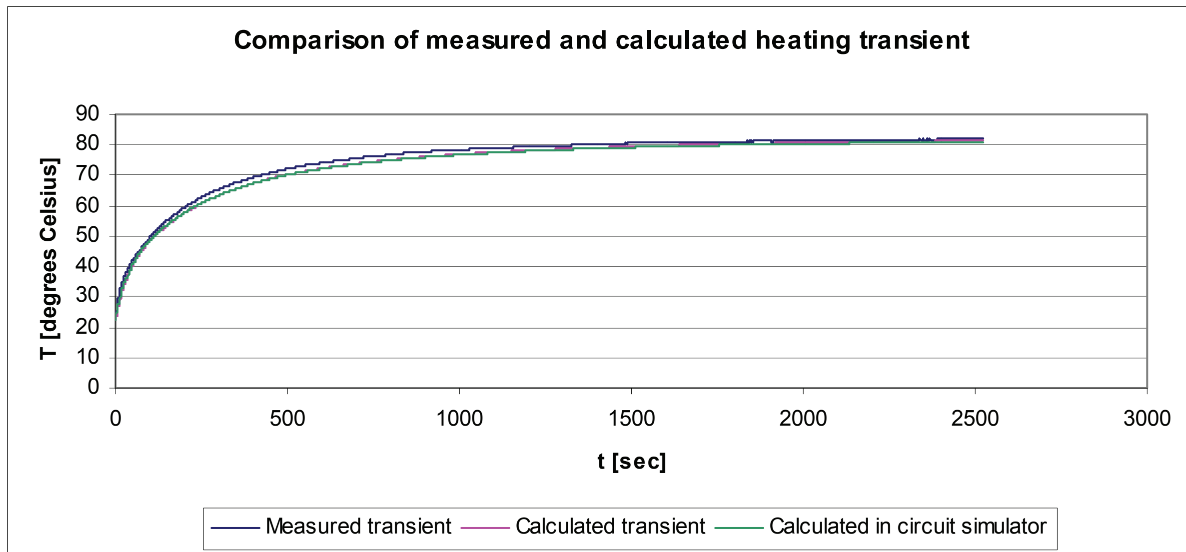


**Figure 28 Comparison of measured, calculated and simulated heating transient**

It was decided to investigate if the temperature measurement on the underside of the substrate could be approximated by the same model in PSIM. The steady state temperature ratio between this measurement and the chip measurement is multiplied with the total thermal resistance as found in (15). This gives an indication of the thermal resistance between the chip and the temperature measurement under the substrate.

The problem will be considerably simplified if the thermal capacitance between the chip and the measurement point on the underside of the substrate is regarded as very small. An approximation to the temperature at this point is then possible to simulate by splitting resistor 1 in the equivalent circuit accordingly. The simulation result is presented in Figure 29. It can be seen that there is a relatively good correspondence between measurement and simulation, with maximum deviation at about 2-3 degrees Celsius. It seems that the approximation with splitting resistor 1 without modifying the corresponding capacitance is relatively good.

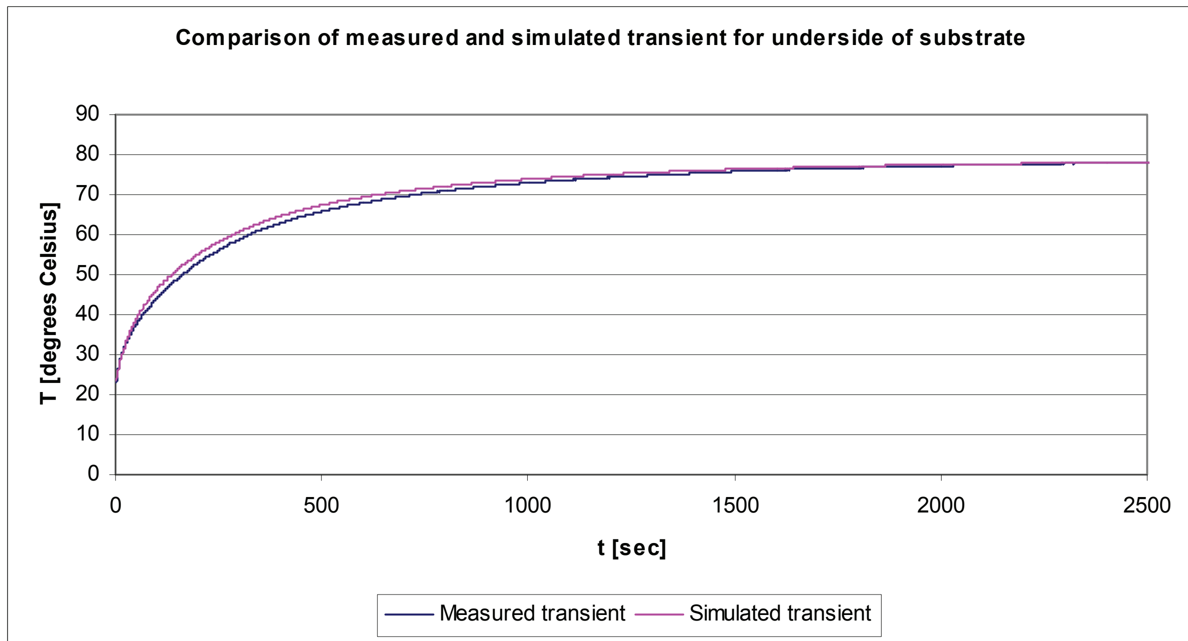


**Figure 29 Comparison of measured and simulated transient for underside of substrate**

The Cauer equivalent networks for the cases where isopor is placed underneath the module and respectively air and Midel 7131 is inside have been calculated using the same procedure as before. These networks have not been utilized in this project, but they are shown in Table 12 and Table 13 for possible future use.

**Table 12 Extracted Cauer network with air in module and isopor underneath**

| n | R | C |
|---|---|---|
| 1 | 2,0136 | 15,65 |
| 2 | 3,036 | 59,19 |
| 3 | 1,144 | 739,8 |

**Table 13 Extracted Cauer network with Midel in module and isopor underneath**

| n | R | C |
|---|---|---|
| 1 | 1,199 | 14,5 |
| 2 | 3,227 | 94,89 |
| 3 | 2,793 | 188,3 |

## 5.2 Modeling in COMSOL Multiphysics

### 5.2.1 Basic model

In order to gain an understanding of the thermal conditions in the IGBT module during operation, it is beneficial to describe the thermal properties of the module in a model. The geometric layout of the different layers in the module will form the basis of the model. Since the modelling only considers one IGBT chip, direct comparison between simulation and laboratory experiments will be difficult. The primary aim of the COMSOL simulations is therefore to look at some relatively simple cases where the chip is cooled by either air or Midel.

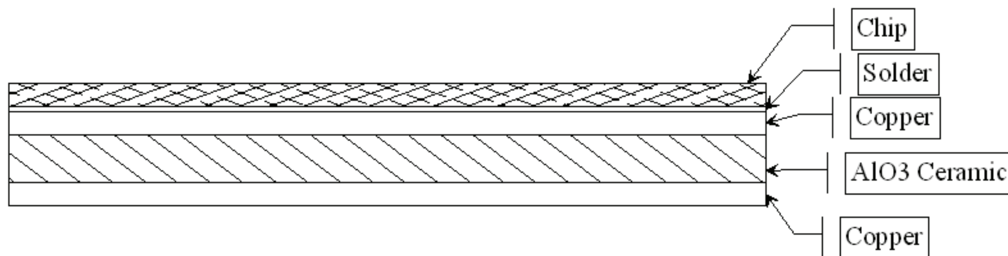


**Figure 30 Cross-section of IGBT chip and substrate layers**

Figure 30 shows a cross-section view of the IGBT chip and the substrate layers beneath it. In the IXYS MII 400-12E4 module each IGBT consists of 3 such chips in parallel. Each diode also has 3 chips in parallel. With 2 IGBT and 2 diodes, this makes for a total of 12 such chips on the substrate. Here a modelling of one IGBT chip will be attempted.

To be able to model the layers correctly, relevant information about the relevant thermal properties needs to be collected. This can be seen in Table 14.

**Table 14 Summary of substrate layers and thermal properties [23, 31]**

| Name of layer | Thickness [μm] | Thermal conductivity [W/m*K] | Thermal resistance using IGBT chip area [K/W] |
|---|---|---|---|
| Chip | 300 | - | - |
| Solder | 80 | 66,6 | 0,009927 |
| Copper | 300 | 401 | 0,012366 |
| Ceramic | 630 | 24 | 0,216942 |

As can be seen from Table 14, most of the thermal resistance is located in the ceramic layer between the two copper layers. This is to be expected since this layer is fairly thick and has a low thermal conductivity. Also the thermal capacitances for the layers are interesting from a modelling point of view.

### 5.2.2 Model with simple flow of cooling medium

In order to get a better picture of the thermal behaviour of the simplified model shown in Figure 30, it was decided to do a finite element analysis of the geometry in COMSOL Multiphysics®.

First it is necessary to state the thermal properties of the materials that will be used in the modelling. This is shown in Table 15.

**Table 15 Thermal properties for the materials used in the model**

| Material | Thermal conductivity [W/(m*K)] | Heat capacity [J/(kg*K)] | Density [kg/m$^3$] |
|---|---|---|---|
| Silicon | 163 | 703 | 2330 |
| Solder | 50 | 150 | 9000 |
| Copper | 401 | 385 | 8933 |
| Ceramic | 24 | 765 | 3970 |
| Air | 26,3E-3 | 1007 | 1,1614 |
| Midel 7131 | 0,144 | 1910 | 963 |

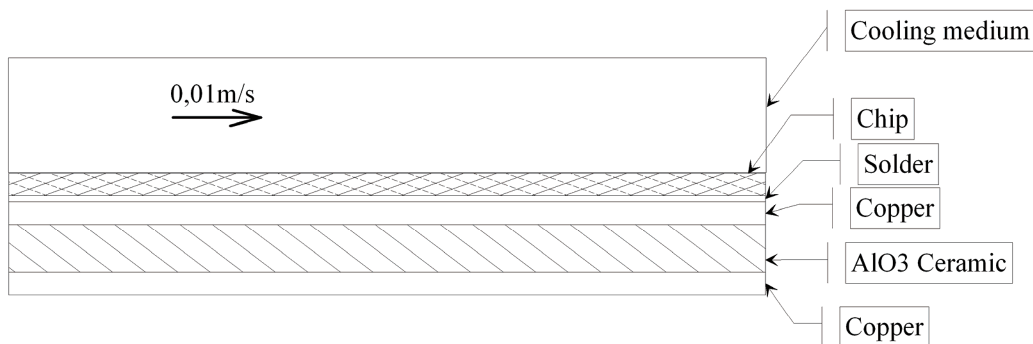


**Figure 31 Simple model used as a first approximation in COMSOL**

First, air is used as a cooling medium, and the flow is defined to be from left to right at a speed of 0.01 m/s. A sketch of the model can be seen in Figure 31. The underside of the substrate is presumed to be cooled by other means, and is set to a constant temperature of 60 degrees Celsius. The chip is assumed to dissipate 10W evenly distributed throughout the chip volume. A steady state analysis is performed regarding the thermal flow patterns in the geometry. As can be seen from Figure 32, essentially all of the heat transport for this case is done by means of conduction from the chip and down through the substrate layers. The air does not take up any significant heat.

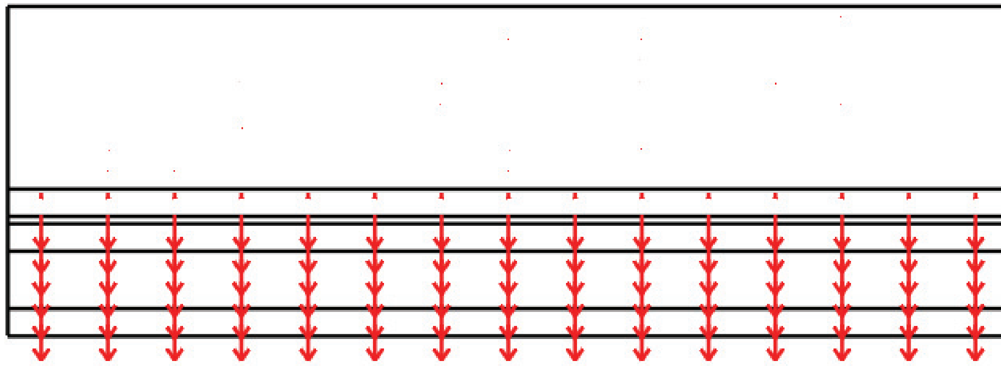

**Figure 32 Heat flow pattern for air as cooling medium**

With all other conditions equal, the cooling medium is changed to Midel 7131. As can be seen from Figure 33 much more heat is now absorbed by the cooling medium by convection. This in turn leads to less heat being conducted down through the substrate layers. Since the thermal conductivity for Midel 7131 is larger than for air this result is to be expected.

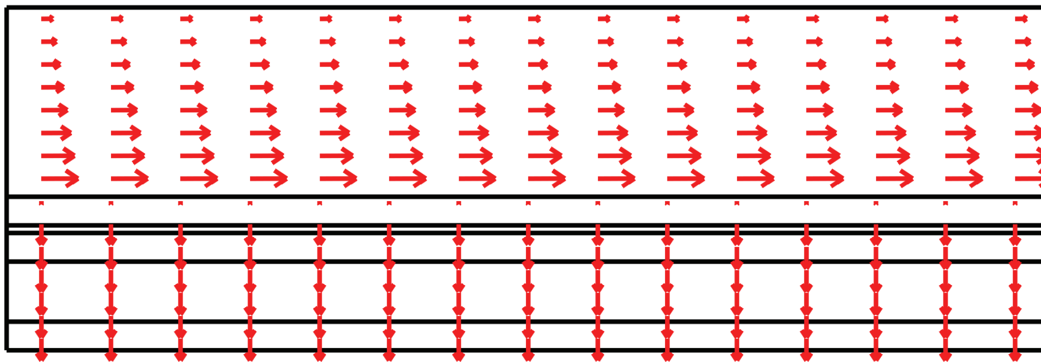

**Figure 33 Heat flow pattern for Midel 7131 as cooling medium**

The simple model in COMSOL described before is expanded to take into account the heat spreading in the substrate between the chips. The substrate layers and cooling medium is prolonged on each side of the chip. One half chip length is available on each side of the chip for heat spreading. The cooling medium is assumed to enter from the left with a constant temperature of 21 degrees Celsius and a speed of 0,01m/s. A sketch of the model featuring the boundary conditions can be seen in Figure 34. Firstly Midel 7131 is used as a cooling medium. A picture of this simulation can be seen in Figure 35. Air is then used as a cooling medium under the same conditions as for Midel 7131. The result from simulation with air can be seen in Figure 36.

Comparing the cooling medium for the two simulations, it can be seen that Midel 7131 has a lower temperature throughout compared to air. This is an indication that Midel 7131 has a better ability to transport the generated heat away, which is to be expected when looking at the thermal properties.

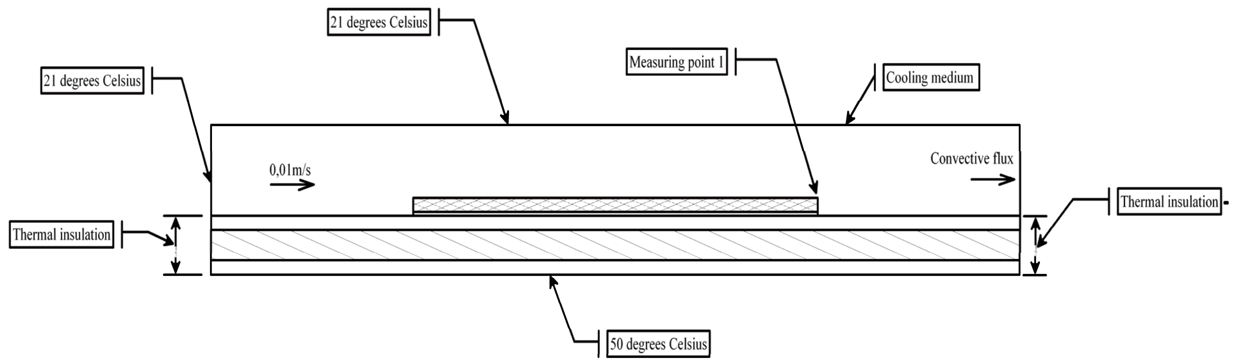


**Figure 34 Overview of the COMSOL model of the chip with boundary conditions**

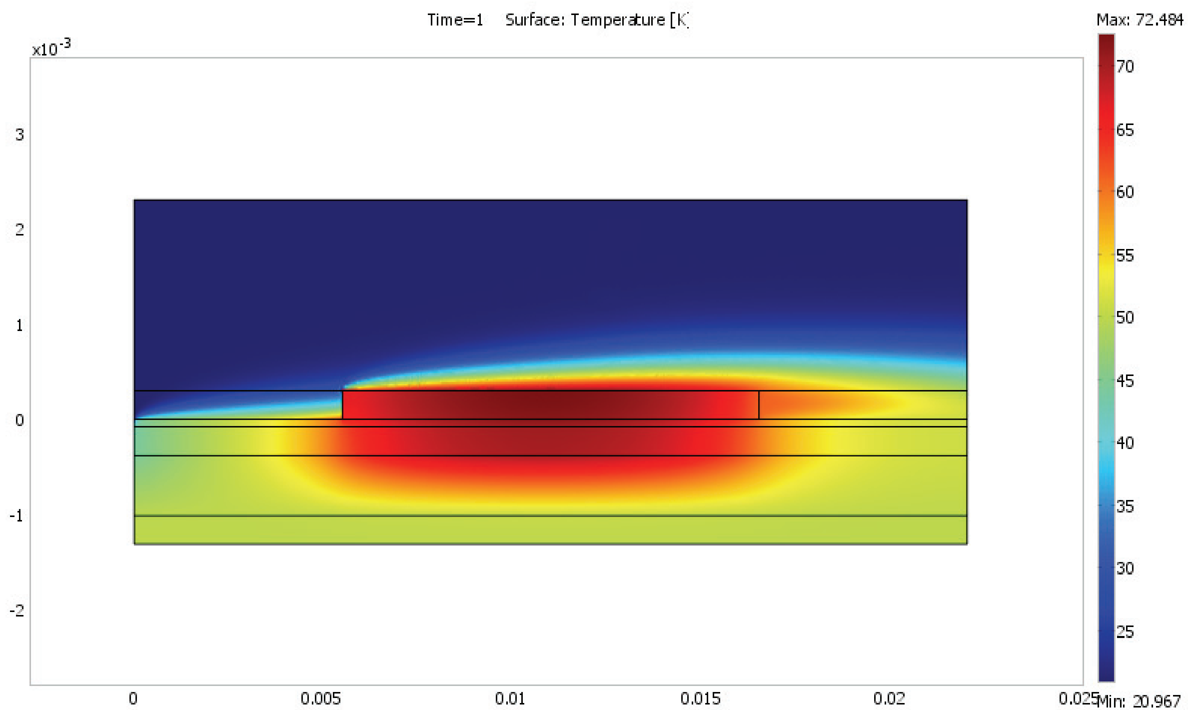


**Figure 35 Temperature conditions in the model when Midel 7131 is circulated above the chip**

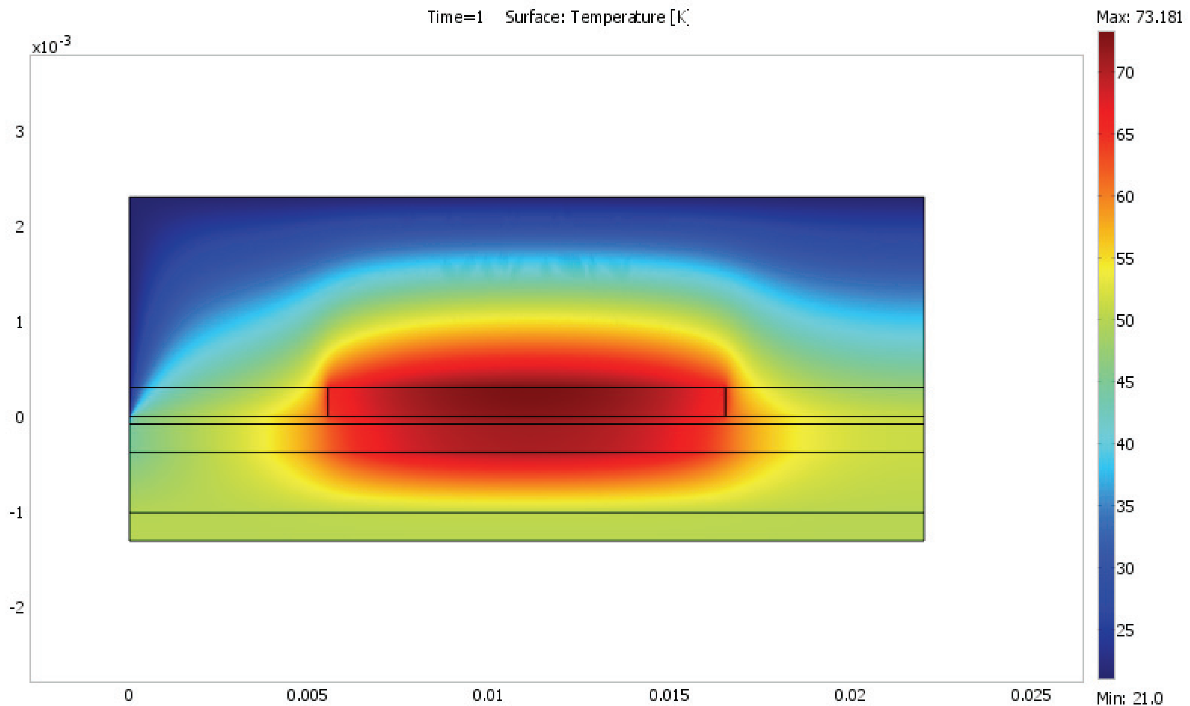


**Figure 36 Temperature conditions in the model when air is circulated above the chip**

As can be seen from Figure 35 and Figure 36 there are differences in the temperature distribution especially on the right top part of the chip. The asymmetrical temperature distributions are caused by the flow direction of the cooling medium. The right top area is further investigated by the Measuring point 1 shown in Figure 34. A transient simulation of the temperature in this point was performed. The result can be seen in Figure 37. It can be seen that although having the two curves are equal in the beginning, the Midel curve will eventually start to rise slower, before settling on a lower stationary temperature compared to the air curve.

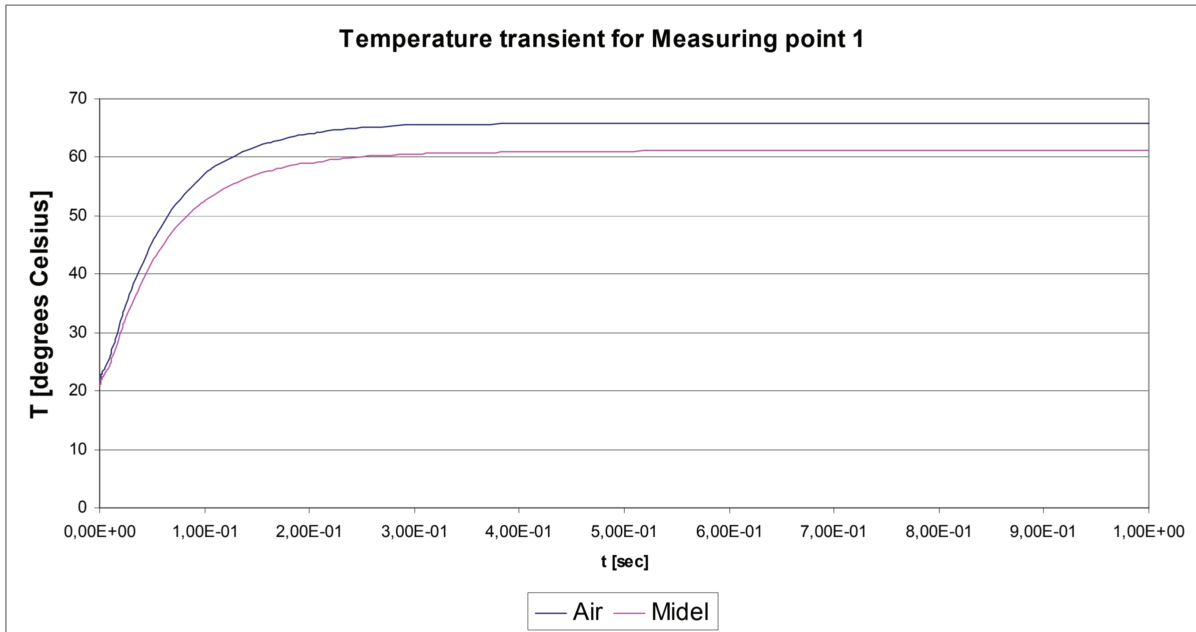


**Figure 37 Temperature transient for Measuring point 1 for respectively air and Midel as cooling medium**

### 5.2.3 Stationary cooling medium

It was decided to do some additional stationary type simulations, in order to establish some connection between the COMSOL simulations and the laboratory measurements. The boundary conditions were changed according to Figure 38. Both sides of the model had thermal insulation as a boundary condition. The simulation thus represents the case where air is standing still above the chip. The temperature of the bottom of the substrate is set to 83 degrees Celsius, in order to approximate the stationary result of this measurement from Figure 17. Measuring point 1 and Measuring point 2 is then meant to approximate the two AD590 temperature sensors, respectively close to and away from the chip.

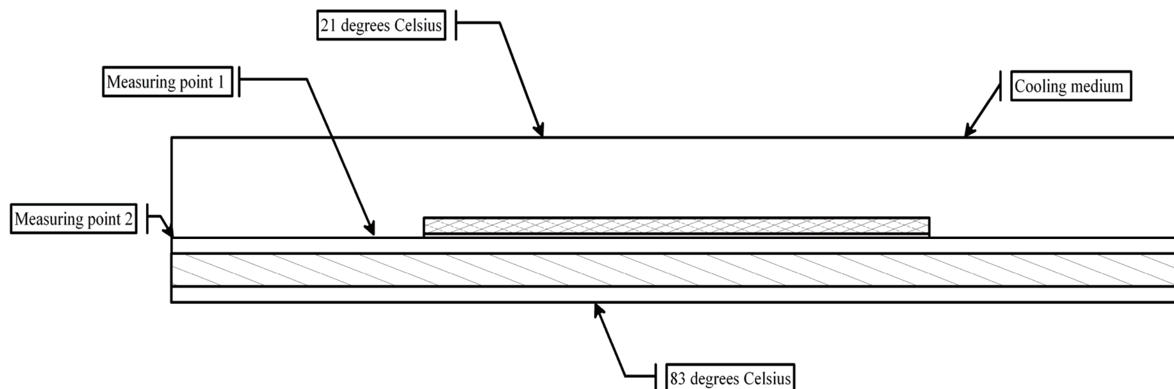


**Figure 38 Overview of the COMSOL model of the chip with boundary conditions**

The results from the simulation can be seen in Figure 39. A comparison with values from laboratory measurements can be seen in Table 16. It can be seen that there is a good correspondence between the measured and simulated values. It should however be noted that Measuring point 1 in the simulation depends significantly on the distance from the chip.

**Table 16 Summary of comparison between simulated and measured values for Measurement points 1 and 2**

| Measuring point | Simulated | Measured in laboratory |
|---|---|---|
| 1 | 92,2 | 92 |
| 2 | 84,2 | 83 |

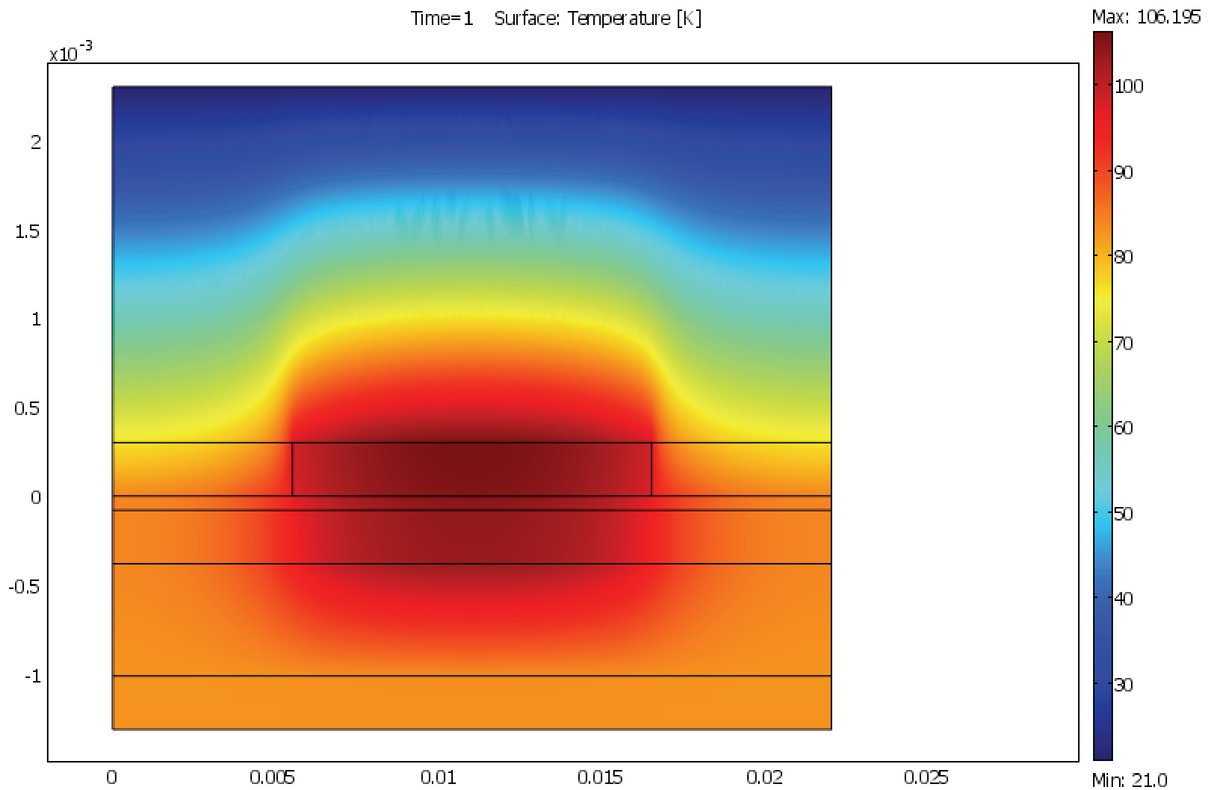


**Figure 39 Temperature conditions in the model for the case with still air above the chip**

# 6 THERMOCAMERA MEASUREMENTS

## *6.1 Initial testing of the thermocamera*

It was decided to record the thermal conditions at the top of the IGBT with a thermocamera. The top of the substrate is covered in a thin layer of Midel 7131. This is in order to get more correct measurements, as the Midel 7131 has an emissivity which is closer to 1 than the silicon. The thermocamera measurements are dependent on the emissivity of the material of which the temperature is measured. Initial testing was done to investigate the emissivity of Midel 7131 in comparison with a type of plastic tape that is regarded to have a high emissivity. Silicon oil was also included in the test for the sake of comparison. The test was performed by applying Midel 7131, silicon oil and the plastic tape to a blank metal piece that was heated. Because of the lower emissivity of the metal, the three test areas on the metal should stand out clearly when looking at them with a thermocamera.

A picture from the thermocamera can be seen in Figure 40. As can be seen from the figure, the three test areas of the metal piece gives almost exactly the same temperature readings. This is an indication that both Midel 7131 and silicon oil has approximately the same emissivity as the plastic tape, which is known to be high. As is expected, the metal surface gives completely wrong temperature readings at the thermocamera because of its low emissivity.

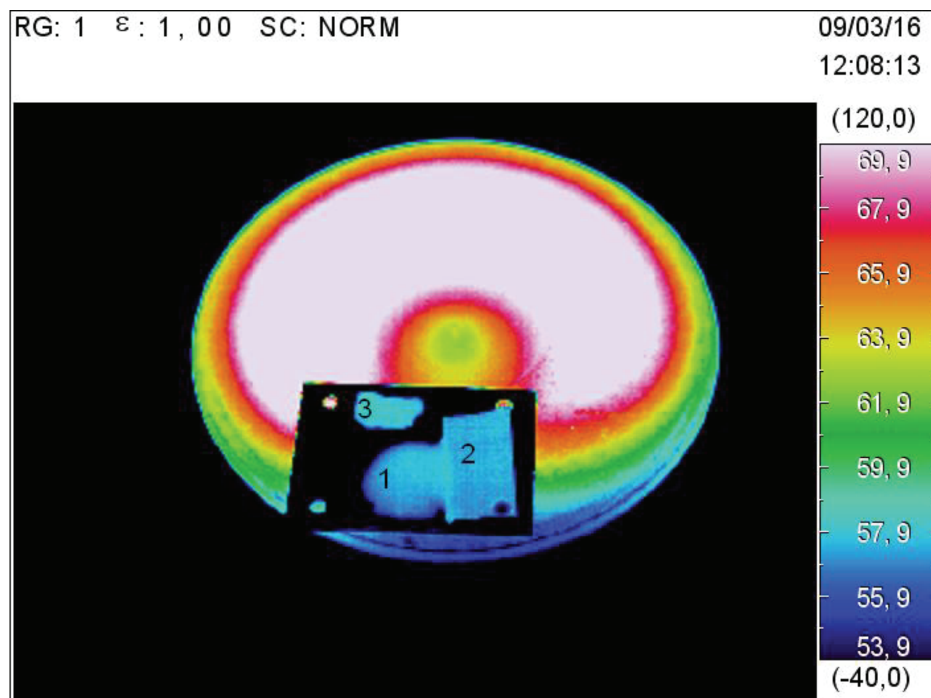


**Figure 40 Thermocamera picture of emissivity test. Area 1 is silicon oil. Area 2 is plastic tape. Area 3 is Midel 7131**

## 6.2 Testing of IGBT module without heatsink

After the thin layer of Midel 7131 had been applied to the top of the substrate, a constant power pulse was applied to one of the IGBT's in the bridgeleg. The thermocamera video is transferred to a computer on the fly and stored in DVD format. A thermal overview for every point in time is thus available by looking at the DVD film afterwards. Additionally thermal images are stored in the camera when steady state temperature has been reached. The thermal images which are stored in the camera contain more information than the DVD film because of the post-processing software available for these images.

One of the images taken in steady state can be seen in Figure 41. It can be seen that when only one of the IGBT's in the module is heated; significant temperature gradients exist in the top of the substrate. This is to be expected, because of the significant distance between the heat source which is the heated IGBT chips and the far end of the module.

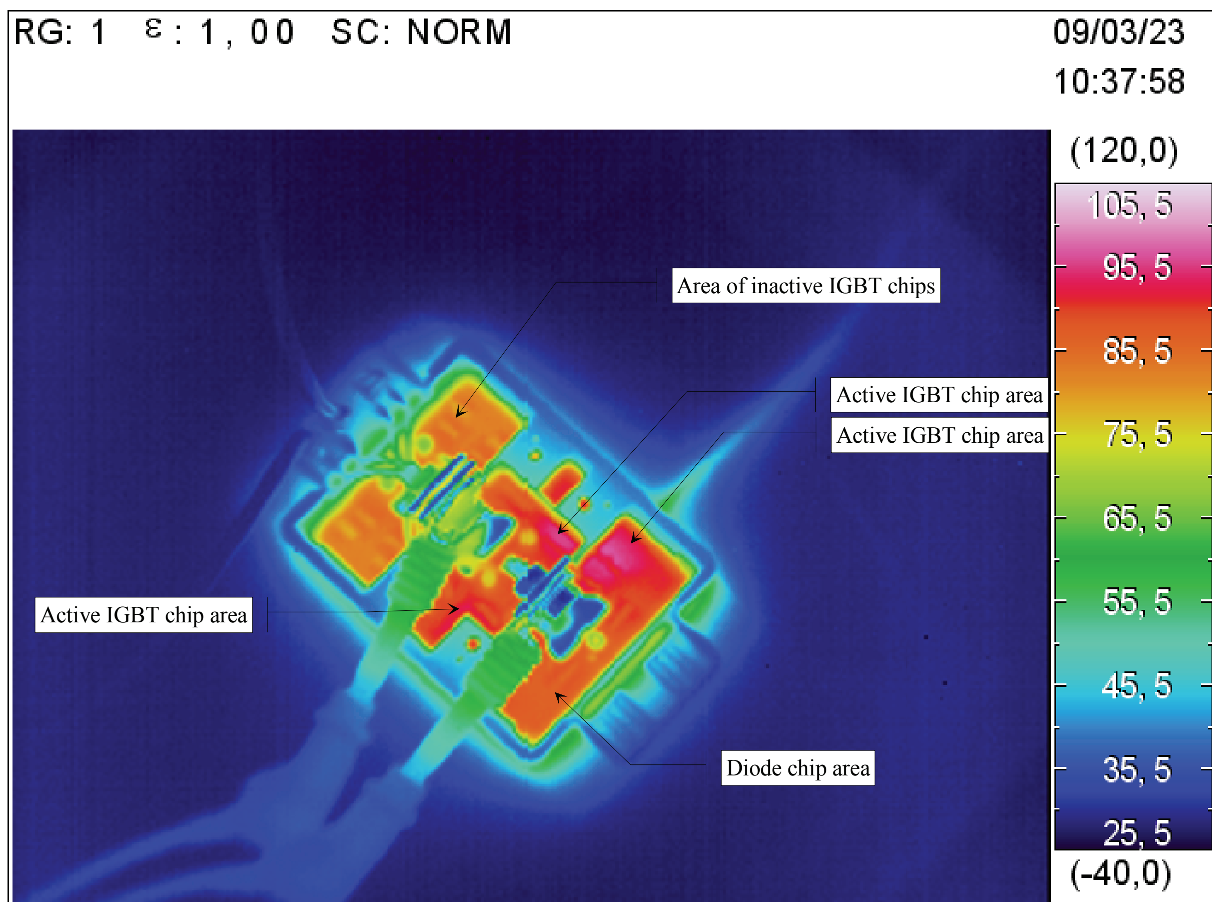


**Figure 41 Thermocamera image of the IGBT module in thermal steady state**

Using post-processing software on Figure 41 shows that the area marked "Active IGBT chip area" has a maximum temperature of about 96,5 degrees Celsius. The area marked "Area of inactive IGBT chips has a temperature of about 83 degrees Celsius, while the "Diode chip area" has a temperature of about 87 degrees Celsius.

It is possible to use discrete readings from the thermocamera recording to construct the temperature transient as seen by the thermocamera. Furthermore, it has been shown earlier in this report that the relation between the chip temperature and the temperature on the underside

of the substrate is primarily given by the thermal resistance between the two points. This makes it possible to estimate the temperature on the underside of the substrate using the thermocamera readings. All three curves can be seen in Figure 42. It can be seen that the calculated and measured temperature transients for the underside of the substrate are quite equal for the first 100 seconds after power is applied.

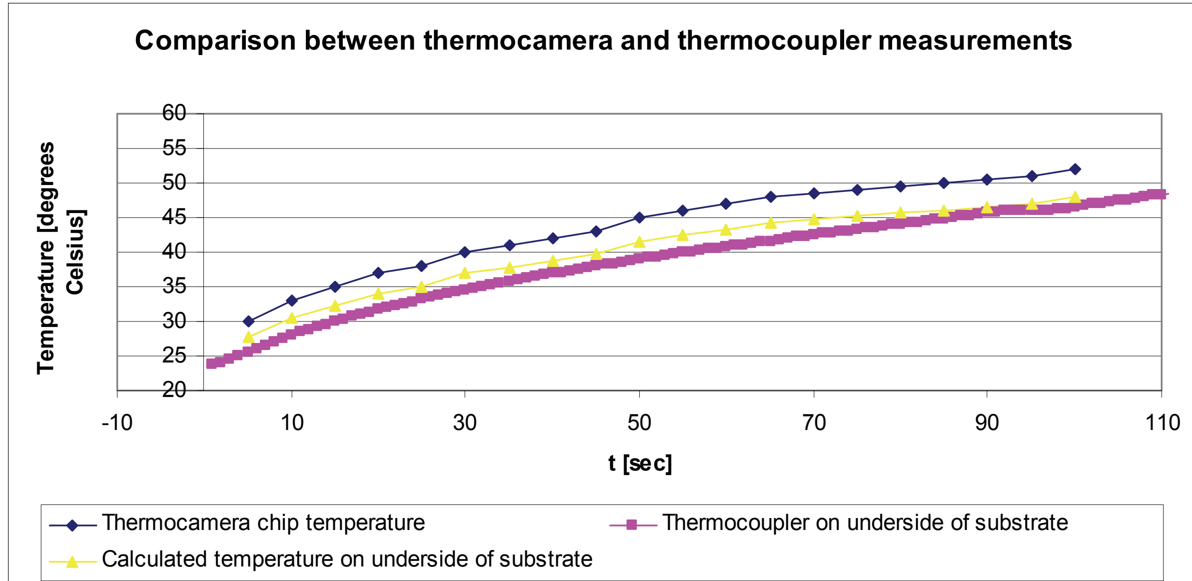


**Figure 42 Thermal transients for the first 100 seconds**

## *6.3 Testing of IGBT module with heatsink*

Since the previous testing was with thermal insulation underneath the module, it was decided that it would be beneficial to look at the opposite case. That is, a case where the cooling underneath the module is quite good. In practice, this was solved by mounting the module on the large heatsink used before. The black paint on the heatsink proved to have a high emissivity, giving a relatively accurate estimation of the temperature when viewed in the thermocamera. Initial testing showed that the heatsink also would attain a relatively uniform temperature distribution. This is likely because of the thermal capacitance of the heatsink being much larger than the thermal resistance of the heatsink. A thermal image of the module with heatsink can be seen in Figure 43.

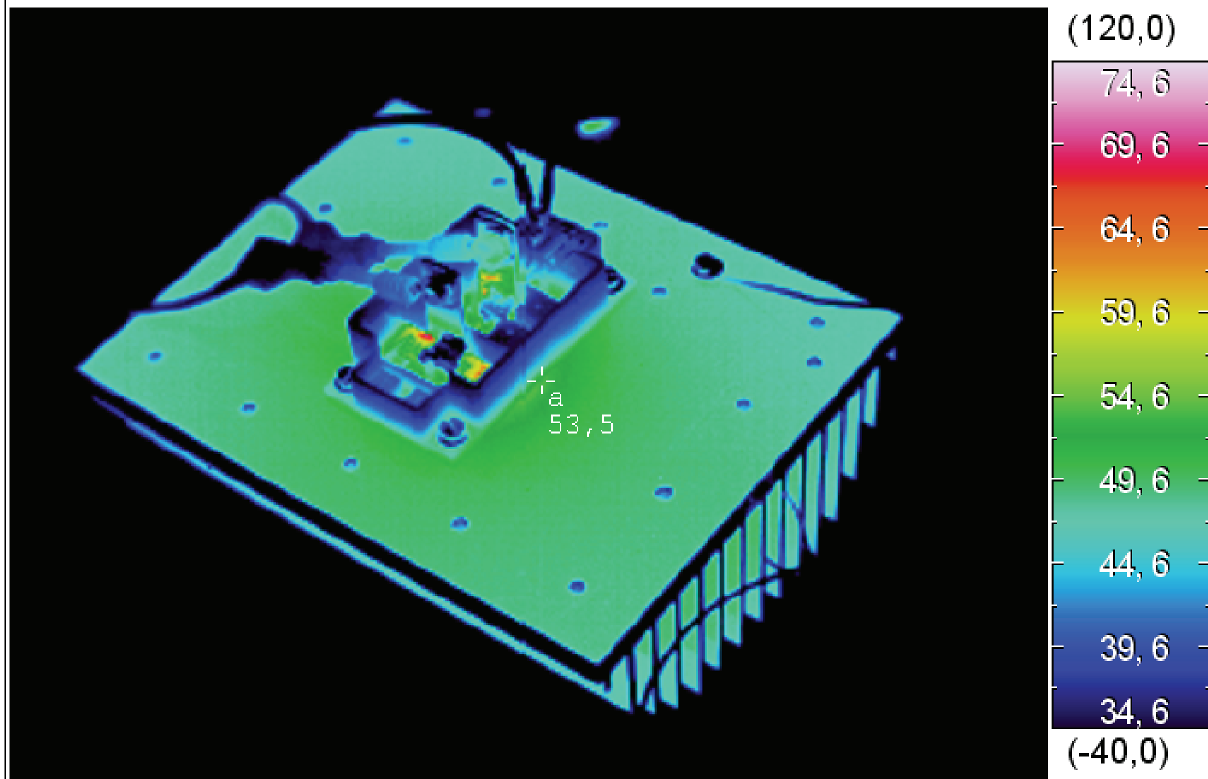


**Figure 43 Thermal image of module with heatsink. Measuring point "a" located on the heatsink close to the module was observed to show good correspondence with the thermocoupler measurements embedded in the heatsink**

When power was applied to the module, the thermal behaviour was somewhat different from the case with thermal insulation underneath the module. A qualitative comparison between Figure 41 and Figure 44 shows that the temperature at the top of the substrate drops of much quicker from the chip when the module is mounted on the heatsink. This shows that the heat transport is larger down through the substrate layers for the heatsink case, as one would expect.

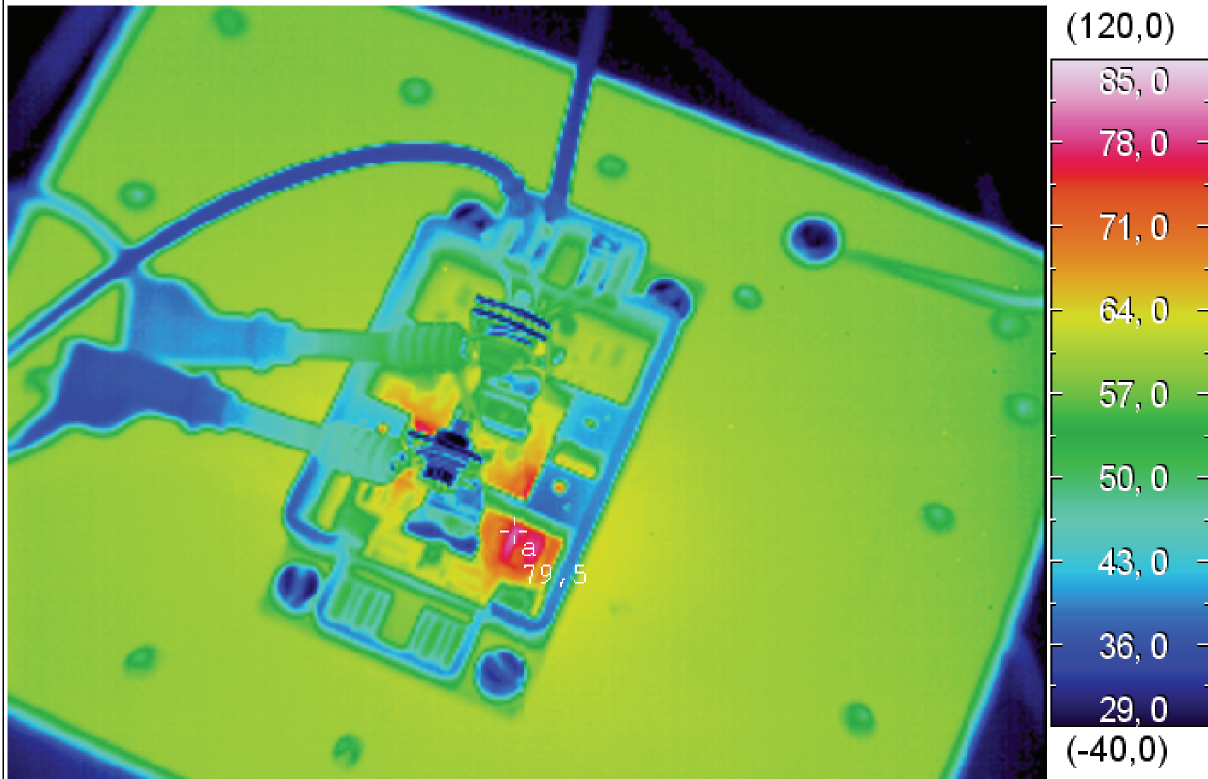


**Figure 44 Thermal image of module with heatsink during testing. Measuring point “a” is located at an IGBT chip**

# 7 STRAY INDUCTANCE CONSIDERATIONS IN THE TEST SETUP

## *7.1 Background of inductance considerations*

During the testing of the IXYS module in the autumn project, it was discovered that significant voltage spikes were produced across the module for some of the combinations of DC-link voltage and transistor current. It is assumed that these voltage overshoots are caused by stray inductance in the circuit between the filtering capacitor mounted on the heatsink and the IGBT module. The principle is illustrated in Figure 45.

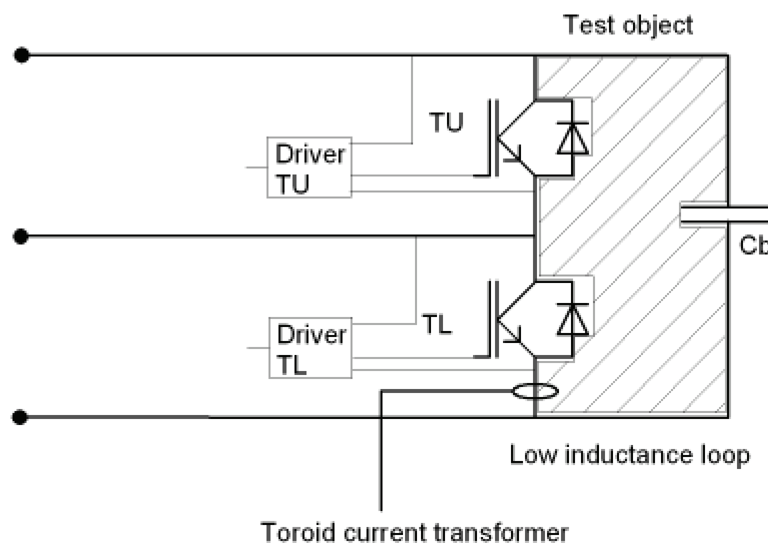


**Figure 45 Drawing of electrical test circuit showing the importance of low stray inductance between filtering capacitor and IGBT module**

In order to obtain more knowledge about lowering the stray inductance in the test setup, a literature study was performed. Minimizing the stray inductance in converter circuits is a prime concern when manufacturing converters. [27] describes reduction of stray inductance in the circuit as a more feasible way to reduce excessive transient voltages in high power applications compared to using snubbers. This is because of the necessary snubber capacitor size, and thereby cost. It is stated that loop area is the main contributor to the stray inductance in the circuit, and may be a more cost-effective way of reducing transient overvoltages.

## *7.2 Inductance calculation methods*

Skibinski [25] gives an analysis of different connection configurations with regard to stray inductance, and outlines a design methodology for planar bus structures for obtaining minimum stray inductance. When speaking of the inductance of conductors, one makes a distinction between the self inductance and mutual inductance of the conductors. Self inductance will be a function of the conductor itself, while mutual inductance will be a function of the geometric placement of several conductors with respect to each other.
[25] shows that a bus bar will have a lower self inductance than a round conductor, with the self inductance of the bus bar given by the formula (19) below and the condition that the

busbar is located so far away from the return path of the current so that the mutual inductance can be regarded as zero.

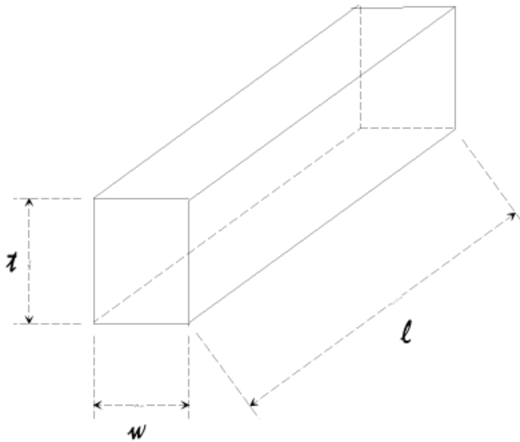


**Figure 46 Principal rectangular conductor**

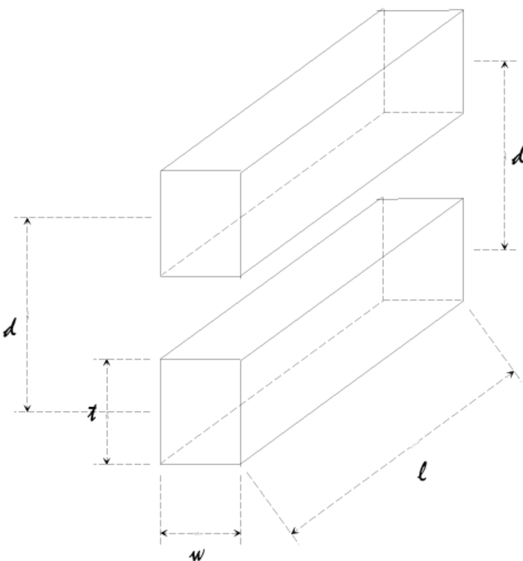


**Figure 47 Geometric placement of two rectangular conductors**

$$L_{bar,DC} = 0{,}002 \cdot l \cdot (2{,}303 \cdot Log_{10}\left[\frac{2l}{w+t}\right] + 0{,}5 + 0{,}2235 \cdot \left[\frac{w+t}{l}\right]\ ) \tag{19}$$

In formula (19) L is given in μh and l, w, and t is given in centimetres.

While [27],[28] gives the formula for self inductance of the bus bar for low frequencies as

$$L_i = \frac{\mu_0 \mu_r}{8\pi} l \tag{20}$$

In [25], a optimal width/length ratio for “short” bus bars is discussed. If we assume that the notion for “short” busbar also applies for the IXYS test setup, it is worth noticing that a width/length ratio of 1:1 is necessary to minimize the stray inductance, while a ratio of 2:1 gives optimum minimization.

The self inductance of a conductor is combined with the mutual inductance of the conductor arrangement. When two parallel conductors are conducting current in the same direction, the mutual inductance will add up, while if they are conducting in the opposite direction the mutual inductance will subtract. For our laboratory setup the current in the parallel conductors will run in opposite direction, and the mutual inductance will thereby subtract from the self inductance for each conductor, giving a lower total inductance. A maximization of mutual inductance will therefore mean a minimization of total inductance in the test setup. This can be seen easily in the formula for total inductance (21) [25, 29], given for opposite current directions.

$$L_{total} = L_1 + L_2 - 2M \tag{21}$$

When calculating the mutual inductance of two parallel busbars, [26] gives the central filament approach, where the busbar area is replaced by an equivalent central conductor filament. This method is also quoted by [25].

[27] and [28] cites an approximate formula for calculation of the total self inductance for the two bus bar configuration with return current in one of the bus bars, given some conditions regarding the geometric properties of the bus bars. Since papers [27] and [28] calculates the internal inductance and external inductance for the whole bus bar configuration, direct comparison with the mutual inductance approach in [25] becomes difficult.

Since both [27] and [28] cites [29] as a reference, the mutual inductance approach in [29] is used for direct comparison of the formulas in [25] and [29]. According to [29] the self inductance of a rectangular conductor as given in Figure 46 can be calculated by formula (22)

$$L = \frac{\mu \cdot l}{2\pi} \cdot (\ln(\frac{2l}{w+t}) + \frac{1}{2} - \Delta e) \tag{22}$$

Δe is a parameter dependent on the geometry of the conductor, given by Table 17 [29].

**Table 17 Δe as function of t/w [29]**

| t/w | 0 | 0,25 | 0,50 | 0,75 | 1,00 |
|---|---|---|---|---|---|
| Δe | 0 | 0,00249 | 0,00211 | 0,00184 | 0,00177 |

Likewise, the mutual inductance calculations of [25] and [29] are compared, shown respectively in formula (23) and formula (24)

$$M = 0{,}002 \cdot l \cdot \left[ \ln\left( \frac{l}{d} + \sqrt{1 + \frac{l^2}{d^2}} \right) - \left( \sqrt{1 + \frac{d^2}{l^2}} + \frac{d}{l} \right) \right] \tag{23}$$

In formula (23) M is given in μh, and l and d in centimetres.

$$M = \frac{\mu \cdot l}{2\pi} \cdot \left[ \ln\left(\frac{l}{d}\right) - 1 + \Delta k + \frac{d}{l} - \frac{1}{4}\left(\frac{d}{l}\right)^2 \right] \tag{24}$$

Δk is a parameter dependent on the geometric configuration of the conductors, given by Table 18 [29].

**Table 18 Δk as function of w/d and t/w [29]**

| w/d | 0 | 0,5 | 1,0 | 2,0 | 10 |
|---|---|---|---|---|---|
| Δk for t/w=0 | 0 | 0,0199 | 0,0708 | 0,2107 | 1,0787 |
| Δk for t/w=0,5 | 0 | 0,0152 | 0,0560 | 0,1754 | - |
| Δk for t/w=0,75 | 0 | 0,0092 | 0,0359 | - | - |
| Δk for t/w=1,0 | 0 | 0,0005 | 0,0065 | - | - |

Inductance calculation of the two bus bar problem is also possible with finite element (FEM) analysis. The finite element program calculates the magnetic field distribution for the geometry. The current density is given as a parameter to the program. Since the conductor area is known, the current can be calculated by (25)

$$I = J \cdot A \tag{25}$$

The geometry is then meshed, and the differential equations governing the problem are solved. After the solution has been found, the integral of the magnetic energy of the integration area can be read from the program. Given the magnetic energy, the self inductance of the conductors can be found by equation (26) and the mutual inductance of the two-conductor configuration can then be found by equation (27) [30]

$$L = 2 \cdot \frac{W_{magn}}{I^2} \tag{26}$$

$$M = \frac{W_{magn} - \frac{1}{2} \cdot L_1 \cdot I_1^2 - \frac{1}{2} \cdot L_2 \cdot I_2^2}{I_1 \cdot I_2} \tag{27}$$

It should be noted that the equations in this chapter are based on uniform current distribution in the conductors, hence no skin- or proximity effects. At high frequencies these effects will lead to a reduction of the stray inductance of the two bus bar configuration [25].

## 7.3 COMSOL Multiphysics modelling for assessment of stray inductance

For case of comparison, two cases of bus bar configuration were investigated for stray inductance. Both configurations are geometrically possible to realize for the IXYS module test setup. The geometry of each configuration is drawn in COMSOL Multiphysics, and the corresponding current density for a current of 1A is calculated according to (25). Given the correct boundary conditions and subdomain settings, the finite element problem is then meshed and solved.

COMSOL Multiphysics allows direct subdomain integration of the magnetic energy density. The magnetic energy is then used in (26) for the case of one conductor conducting a current, and in (27) for the case when both conductors are conducting current. Minding the correct sign for opposite current directions, (21) will give the total inductance of the configuration. The geometric configuration for two bus bars side by side can be seen in Figure 48. The bus bars are given as 9 cm long, as this is approximately the distance from the capacitor connections to the power terminals of the IXYS module in the test setup. The corresponding plot of magnetic flux lines can be seen in Figure 49.

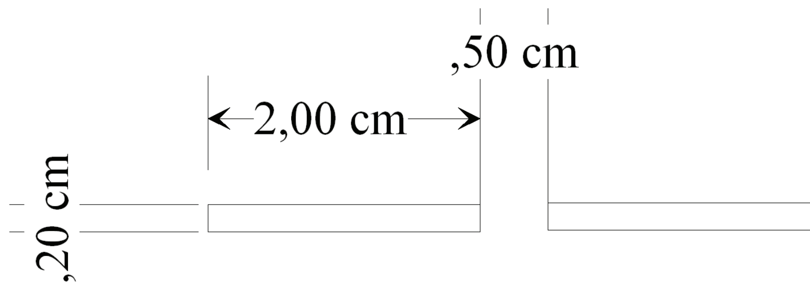


**Figure 48 Geometric configuration for two bus bars side by side**

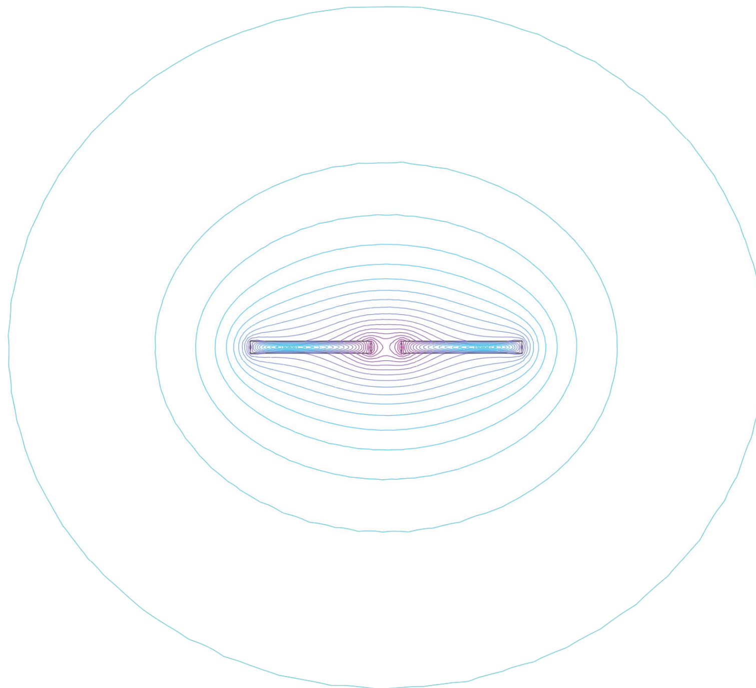

**Figure 49 Magnetic flux lines for two bus bars side by side**

Using the subdomain integration function of COMSOL Multiphysics, the magnetic energy can be found, shown for this case in Table 19.

**Table 19 Magnetic energy integral for two bus bars side by side**

| Configuration | Magnetic energy integral |
|---|---|
| Conductor 1 carrying a current of 1A | 4.179009e-7 |
| Conductor 2 carrying a current of -1A | 4.185004e-7 |
| Both conductors carrying a current of 1A in opposite directions | 3.122193e-7 |

The magnetic energy integral gives the inductances in the circuit according to (24), (25) and (21). The inductances for two bus bars side by side were calculated and are shown in Table 20.

**Table 20 Inductance calculation for two bus bars side by side**

| Variable | Description | Size [uH] |
|---|---|---|
| $L_1$ | Self inductance, conductor 1 | 0,8360 |
| $L_2$ | Self inductance, conductor 2 | 0,8360 |
| M | Mutual inductance between the conductors | 0,5236 |
| L | Total inductance | 0,6244 |

The geometric configuration for two bus bars over each other can be seen in Figure 50.The bus bars are given as 9 cm long, as this is approximately the distance from the capacitor connections to the power terminals of the IXYS module in the test setup. The corresponding plot of magnetic flux lines can be seen in Figure 51.

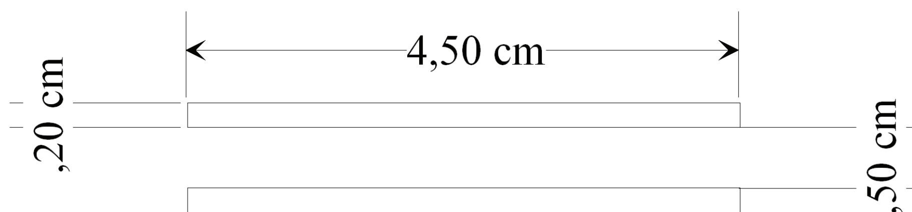


**Figure 50 Geometric configuration for two bus bars over each other**

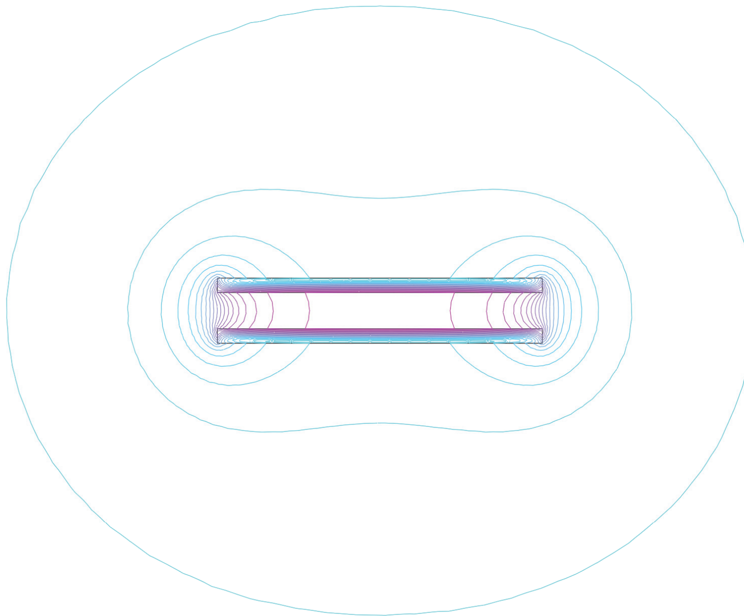

**Figure 51 Magnetic flux lines for two bus bars over each other**

Using the subdomain integration function of COMSOL Multiphysics, the magnetic energy can be found, shown for this case in Table 21.

**Table 21 Magnetic energy integral for two bus over each other**

| Configuration | Magnetic energy integral |
|---|---|
| Conductor 1 carrying a current of 1A | 3.426471e-7 |
| Conductor 2 carrying a current of -1A | 3.426007e-7 |
| Both conductors carrying a current of 1A in opposite directions | 7.232628e-8 |

The magnetic energy integral gives the inductances in the circuit according to (24), (25) and (21). The inductances for two bus bars over each other were calculated and are shown in Table 22.

**Table 22 Inductance calculation for two bus bars over each other**

| Variable | Description | Size [uH] |
|---|---|---|
| $L_1$ | Self inductance, conductor 1 | 0,6852 |
| $L_2$ | Self inductance, conductor 2 | 0,6852 |
| M | Mutual inductance between the conductors | 0,6129 |
| L | Total inductance | 0,1446 |

Comparing the total inductance for the two geometric configurations, it can be seen that the inductance for the case for two bus bars over each other is only 0,1446 / 0,6244 = 23,2% of the inductance for the case for two bus bars side by side. As was expected, the configuration with two bus bars over each other was significantly better than the configuration with two bus bars side by side.

# 8 PASSIVE PRESSURE TESTING OF COMPONENTS

## 8.1 Description of passive pressure testing

Part of the project consisted of taking part in the assessment of some components that had been subjected to pressure testing in Midel 7131 oil at 300 bars. The pressure testing was so-called passive tests, meaning that no power was applied to the components under testing. The description of the full test program can be found in [32]. Only the components relevant for the IXYS test setup will be treated here. The components were pressurized for 61 days at 300 bars. The pressurization and depressurization was done relatively fast at respectively 20 minutes and 7 minutes. This is significantly faster than in a real world case, where the descent from surface to the bottom of the sea may take hours. The test is therefore likely to represent an absolute worst case regarding pressure changes with regard to time. The components in the test relevant for the IXYS test setup is

- IXYS MII400-12E4 IGBT module, modified for pressure equalization
- ICW capacitor
- EFI gatedriver, modified for pressure tolerance

The modification done to the IXYS module is based on the experience gained in previous pressure testing, and consists of drilling holes in the sides of the module, to let the oil penetrate into the module and equalize the pressure differences. A picture of the modified IXYS module can be seen in Figure 52. The modification of the EFI gatedriver is described in [21] and consists mainly of replacement of pressure-intolerant capacitors and transformers. A picture of the oil filled container with test objects inside can be seen in Figure 53.

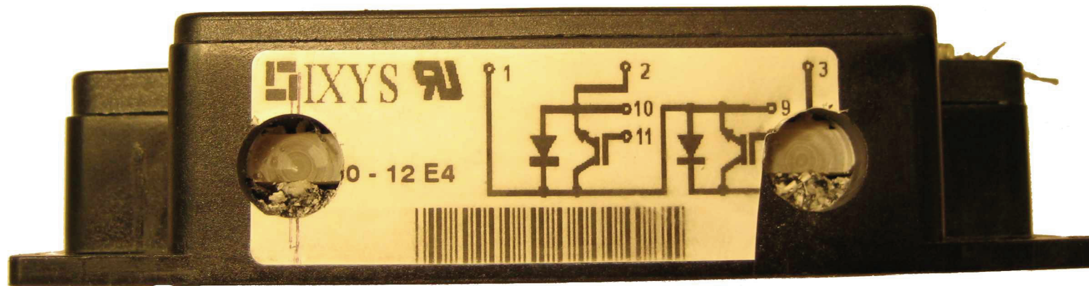


**Figure 52 IXYS module modified for pressure tolerance [32]**

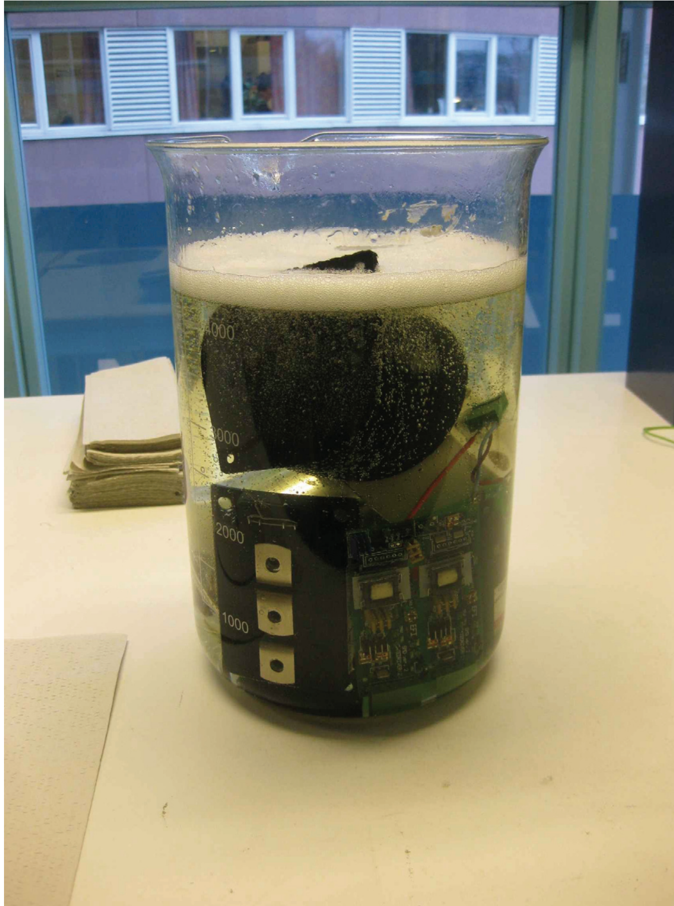

**Figure 53 Picture of the oil-filled glass with tested components inside [32]**

## 8.2 Results from passive pressure testing

The tested components were investigated for mechanical damage, and the correct electrical operation was verified. None of the components showed signs of mechanical failure significant enough to affect electrical operation. The electrical testing of the components is well described in [32], but it was decided to perform some additional double-pulse switching on the IXYS module to compare the waveforms with the reference module. Table 23 shows a summary of the effects of the passive pressure testing on the components.

**Table 23 Summary of passive pressure testing of components**

| Component | Mechanical effects | Electrical effects |
|---|---|---|
| IXYS IGBT module | Some movement of the gel covering the chips. The gel does not dissolve in the oil. | None, electrical testing passed. |
| ICW capacitor | Cracking on top of lid. The resin covering the active components does not dissolve in the oil. | None, electrical testing passed. |
| EFI gate driver | No visible effects | None, electrical testing passed. |

Results from the double-pulse testing can be seen in Figure 54 to Figure 56.

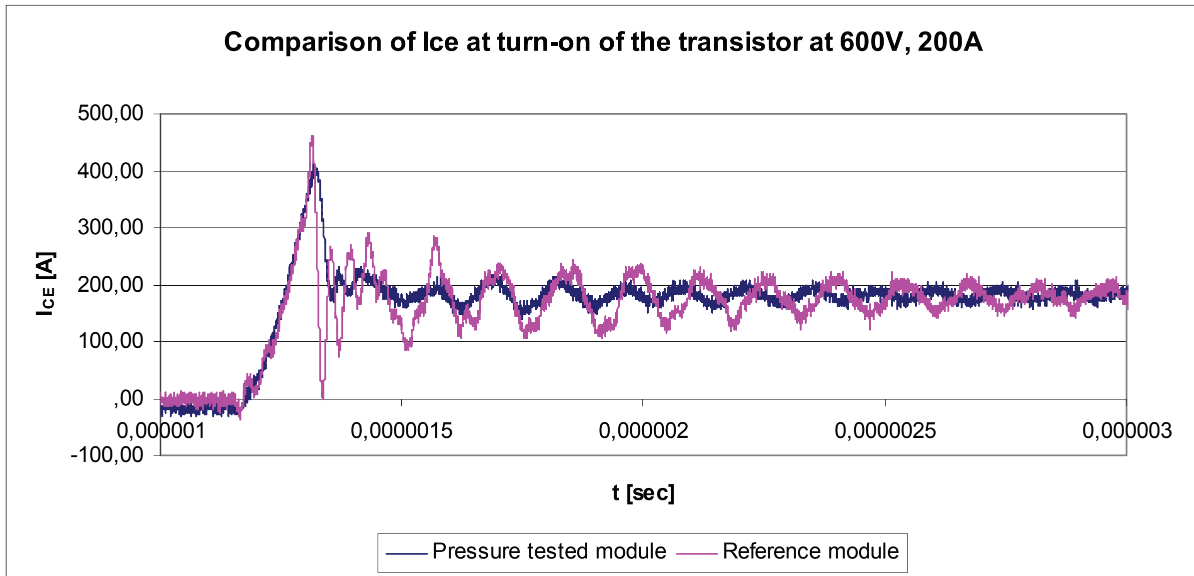


**Figure 54 Comparison of Ice at turn-on of the transistor at 600V, 200A**

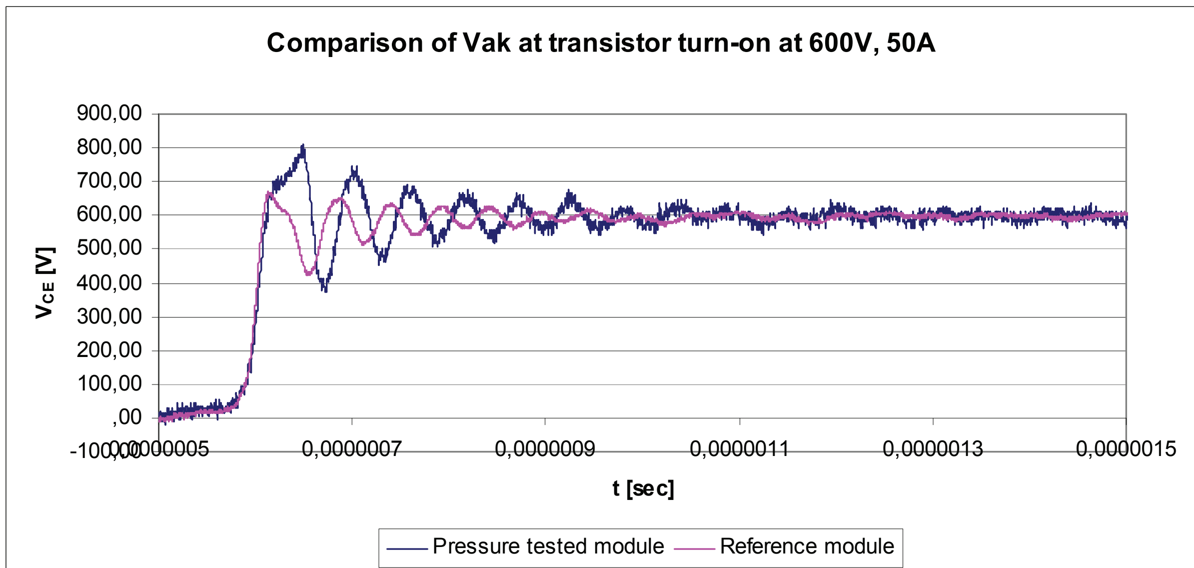


**Figure 55 Comparison of Vak at turn-on of the transistor at 600V, 50A**

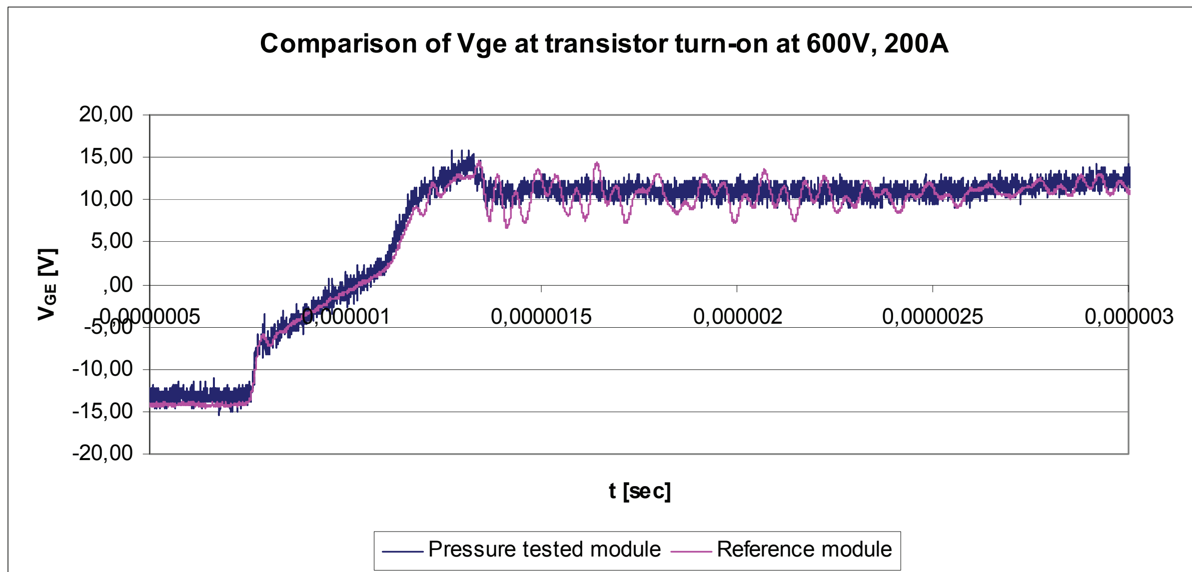


**Figure 56 Comparison of Vge at turn-on of the transistor at 600V, 200A**

As can be seen from Figure 54 to Figure 56, the waveforms for the pressure tested and the reference module are quite equal, but the reference module is actually noisier than the pressure tested module.

# 9 SWITCHING OF OPEN MODULE IN OIL

## 9.1 Description of test setup for double-pulse switching

The test setup used for the IGBT when it is tested in liquid is basically the same that was used when the reference testing was done in the autumn project; this is described in [21]. For the sake of completeness, the description of the basic test setup is shown again here.

The testing of the IGBT module is realized by building a test rack consisting of heatsink, gatedriver, power connections and capacitor. The test rack is shown in Figure 57. A picture of the open module prepared for immersion in oil is shown in Figure 58. The test setup for testing the open module in oil can be seen in Figure 59. The electrical drawing of the test setup is shown in Figure 45. For the double-pulse switching, the current control part of the setup is replaced by a signal generator. The IGBT is mounted on top of the heatsink, with the capacitor connections in close proximity, in order to make the inductance of this loop as small as possible. As seen in the figure, metal rails are mounted on the sides of the heatsink, for easy mounting of gatedriver and power connections. These rails are also important for steady placement of the test rack inside the oil filled vessel, for the tests conducted at 1 bar pressure. Current measuring is done by a toroid transformer placed around the negative power terminal of the IGBT module, between the module and the capacitor. Connections for further measurements can be seen in the background of Figure 57; these include measurements of $V_{GE}$, $V_{CE}$ and $V_{AK}$ for the lower IGBT of the bridge leg which is tested.

A SINTEF laboratory converter is connected to the module to be tested through an inductive load, as seen in Figure 60. An air core inductor is used as a load during the double pulse switching, while an iron core coil is used for continuous switching.

The converter is well described in [3], and a circuit diagram can be found in Appendix C. The laboratory converter setup also contains a gate driver interface card, which is responsible for the interface between the control system and the power circuit switches. This card also contains the cross conduction interlock logic and status signal monitoring [17]

The gate driver interface card on the laboratory converter is not modified, but the gatedriver on the test rack is connected to it, substituting one of the drivers of the laboratory converter. It is important that the wiring between the driver interface board and the gatedriver on the test rack is kept as short as possible, because of possible induction of noise in the wiring.

The gatedriver to be used is a driver developed at SINTEF for laboratory use, the so-called EFI-driver. The driver is described in [4]. It is important that the gate resistance of the gatedriver is modified in accordance with the requirements of the IGBT under testing. The gatedriver is modified in order be fully pressure tolerant.[15],[21] It is then mounted on the heatsink, so that it will be immersed in oil during testing. A circuit diagram for the gatedriver can be found in Appendix B.

For the double-pulse switching, a signal generator is utilized. The double-pulses generated by this device are in turn routed through a jumper card, which gives the possibility of connecting the signal from the signal generator to the different gate drivers.

For the continuous switching, a current control card is connected to the driver interface card instead of the signal generator. This current control card will in turn generate a pulse-width modulated signal to the driver cards of the IGBT's that are in use. A circuit diagram for the current control card can be found in Appendix D.

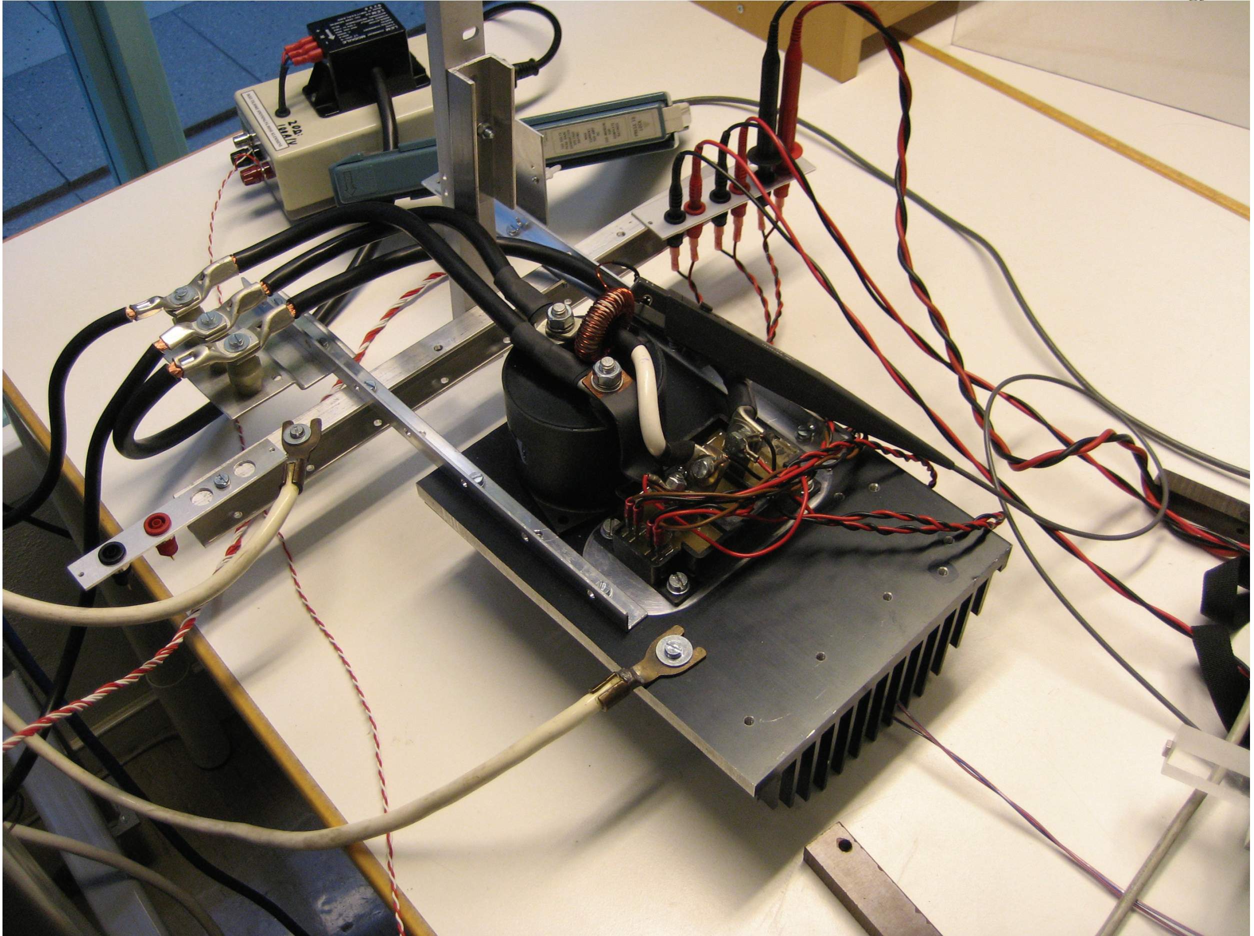

**Figure 57 Picture of the test rack for testing in air with IGBT module, smoothing capacitor, heatsink and connections**

The test setup is described in more detail in the report from the autumn project [21], and the laboratory protocol from the introductory testing in the autumn [20].

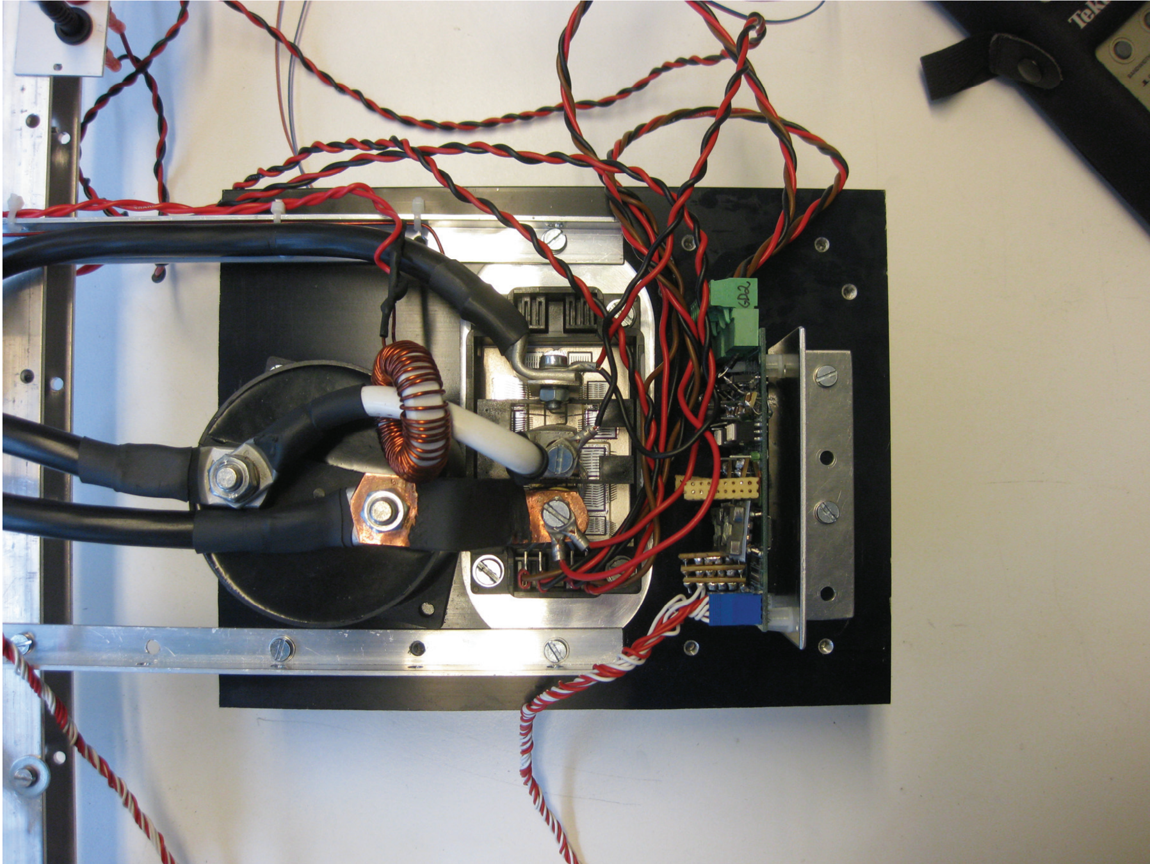

**Figure 58 Close-up picture of the IGBT and smoothing capacitor with connections and current measuring toroid. Note that the gatedriver is moved onto the heatsink for testing in oil**

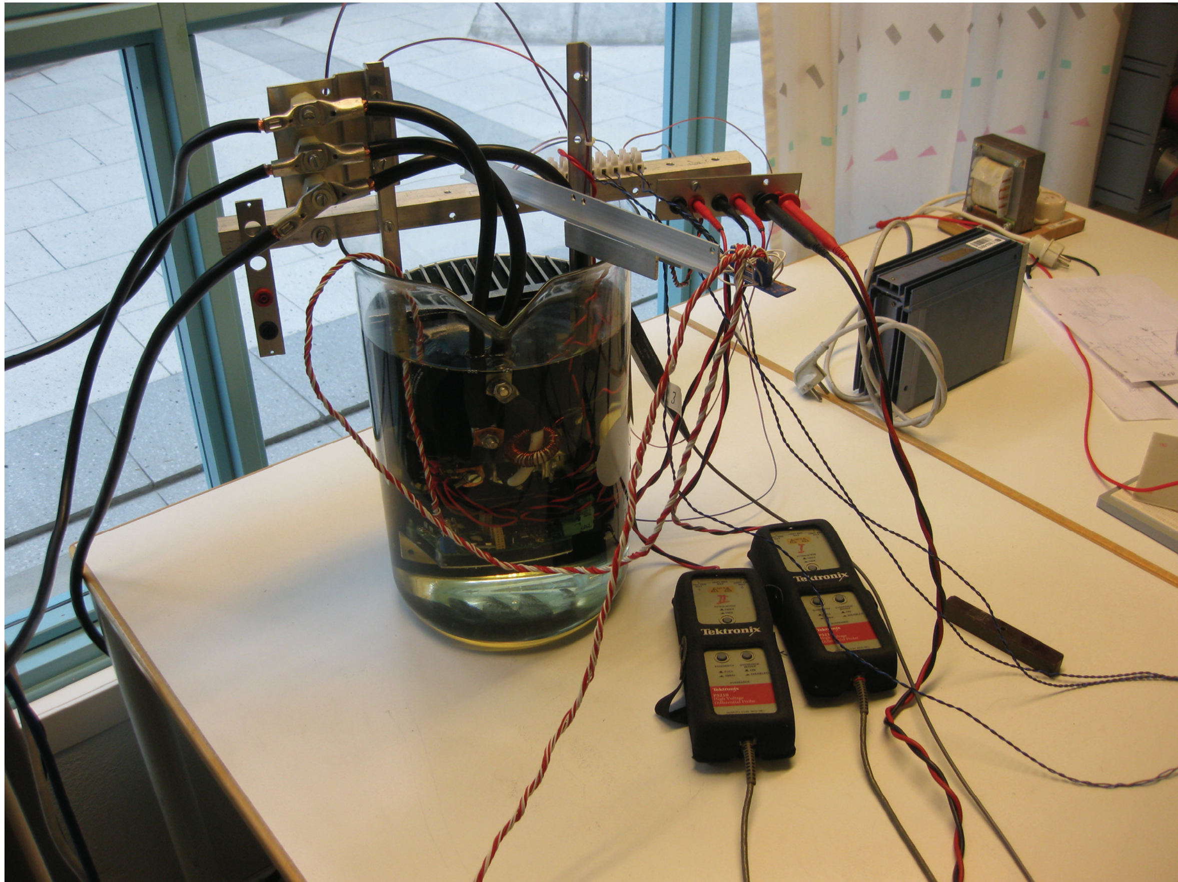


**Figure 59 Picture of  test setup for testing the open IGBT module in oil**

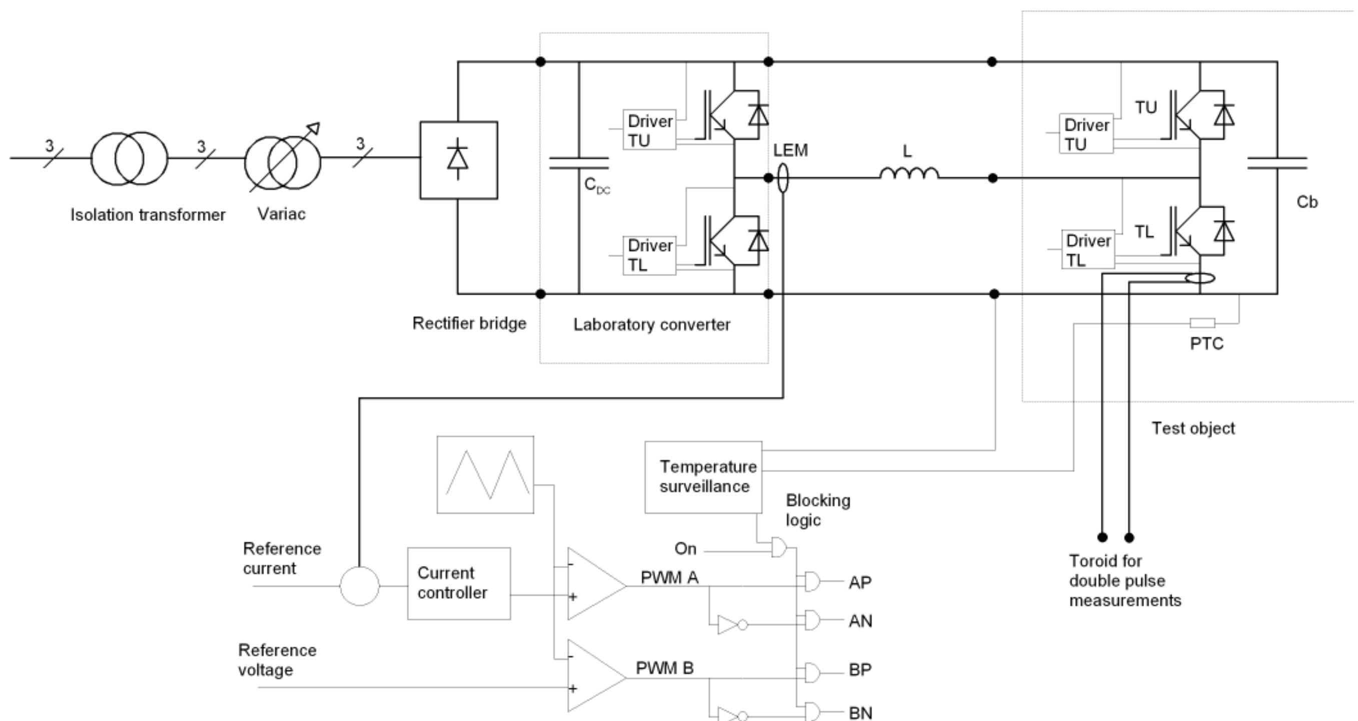


**Figure 60 Electrical drawing of the test setup. For the double-pulse switching, the current control part of the setup is replaced by a signal generator**

## 9.2 Description of double-pulse switching

The measuring equipment and data acquisition methods used during the double-pulse switching are the same as were used during the autumn project. The reader is therefore referred to the autumn project [21] for this information.

The first test that were performed on the IGBT were so-called double-pulse switching. A generic example of waveforms during this kind of testing is shown in Figure 61. The purpose of this test is foremost to gather information about the IGBT's behaviour during turn-on and turn-off, while the device is conducting current. Points of interest will therefore be at first turn-off and second turn-on of the transistor, and possibly second turn-off. The time between the two pulses is adjusted such that the current at first turn-off and second turn-on is approximately equal. During this testing an air core coil is used as a load inductor. Tests are conducted for increasing values of voltage and current..

The values of $V_{GE}$, $V_{CE}$, $I_{CE}$ and $V_{AK}$ are recorded by oscilloscope for each test point. [21]

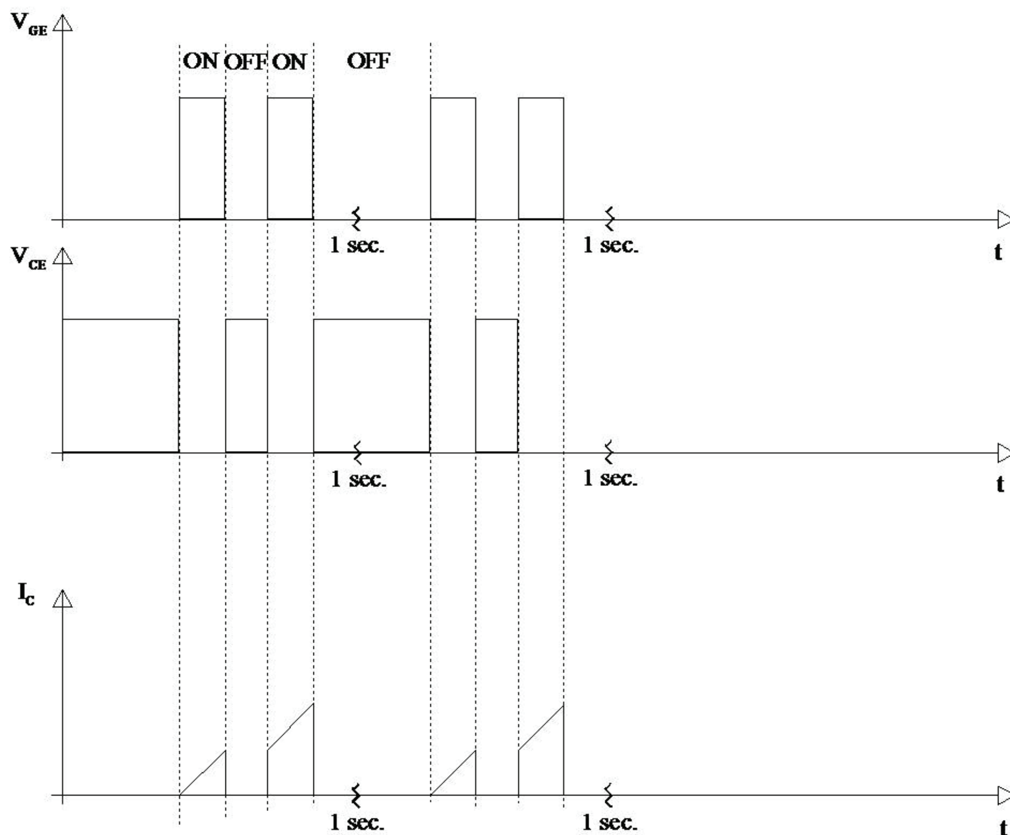


**Figure 61 Principal waveforms during double-pulse switching**

## 9.3 Description of test programme for double-pulse switching of open module in oil at 25 degrees Celsius

The double-pulse test program is summarized in Table 24. "On" denotes a capture of a turn-on of the transistor at the relevant voltage and current. "Off" denotes a capture of a turn-off of the transistor at the relevant voltage and current. It should be noted that measurements of 200A and over can be troublesome because of the short-circuit protection found in the gate drivers. This problem is described in detail in [21].

**Table 24 Summary of double-pulse test program**

| $I_{CE}$ | 50A | 100A | 200A | 400A |
|---|---|---|---|---|
| $V_{DC}$ | | | | |
| 50V | On/Off | On/Off | | |
| 100V | On/Off | On/Off | On/Off | |
| 200V | On/Off | On/Off | On/Off | |
| 400V | On/Off | On/Off | On/Off | |
| 600V | On/Off | On/Off | On/Off | Off |

## 9.4 Results from double-pulse switching in oil at 25 degrees Celsius

Before the open module was put into oil it was switched at reduced voltage in air to verify correct switching operation. Because the withstand voltage of the open module in air is unknown, the instantaneous switching voltages had to be limited. The module was therefore set to switch at 50V and 10A. The test was repeated immediately after the module was immersed in oil in order to observe possible differences. It was seen that there was very little difference between the waveforms before and after immersion in oil. An example can be seen in the diode voltage waveform in Figure 62. It can be seen that the diode voltage oscillations when testing in oil has a bit lower frequency in the later part of the transient and they are more damped compared to when testing in air.

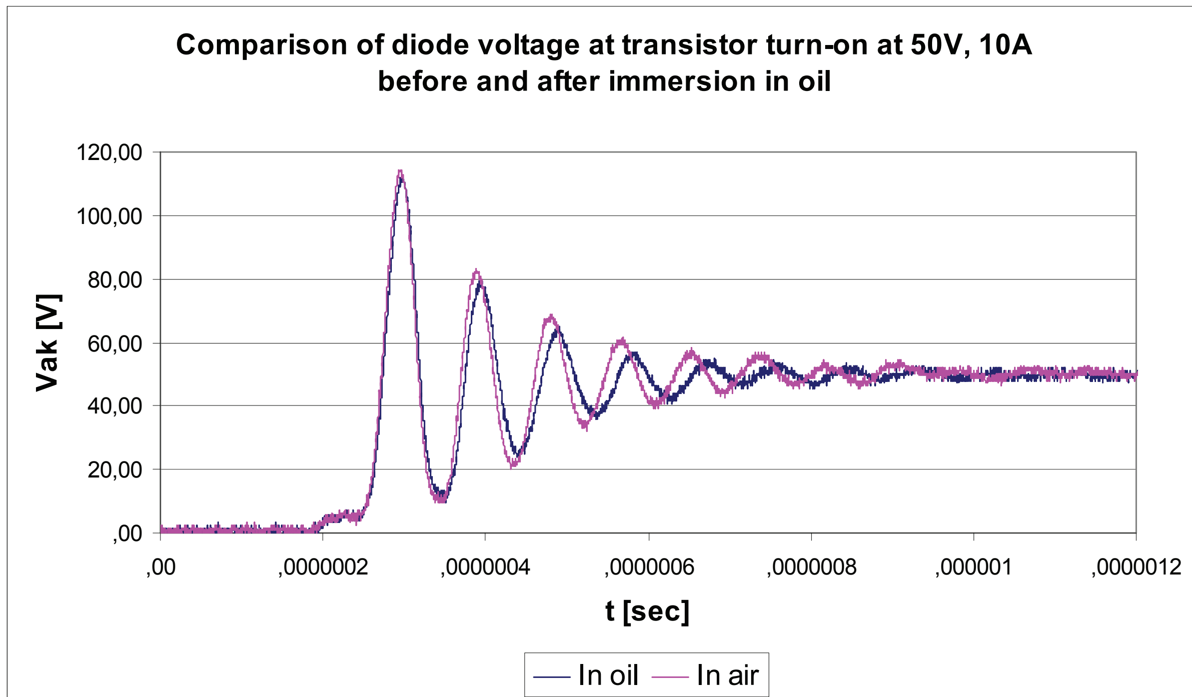


**Figure 62 Diode voltage waveform before and after immersion of the module in oil**

Since the module had no significant difference in the switching waveforms directly after immersion in oil, the double-pulse switching at higher voltages and currents could be started. The test programme was performed according to Table 24. Comparison with the reference testing of a standard module in air done in the autumn showed relatively little difference between the two modules. Since the waveforms were generally relatively equal, emphasis will be put on the observable differences in the following. Typical oscilloscope captures for a test point, in this case 200V and 100A, can be seen in Figure 63 and Figure 64.

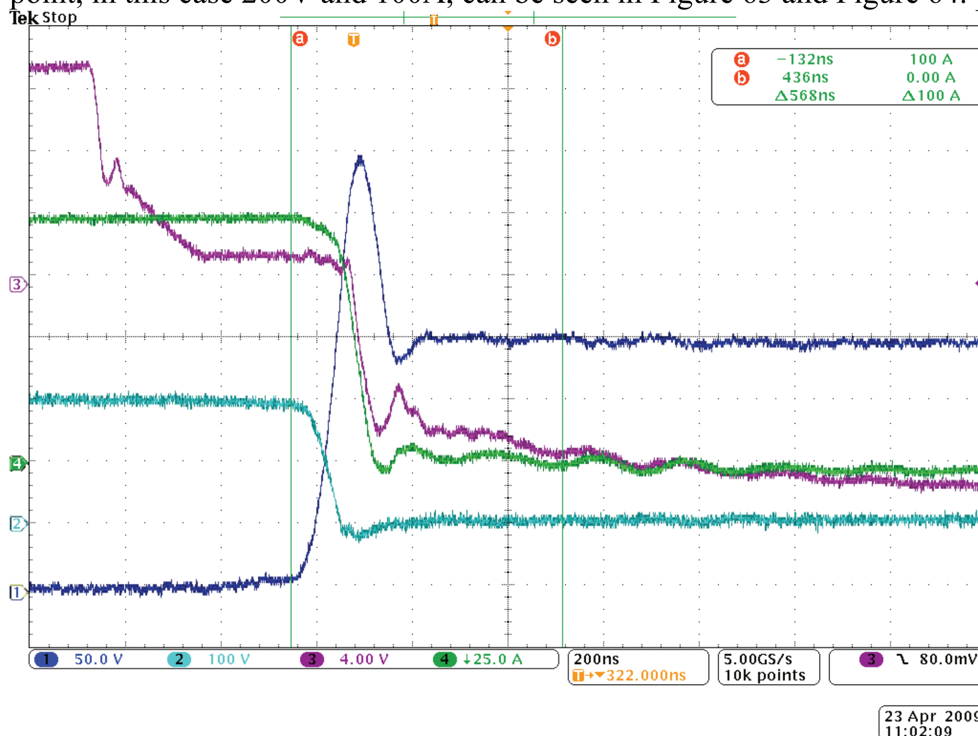


**Figure 63 Turn-off of the transistor at 200V and 100A**
**Ch1: Vce Ch2: Vak Ch3: Vge Ch4: Ice**

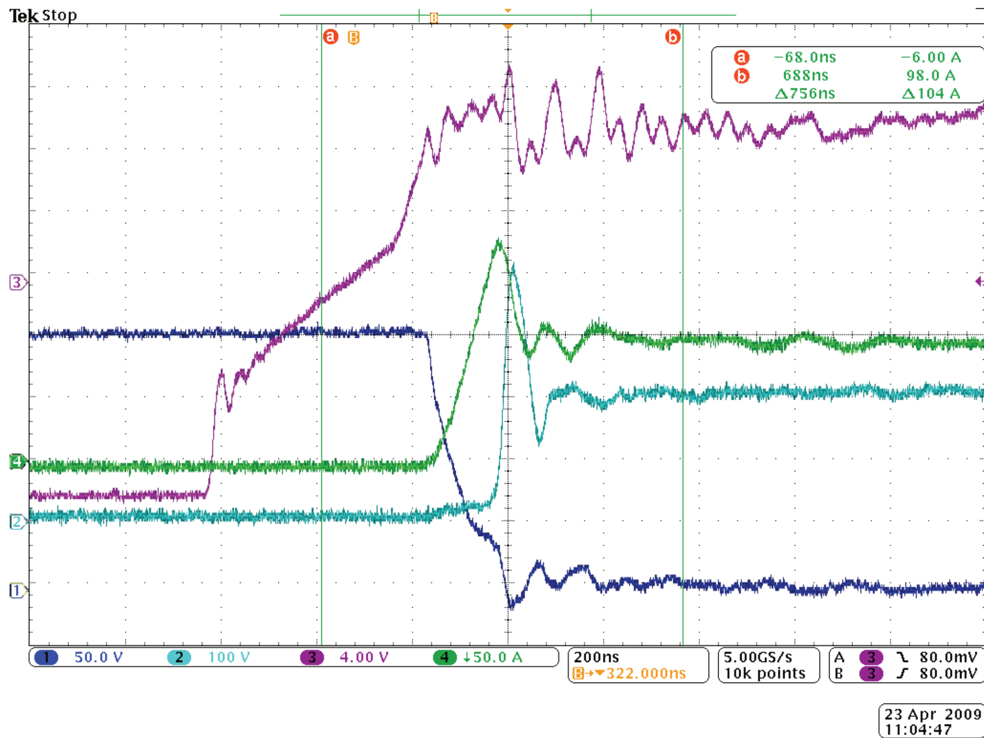


**Figure 64 Turn-on of the transistor at 200V and 100A**
**Ch1: Vce  Ch2: Vak  Ch3: Vge  Ch4: Ice**

The testing showed that the difference between the standard module in air and the open module in oil was most noticeable in the transistor current waveforms. As can be seen in Figure 65, the standard module in air is noisier and has higher peaks in the oscillations than the open module in oil. The difference is more at transistor turn-on than transistor turn-off. Some more oscillations can also be seen in the diode voltage waveforms for the open module in oil, as can be seen in Figure 66. A relatively small difference was observed between the transistor voltage waveforms, as can be seen in Figure 67. It is difficult to establish whether the differences are caused by parameter spreading between the two modules or by different operating environments.

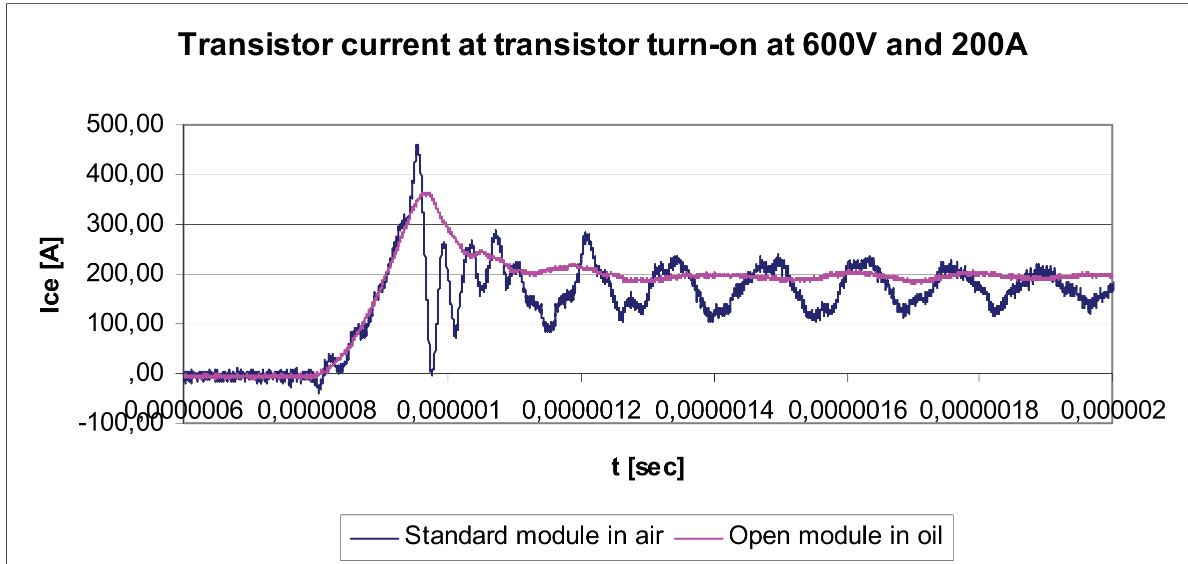


**Figure 65 Comparison of transistor current waveforms at transistor turn-on at 600V and 200A**

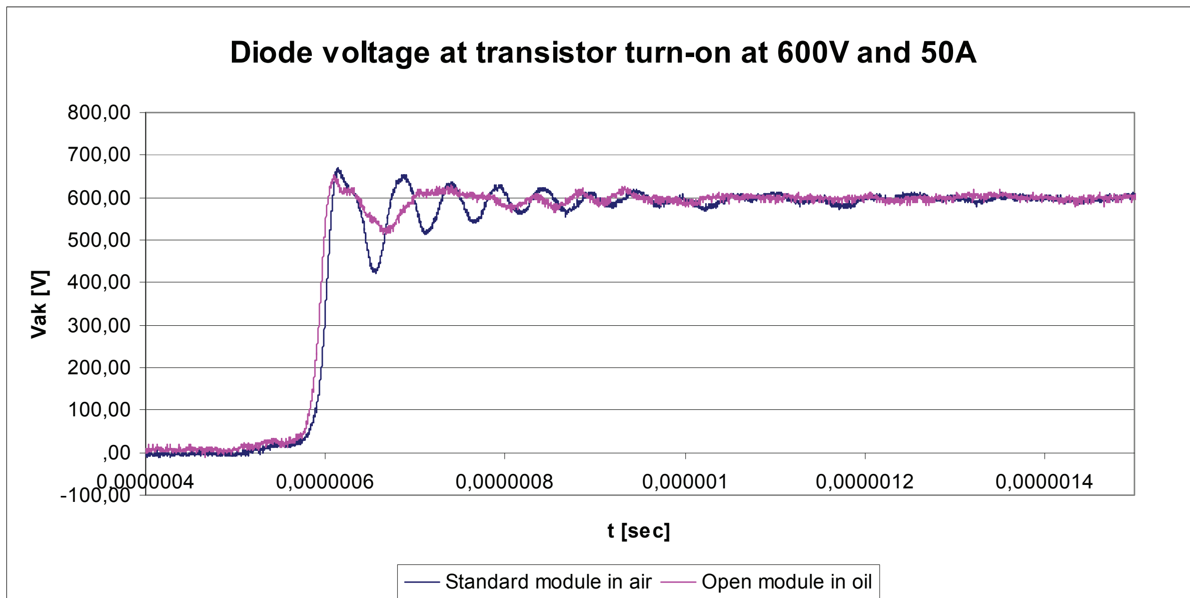


**Figure 66 Comparison of diode voltage waveforms at transistor turn-on at 600V and 50A**

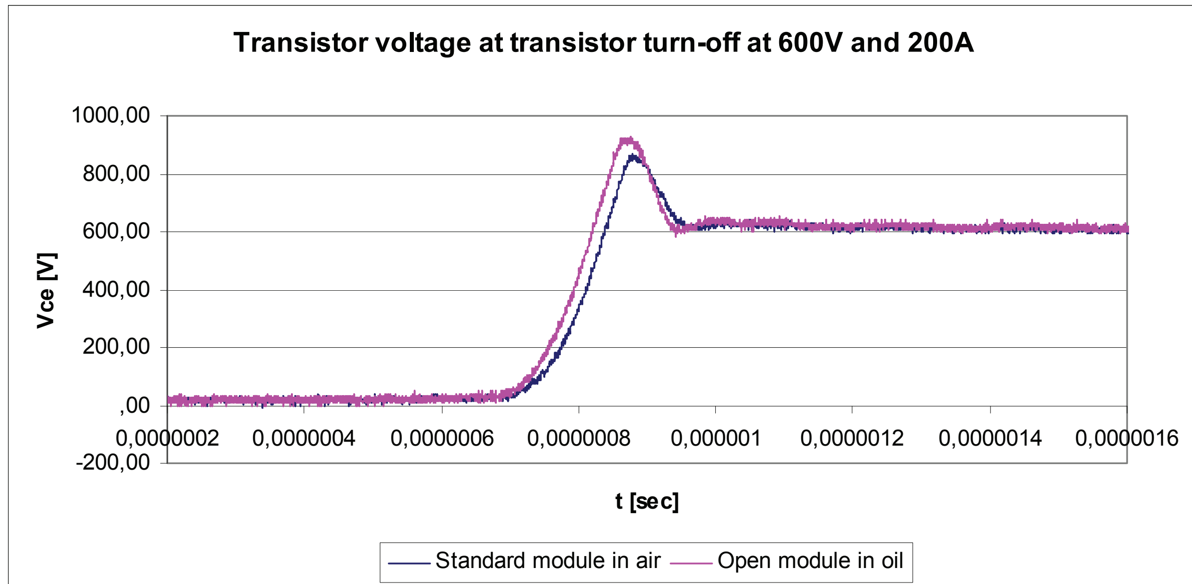


**Figure 67 Comparison of transistor voltage waveforms at transistor turn-off at 600V and 200A**

## *9.6 Continuous switching*

### 9.6.1 Description of continuous switching

Testing with continuous current is performed. The IGBT is run as a DC-DC converter with a significant load current. This is solved practically by using a current control board, described in [13]. A so called H-bridge configuration of the two bridgelegs involved is then employed. This means that one of the bridgelegs is run at a constant PWM of about 50%, giving a constant voltage at one side of the inductive load. The other bridgeleg is controlled by a PI controller on the current control board, sensing the current through the load, and comparing it with a reference given by a potmeter. This gives the possibility to adjust the voltage and current separately. The principle is shown in Figure 68.

In opposition to the double-pulse switching, it is important that the load inductor used during the continuous switching is large enough. This is in order to make the load current as constant as possible. It is also important that the power dissipation capacity of this inductor is large enough for the constant conduction of the load currents used. With background in these requirements, the air core coil used in the double-pulse switching is replaced by an iron core coil, significantly larger both in size and inductance.

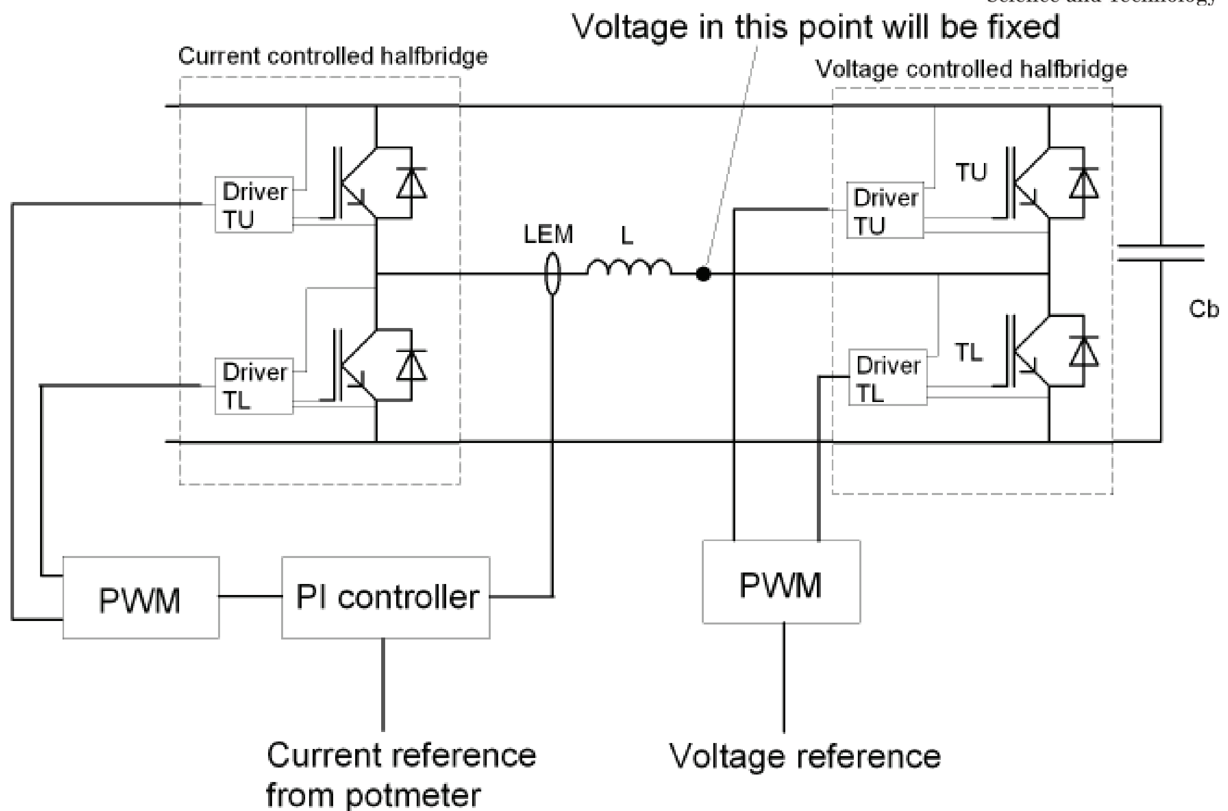


**Figure 68 Control of current and voltage in continuous testing**

The module will heat up because of losses, and possible effects of this on the switching performance can be observed. This will also be the normal mode of operation for an IGBT module, so the test is also useful in verifying the proper functioning of the module. The temperature under the module is measured with thermocouplers and a data logger. The data logger is set up to give a blocking signal to the driver interface board if the temperature becomes too high.[21]

### 9.6.2 Description of changes to test setup for the continuous switching

For the continuous switching, the load inductor is changed to a 1,2 mH, 500A iron core inductor, in order to get an approximately constant current in the load during the switching. The gate driver on the test rack is connected as gate driver B at the driver interface board of the laboratory converter. Gate driver A of the laboratory converter is controlled by an analog PI controller operating at 10 kHz. The current through the load inductor is measured by a LEM current module. The DC-link voltage is measured by a LEM voltage module. The measurements from the LEM modules are registered by the Agilent 34970A data logger, which also measures the temperature at the heatsink as described before. Further information about the continuous switching test setup can be found in [20] and [21].

The module apparently functioned properly during continuous switching, and no abnormalities were observed during the testing. The oil was heated to about 70 degrees by switching losses without any malfunction of module or test setup. It is still an important test to do, as this is the normal operating conditions of the module. A capture from the oscilloscope during continuous testing can be seen in Figure 69. It should be noted that the transistor current Ice as shown in this figure is only correct regarding the magnitude of the

current. The real Ice is a direct current, which the toroid transformer in turn translates to an alternating current when measured.

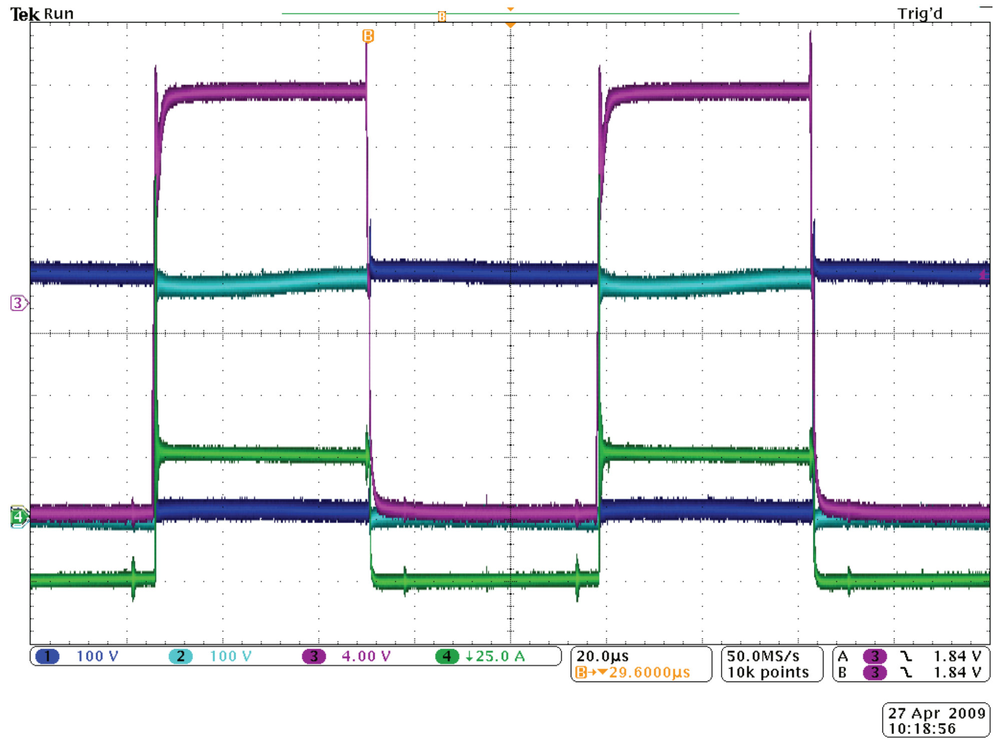


**Figure 69 Oscilloscope capture during continuous switching at 400V and 50A**
**Ch1: Vce Ch2: Vak Ch3: Vge Ch4: Ice**

# 10 BREAKDOWN VOLTAGE CONSIDERATIONS

It was decided to investigate the properties of Midel 7131 with respect to electrical strength and moisture content. Even though Midel is likely to absorb more water than mineral oil, the water saturation limit of Midel 7131 is also higher than for mineral oil. Since the relative water content is given by the ratio of the absolute water content to the water saturation limit, the relative water content for two liquids may be the same even though the absolute water content is different. The breakdown strength of an insulating liquid is dependent on the relative water content of the liquid, this is illustrated in Figure 70. The curves of interest are especially the one for Midel 7131 and the one for a mineral oil NN3000X. It can be seen that all the curves in Figure 70 has the same behaviour, although the Midel 7131 curve is a bit higher than the others.

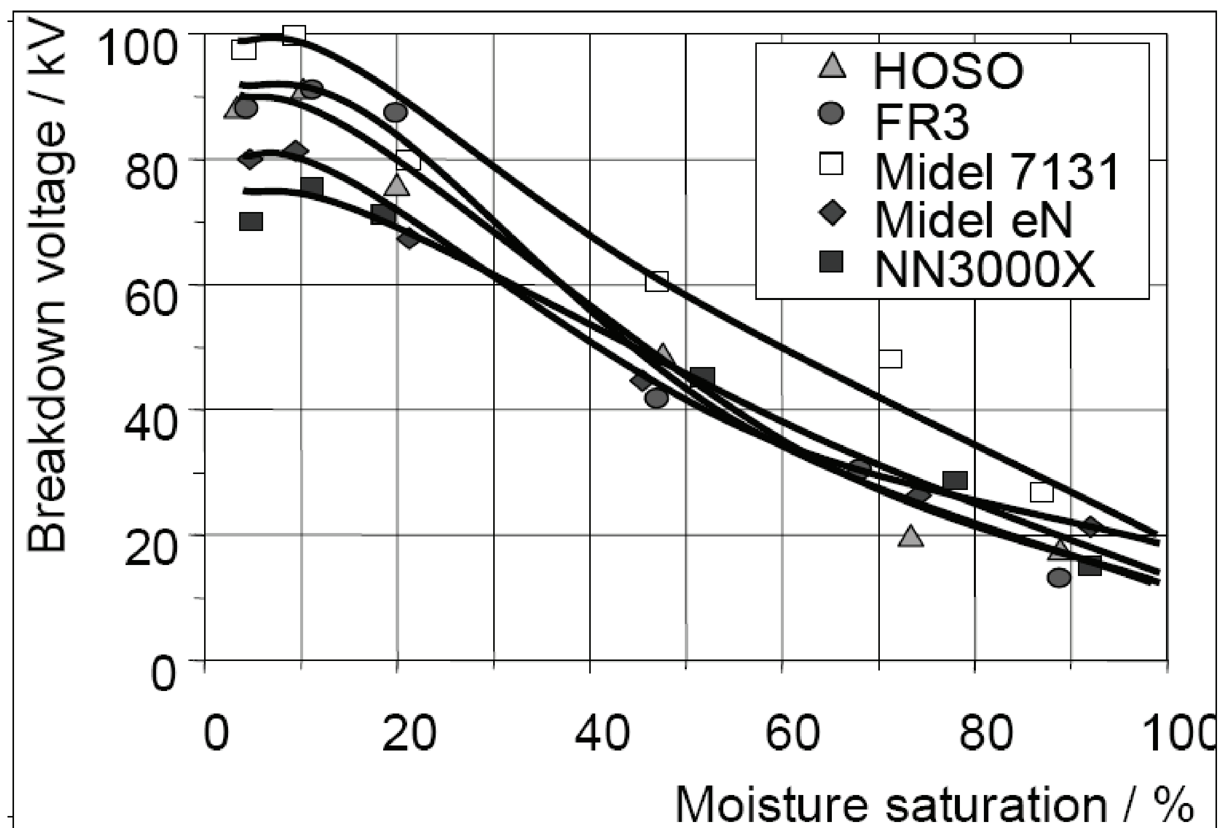


**Figure 70 Breakdown voltage with respect to moisture saturation for some dielectric liquids. NN3000X is a mineral oil, the rest are natural oils [43]**

It is also possible to draw curves showing breakdown voltage with respect to water content in parts per million. An example of such a curve can be seen in Figure 71. From this figure it can be seen than Midel 7131 performs much better than mineral oil if measured by absolute water content.

It should be noted that the notion of breakdown voltage used in Figure 70 and Figure 71 refers to specific test conditions. This usually means measuring the breakdown voltage for a given voltage waveform between standardized electrodes, i.e plane-plane gap at a distance of 2,5 mm. Alltough the test conditions in Figure 70 and Figure 71 may not be the same, the purpose here is to show the difference between the two representation methods.

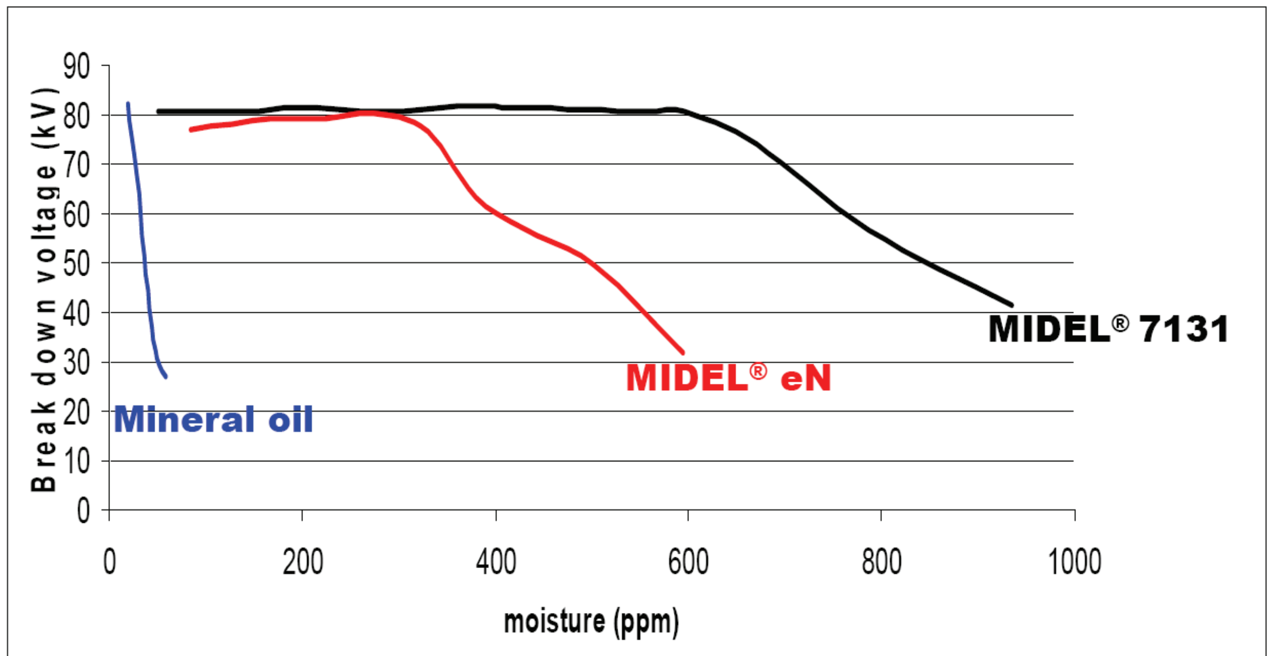


**Figure 71 Breakdown voltage with respect to water content in parts per million at 20 degrees Celsius. Midel eN is an organic ester not investigated in this report [44]**

As stated before, the water saturation limit of Midel 7131 is significantly higher than for a mineral oil. A comparison between Midel 7131 and the mineral oil Shell Diala D with respect to water saturation limit has been reported in [45]. Also mixtures of the two oils were investigated. The significant difference in water saturation limit for the two oils can be seen in Table 25.

**Table 25 Water saturation limits for a mineral oil and Midel 7131 at different temperatures [45]**

| | Water saturation limit in parts per million (ppm) | | | | |
|---|---|---|---|---|---|
| | 20°C | 23°C | 60°C | 88°C | 100°C |
| Mineral oil Shell Diala D | 45 | 51 | 210 | 510 | 716 |
| Synthetic ester Midel 7131 | 2700 | 2829 | 4675 | 6386 | 7200 |

Investigations performed in [42] that consider operation in an open transformer system over extended periods of time suggests that the Midel 7131 will absorb up to 500 ppm of water. Specifications for new Midel 7131, as given in the datasheet, give a maximum water content of 50 ppm. Midel 7131 will be within specifications for water content up to 400 ppm but still maintaining a high breakdown voltage for water content exceeding 550 ppm.[22].

The breakdown voltage as given in Figure 70 and Figure 71 is with respect to specified testing conditions. This means that it is difficult to calculate the water content in the Midel 7131 that

should give breakdown when the open IGBT module is operating in the Midel. This is because the breakdown phenomena are dependent on a number of factors that is not trivial to investigate. Geometric considerations, voltage waveform and contaminations will affect the real breakdown voltage, and will also make it very difficult to calculate a water content that should give breakdown for a given voltage in the real test setup.

A better approach may be to establish relatively unideal operating conditions with respect to water content, and then observe if breakdown phenomena occurs. This would also be useful for the project in a greater sense, as a parallel project involving electrical stress and field calculations on the IXYS module could benefit from these observations. A relative water content of for example 90% at 20 degrees Celsius could constitute a starting point for the testing. More water could then be added later to give a relative water content of for example 100% at 60 degrees Celsius. This case would give condensation of water when the oil is cooled from 60 degrees Celsius and the condensed water may impact the breakdown properties of oil.

The volume of oil in the container has been measured to 7,61 liters. The water content of this oil was measured by the Karl Fischer method to be 466,7 ppm, this is actually over the limit at 400 ppm for the Midel to keep the specification. The reason for the high water content is that the oil has been stored in the laboratory exposed to air.

If a relative water content of 90% at 20 degrees Celsius is desired, it can be calculated as in the following, using the saturation limit from Table 25. The density of Midel 7131 is 0,97 $kg/dm^3$ and the density of water is taken as 1 $kg/dm^3$.

Calculation of the mass of Midel 7131

$$m_{midel} = V_{midel} \cdot \rho_{midel} = 7{,}61 dm^3 \cdot 0{,}97 \frac{kg}{dm^3} = 7{,}38 kg \tag{28}$$

Calculation of how much water it is necessary to add to obtain 90% relative water content

$$2700 ppm \cdot 0{,}90 - 466{,}7 ppm = 1963{,}3 ppm \tag{29}$$

Calculation of mass of water taking into account water the desired relative water content

$$m_{water} = m_{midel} \cdot \frac{1963{,}3}{10^6} = 7{,}38 \cdot \frac{1963{,}3}{10^6} = 0{,}0145 kg \tag{30}$$

Calculation of necessary volume of added water

$$V_{water} = \frac{m_{water}}{\rho_{water}} = \frac{0{,}0145 kg}{1 \frac{kg}{dm^3}} = 0{,}0145 dm^3 = 14{,}5 mL \tag{31}$$

The necessary water is added as distilled water from an Arium 611 UV which gives a product water quality of 18,2 MΩ*cm. The Midel/water mix should then be stirred thoroughly for several hours until the water has been dissolved.

Dissolving the water into the Midel showed to be challenging. After thorough stirring for several days, the relative water content of the Midel/water mixture was measured with a Vaisala MI70 Moisture Meter for Oil. In addition, the relative moisture was measured after the first electrical test had been finished. At this point the Midel/water mixture had been exposed to air in the laboratory for approximately 24 hours. The results can be seen in Table 26. As can be seen, the relative water content 24 hours later is a bit lower than before. It is however difficult to say if the decrease in relative water content is mostly caused by evaporation or by the increased temperature. Since the oil will have higher maximum water content for a higher temperature, the relative water content will go down if the temperature increases and the absolute water content remains the same.

**Table 26 Measurements of relative water content**

| Time of measurement | Relative water content [%] | Temperature [degrees Celsius] |
|---|---|---|
| Immediately after end of stirring | 78 | 19,0 |
| Approximately 24 hours later | 74 | 22,7 |

The IXYS test setup was lowered into the Midel/water mixture and double-pulse switching at increasing voltages was performed. No partial discharge or other breakdown phenomena were observed, and the IGBT module seemed to be operating flawlessly. However, when comparing the switching waveforms before and after adding of water, some differences were observed. As can be seen in Figure 72, the transistor voltage overshoot at transistor turn-off was larger before adding of water. A difference in the transistor current was also observed after adding of water. As can be seen in Figure 73, the transistor current overshoot at transistor turn-on was larger after adding of water. The shape of the overshoot is also somewhat different. Other waveforms that were compared before and after adding of water were seen to be relatively equal. The author has not been able to find an explanation for these differences in the waveforms before and after adding of water.

The DC-link voltage of the laboratory converter is limited to approximately 630V, which was not sufficient to induce breakdown phenomena under these testing conditions. An additional test was done, where 600V DC-link voltage was applied for two hours without switching. This was in order to try to produce polarization effects in the oil. The switching was so turned on at 600V and 200A after two hours. No phenomena were observed during this test.

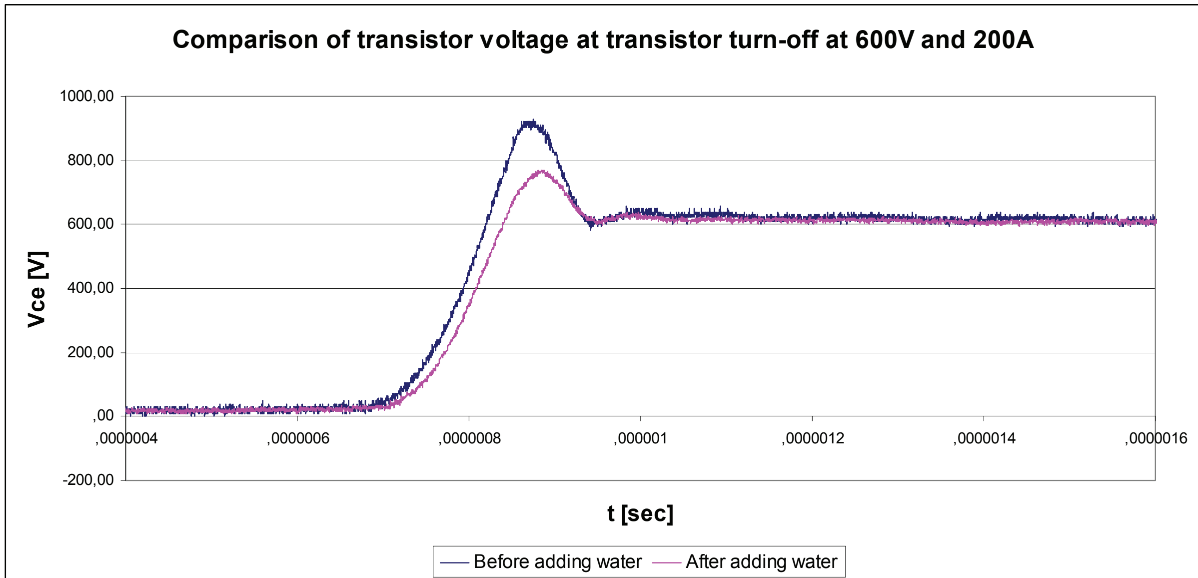


**Figure 72 Comparison of transistor voltage before and after adding of water**

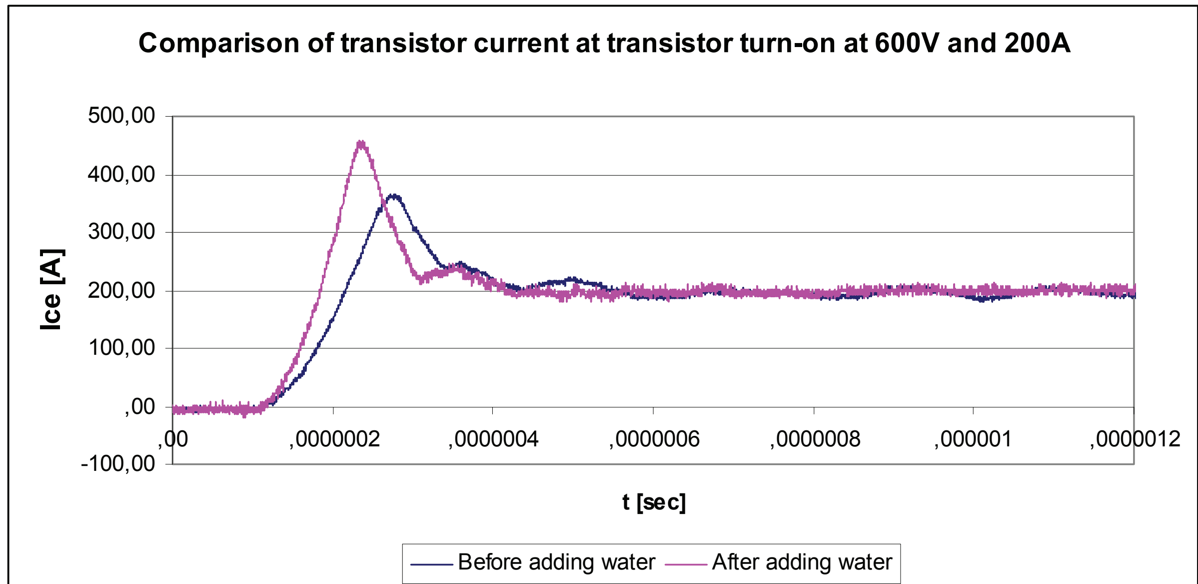


**Figure 73 Comparison of transistor current before and after adding of water**

# 11 DISCUSSION

Testing showed that the thermal resistance from chip to ambient went down when the module was filled with Midel compared to when filled with air. Testing also showed that the thermal capacitance as seen from the chip went up when the module was filled with Midel. This was as expected. Estimation of heat flow in the module showed that there is less heat going down through the substrate when the module is filled with Midel. This estimation should be regarded as qualitative, as it does not take into account the three-dimensional heat flow in the module. It is important to place the chip temperature sensor as close as possible to chip. Placement on top of the chip is however not possible due to the bonding wires. The chip temperature measurement is therefore likely to be slightly lower than the real junction temperature.

Care has to be taken when running the module in active mode of operation without heatsink, as relatively low power dissipation levels, i.e. 10-15W can lead to relatively high temperatures.

When developing the thermal equivalent networks by the method used in this project, the accuracy of the model will be determined by the development itself. If one takes the time to develop an increasing number of time constant expressions, the model will be increasingly accurate. One may however, experience during Foster to Cauer equivalent network transformation, that the number of RC-cells goes down. This is due to the Cauer network transfer function having a different dependency on the RC-cells than the Foster network transfer function. Even with a lower number of RC-cells, the transfer function is thus not less accurate for the Cauer network, if the transformation is performed correctly.

A two dimensional model was constructed in COMSOL Multiphysics. The model only considers one chip on top of the substrate layers. This means that comparison with measurements done on the IGBT module becomes very difficult, as the whole module represents a much larger thermal network than the chip. Almost all the results from these simulations should therefore be treated qualitatively. Part of the reason for doing these COMSOL simulations was indeed for investigating the possibilities in COMSOL Multiphysics, also for possible future use. To be able to compare simulation results with laboratory measurements a larger and more detailed two or three dimensional model has to be constructed, but this was beyond the scope of this project.

For the simulation with stationary cooling medium, a relatively good agreement between simulation and measurement was achieved when the cooling medium was air. The same agreement was not possible to obtain when the cooling medium was Midel.

As is described in the chapter on thermocamera measurements, the thermocamera relies on the emissivity of materials for measuring the temperature. This means that blank surfaces which are not covered in Midel will seem to be at a much lower temperature in the thermocamera than they really are. In addition, when the chip temperature increases, the difference between the maximum and minimum temperatures of the module as seen by the thermocamera increases. This in turn means that the scale has to have larger increments to accommodate the maximum and minimum values, giving less accuracy.

As noted in the chapter on inductance considerations, it is possible to calculate the stray inductance of a two busbar configuration using analytical formulas found in literature. However, these formulas assume a uniform current distribution, thereby neglecting proximity and skin effects. When dealing with high frequency signals, the inductance calculation will thus be inaccurate. Modeling with a finite elements program seems to be a relatively simple

way of simulating the stray inductance taking into account frequency. As expansion of the initial structure into more complex geometries is also relatively easily performed, the finite element approach seems to be superior.

The results from the passive pressure testing of an IXYS module showed that the reference module was actually noisier than the module which had been subjected to pressure. Although it is not possible to say for certain, a reason may be the existence of small differences from one module to another, including parameter spreading. The reference module is the same module that was used during the testing in the autumn project. It should also be noted that the module which had been pressurized was not subjected to long term testing, i.e. switching significant power for extended periods of time.

Double-pulse switching of the open module at reduced voltage immediately before and after immersion in oil showed little difference between the waveforms in the two cases. Immersion in oil therefore does not seem to influence the switching behaviour at reduced voltage. Comparison at higher voltages is not possible due to the reduced maximum allowable voltage when the open module is run in air.

For comparing at higher voltages, the test results from the double-pulse switching of a standard module in air have to be used. Part of any difference between the switching waveforms therefore may be caused by parameter spreading in the modules. The testing showed that the difference between the standard module in air and the open module in oil was most noticeable in the transistor current waveforms. Comparison of the transistor current waveform showed that the standard module in air was noisier and had higher peaks in the oscillations than the open module in oil. It is difficult to estimate how much of the difference is caused by parameter spreading and how much is caused by the difference in operating conditions.

When mixing the water into the Midel, it is important to stir thoroughly for relatively long periods of time, i.e. 24 hours. Even then, it was observed that it is difficult to obtain high values of relative water content. This was experienced even when the oil was heated to 50 degrees Celsius. One may also experience the forming of water drops in the oil, but these will tend to fall to the bottom of the container, if the oil is left still. It is presumed that the relative water content of the Midel will fall when it is exposed to air in the laboratory, since the relative water content of the air is likely to be less than for the oil. Some differences between the transistor current and voltage waveforms at double-pulse switching before and after adding of water were seen. An explanation for these differences has not been found during this project.

# 12 CONCLUSIONS

Thermal testing of the IGBT module in the active mode of operation was performed. As expected, the module without heatsink has a very low heat dissipation capability, with a dissipated power in the range of 10W giving chip temperatures in excess of 80 degrees Celsius. When Midel 7131 is added inside the open module, the time to heat up the module becomes significantly longer. This is to be expected due to the additional thermal capacitance of the Midel. The stationary chip temperature difference between the two cases is however relatively small at 2,9 degrees Celsius. Comparisons of the different temperature measurements for the two cases indicated that more of the heat is transported upwards from the chip when the cooling medium is Midel.

Shaking the module during testing in the active mode of operation showed better transient thermal behaviour, as all the temperature measurements had a lower rate of increase during shaking. Shaking of the module made a rough estimation of the contact resistance from chip to oil possible, which was estimated to be 1,3 K/W.

A mathematical description of the transient chip temperature behaviour was found using transient temperature measurements. The mathematical description was used to build a Foster thermal equivalent network. The Foster network was transformed into a Cauer thermal equivalent network using network synthesis. The thermal equivalent network was then simulated in a circuit simulator. The measured, mathematical and simulated transients showed good agreement.

A simple model of the IXYS IGBT was constructed in COMSOL Multiphysics by considering only the chip and substrate layers beneath the chip. The simple model showed that Midel 7131 had a better ability to transport heat away from the chip compared to air. This is to be expected since Midel 7131 has a higher thermal conductivity than air. It was also seen that Midel 7131 gave a slower temperature increase at the chip surface than air. This is to be expected, because Midel 7131 has a higher thermal capacity than air. Steady state temperatures when the model was simulated with still air above the chip showed good correspondence with measured temperatures. It should however be noted that the point of measurement in the model has a great influence on the temperature reading, so this has to be selected with care.

Thermocamera measurements showed significant temperature gradients at the top of the substrate during testing. This was to be expected due to only one of the IGBT's of the module being heated. When using a heatsink, it was seen that the heatsink attains a quite uniform temperature. The temperature in the substrate away from the chips will attain approximately the temperature of the heatsink. The temperature will thus drop of more quickly when moving away from the chip area when using a heatsink.

A brief literature study regarding the stray inductance conditions for the bus bars in the test setup was performed. A sample inductance calculation by finite elements method was performed in COMSOL Multiphysics for two different busbar configurations. As was expected, the configuration with two bus bars over each other was significantly better than the configuration with two bus bars side by side. In addition to giving a higher accuracy by taking into account high-frequency effects, the finite element method was not any more time-consuming than the analytical methods that were looked at in this report. Inductance calculation by finite element method is therefore suggested for future work.

Components relevant to the test setup which had been subjected to passive pressure testing at 300 bars were investigated. Even though some of the components had been affected

mechanically by the pressure, all components functioned properly during the electrical testing. Comparison with reference tests done on a non-pressurized module actually showed that the pressure-tested module was less noisy than the reference module. This may however be attributed to parameter spreading between the two modules.

Double-pulse switching of an open module in oil was performed. Waveform comparison with a test performed immediately before immersion in oil showed no significant differences before and after immersion. Comparison with the standard module that was tested in air during the autumn showed the transistor current waveform to be less noisy for the open module in oil. The waveforms when switching the open module in oil seemed to be according to theoretical switching waveforms.

Water was added to the Midel, giving a relative water content of the Midel during testing of approximately 78%. When double-pulse switching the IXYS module in the Midel/water mixture at 600V and 200A no breakdown phenomena were observed. The DC-link voltage of the laboratory converter is limited to approximately 630V, no phenomena were observed when double-pulse switching at this voltage either. The added water did not seem to affect the general operation of the IXYS module, but some differences were seen in the transistor voltage and current waveforms.

# REFERENCES

[1] Kristoffersen, A., *Sub Sea Power Electronics*, Master thesis. The Norwegian University of Science and Technology, 2007

[2] Mohan, N., Undeland, T., M., Robbins, W., P., *Power Electronics, Converters, Applications and Design,* Media enhanced 3rd edition. John Wiley & Sons, INC., 2003.

[3] Kolstad, H., Ljøkelsøy, K., *20 kW IGBT omformer. Beskrivelse 2. utgave.* Open worknote SINTEF, 2001

[4] Rogne, T., Ljøkelsøy, K., *Gatedriver SMD2. Sammendragsrapport funksjonsbeskrivelse, kretsskjema, komponentliste, spesifikasjoner og testprosedyre.* Open worknote SINTEF 2001

[5] Holzschuh, J. E., *Pressure Tolerant Electronics,* Naval Undersea Center, San Diego, California, 1970

[6] Sutton, J.L, *Pressure Tolerant Electronic Systems,* Naval Ocean Systems Center, San Diego, California, 1979

[7] Nordanger, K., *AN 07.12.25 Simulations of subsea vessel cooling using COMSOL Multiphysics,* SINTEF Energy Research, 2007

[8] Nordanger, K., *AN 07.12.136 Detailed thermal modelling of IGBT test object in oil filled chamber,* SINTEF Energy Research, 2007

[9] Aspmo, B., Rogne, T., *AN 87.40.12 Feiltolerante Undervanns Kraftelektronikksystemer,* EFI, 1987.

[10] Barnes, H.E., Gennari,J.J, *A Review of Pressure-Tolerant Electronics (PTE),* Naval Research Laboratory, 1976

[11] Marquardt, R.A., *,Five-Year Life Test Data on Pressure (10 000 lbf/in$^2$) Tolerant Electronic Components,* IEEE Transactions on Components, Hybrids, and Manufacturing Technology, Vol. CHMT-1, NO.4, December 1978.

[12] Khanna V. K., *The Insulated Gate Bipolar Transistor IGBT Theory and Design*,, IEEE Press, John Wiley & Sons INC., 2003

[13] Ljøkelsøy, K., *AN 98.13.44 Analog strømregulatorkort v1.0,* Open Worknote SINTEF, 1998.

[14] Oh, K.S, *IGBT Basics 1, Application Note 9016*, Fairchild Semiconductor, February 2001

[15] Pittini, R., *AN 08.12.84 Reinforcing the "EFI-driver"for operation in pressurized liquid environment,* SINTEF Energy Research, 2008

[16] Dodge J, Hess J, *IGBT Tutorial Application Note APT0201 Rev. B*, Advanced Power Technology, July 2002

[17] Ljøkelsøy, K., Lund, R., *AN 00.12.49 Driver interface board, v 4.0 – Documentation 2. edition,* Open Worknote SINTEF, 2000

[18] IXYS, *IGBT module datasheet MII400-12E4,* IXYS, 2007

[19] Ljøkelsøy, K., Holt, Ø., *Igangkjøring av Tyco IGBT modul for trykktesting. Laboratorieprotokoll*, Worknote SINTEF, July 2008

[20] Holt, Ø., *Introductory testing of IXYS IGBT module for pressurization. Laboratory protocol.*, Project Memo SINTEF, 2008

[21] Holt, Ø., *Pressure Tolerant Power Electronics.*, Specialization Project NTNU, 2008

[22] M&I Materials Ltd*., Midel 7131*, Technical datasheet, September 2007

[23] Incropera, F., DeWitt, D., Bergman, L., Lavine, A., *Introduction to Heat Transfer, Fifth Edition*, John Wiley & Sons, 2007

[24] M&I Materials Ltd*., Midel 7131*, Technical datasheet, September 2007

[25] Skibinski, G., Divan, D., Bergman, *Design Methodology & Modeling of Low Inductance Planar Bus Structures*, The European Power Electronics Association, 1993

[26] Grover F., *Inductance calculations: working formulas and tables*, New York, 1946

[27] Qiu, Z., Zhang, H., Chen, G., *Study and Design of Noninductive Bus bar for high power switching converter*, Power Electronics and Motion Control Conference, 2006

[28] Caponet, M., Profumo, F., De Doncker, R., Tenconi, A., *Low Stray Inductance Bus Bar Design and Construction for Good EMC Performance in Power Electronic Circuits,* IEEE Transactions on Power Electronics, 2002

[29] Giacoletti, L., *Electronics Designer's Handbook, 2nd ed.,* McGraw-Hill, New York, 1977.

[30] Nilssen, R., *Electromagnetics in Power Engineering,* Compendium, Norwegian University of Science and Technology, 2007

[31] IXYS*, What is DCB, DCB Data,* IXYS, 2004

[32] Pittini, R., *Provocative pressure testing of power electronics components in 300 bar oil environment,* Project Memo SINTEF, 2009

[33] Bagnoli, P., Casarosa, C., Ciampi, M., Dallago, E., *Thermal Resistance Analysis by Induced Transient (TRAIT) Method for Power Electronic Devices Thermal Characterization – Part I: Fundamentals and Theory,* IEEE Transactions on Power Electronics, Vol.13, No.6, November 1998

[34] Székely, V., *A new evaluation method of thermal transient measurement results,* Microelectronics Journal 28, 1997

[35] Carmona, M. Marco, S., Palacín, J., Samitier, J., *A Time-Domain Method for the Analysis of Thermal Impedance Response Preserving the Convolution Form,* IEEE Transactions on Components and Packaging Technology, Vol.22, No.2, June 1999

[36] Luo, Z., Ahn, H., El Nokali, M., *A thermal Model for Insulated Gate Bipolar Transistor Module,* IEEE Transactions on Power Electronics, Vol.19, No.4, July 2004

[37] Gerstenmayer, Y., Kiffe, W.,Wachutka, G., *Combination of Thermal Subsystems Modeled by Rapid Circuit Transformation,* THERMINIC, Budapest, September 2007

[38] Shammas, N., Rodriguez, M., Masana, F.., *A simple method for evaluating the transient thermal response of semiconductor devices,* Microelectronics Reliability 42, 2002

[39] Ciappa, M., Fichtner, W., Kojima, T., Yamada, Y., Nishibe, Y.., *Extraction of Accurate Thermal Compact Models for Fast Electro-Thermal Simulation of IGBT Modules in Hybrid Electric Vehicles,* Microelectronics Reliability 45, 2005

[40] Weinberg, L., *Network Analysis and Synthesis,* McGraw-Hill Electrical and Electronic Engineering Series, 1962

[41] Borsi, H., Gockenbach, E., *Properties of Ester Liquid Midel 7131 as an Alternative Liquid to Mineral Oil for Transformers,* IEEE International Conference on Dielectric Liquids, 2005

[42] Wruss, G. *,Enviromentally-friendly Distribution Transformers,* VA Tech ELIN Transformatoren

[43] Koch, M., Tenbohlen, S. *,A Systematic Aging Test of Ester Liquids ,* Universität Stuttgart, Omicron, Euro TechCon 2008

[44] Martin, R. *,The Role of Esters in Improving Reliability and Safety in Transformers ,* M&I Materials, 2006

[45] Arakelian, V.G., Fofana, I., *Water in Oil-Filled High-Voltage Equipment Part I: States Solubility, and Equilibrium in Insulating Materials,* Electrical Insulation Magazine, IEEE, 2007

# APPENDIX A: IXYS MII400-12E4 [18]

## IGBT Module

phaseleg and chopper topolgies
with optional temperature sensor

Preliminary Data

$I_{C25}$ = 420 A
$V_{CES}$ = 1200 V
$V_{CE(sat)\ typ.}$ = 2.2 V

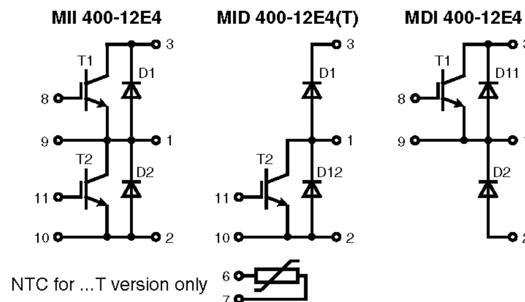

| IGBTs T1 - T2 | | | |
|---|---|---|---|
| **Symbol** | **Conditions** | **Maximum Ratings** | |
| $V_{CES}$ | $T_{VJ}$ = 25°C to 125°C | 1200 | V |
| $V_{GES}$ | | ± 20 | V |
| $I_{C25}$<br>$I_{C80}$ | $T_C$ = 25°C<br>$T_C$ = 80°C | 420<br>300 | A<br>A |
| $I_{CM}$<br>$V_{CEK}$ | $V_{GE}$ = ±15 V; $R_G$ = 4.7 Ω; $T_{VJ}$ = 125°C<br>**RBSOA** Clamped inductive load; L = 100 µH | 450<br>$V_{CES}$ | A |
| $t_{SC}$<br>**(SCSOA)** | $V_{CE}$ = 900 V; $V_{GE}$ = ±15 V; $R_G$ = 4.7 Ω<br>$T_{VJ}$ = 125°C; non-repetitive | 10 | µs |
| $P_{tot}$ | $T_C$ = 25°C | 1700 | W |

| **Symbol** | **Conditions** (Characteristic Values; $T_{VJ}$ = 25°C, unless otherwise specified) | | **min.** | **typ.** | **max.** | |
|---|---|---|---|---|---|---|
| $V_{CE(sat)}$ | $I_C$ = 300 A; $V_{GE}$ = 15 V; | $T_{VJ}$ = 25°C<br>$T_{VJ}$ = 125°C | | 2.2<br>2.6 | 2.8 | V<br>V |
| $V_{GE(th)}$ | $I_C$ = 10 mA; $V_{GE}$ = $V_{CE}$ | | 4.5 | | 6.5 | V |
| $I_{CES}$ | $V_{CE}$ = $V_{CES}$; $V_{GE}$ = 0 V; | $T_{VJ}$ = 25°C<br>$T_{VJ}$ = 125°C | | 0.8<br>3.5 | 3.3 | mA<br>mA |
| $I_{GES}$ | $V_{CE}$ = 0 V; $V_{GE}$ = ± 20 V | | | | 600 | nA |
| $t_{d(on)}$<br>$t_r$<br>$t_{d(off)}$<br>$t_f$<br>$E_{on}$<br>$E_{off}$ | Inductive load, $T_{VJ}$ = 125°C<br>$V_{CE}$ = 600 V; $I_C$ = 300 A<br>$V_{GE}$ = ±15 V; $R_G$ = 4.7 Ω | | | 170<br>60<br>680<br>50<br>44<br>30 | | ns<br>ns<br>ns<br>ns<br>mJ<br>mJ |
| $C_{ies}$<br>$Q_{Gon}$ | $V_{CE}$ = 25 V; $V_{GE}$ = 0 V; f = 1 MHz<br>$V_{CE}$ = 600 V; $V_{GE}$ = 15 V; $I_C$ = 300 A | | | 17<br>1.74 | | nF<br>µC |
| $R_{thJC}$<br>$R_{thJH}$ | (per IGBT)<br>with heatsink compound | | | <br>0.15 | 0.08 | K/W<br>K/W |

**Features**

- NPT[3] IGBT
  - low saturation voltage
  - positive temperature coefficient
  - fast switching
  - short tail current for optimized performance in resonant circuits
- HiPerFRED™ diodes
  - fast and soft reverse recovery
  - low operating forward voltage
  - low leakage current
- NTC sensor for measurement of case temperature
- Package
  - low inductive current path
  - screw connection to high current main terminals
  - use of non interchangeable connectors for auxiliary terminals possible
  - Kelvin emitter terminal for easy drive
  - isolated ceramic base plate

**Applications**

- drives
  - AC
  - DC
- power supplies
  - rectifiers with power factor correction and recuperation capability
  - UPS

IXYS reserves the right to change limits, test conditions and dimensions.

20070725a

© 2007 IXYS All rights reserved

IXYS **MII400-12E4** **MID400-12E4(T)** **MDI400-12E4**

| Free wheeling diodes D1 - D2 | | | | | | |
|---|---|---|---|---|---|---|
| **Symbol** | **Conditions** | | | | Maximum Ratings | |
| $I_{F25}$ | $T_C$ = 25°C | | | | 450 | A |
| $I_{F80}$ | $T_C$ = 80°C | | | | 290 | A |
| **Symbol** | **Conditions** | | **Characteristic Values** | | | |
| | | | **min.** | **typ.** | **max.** | |
| $V_F$ | $I_F$ = 300 A; $V_{GE}$ = 0 V; | $T_{VJ}$ = 25°C | | 2.3 | 2.7 | V |
| | | $T_{VJ}$ = 125°C | | 1.7 | | V |
| $I_{RM}$ | $I_F$ = 225 A; $di_F/dt$ = -2000 A/µs; | | | 200 | | A |
| $t_{rr}$ | $V_R$ = 600 V; $V_{GE}$ = 0 V; | $T_{VJ}$ = 125°C | | 220 | | ns |
| $R_{thJC}$ | (per IGBT) | | | | 0.15 | K/W |
| $R_{thJH}$ | with heatsink compound | | | 0.3 | | K/W |

| Chopper anti parallel diodes D11 - D12 | | | | | | |
|---|---|---|---|---|---|---|
| **Symbol** | **Conditions** | | | | Maximum Ratings | |
| $I_{F25}$ | $T_C$ = 25°C | | | | 150 | A |
| $I_{F80}$ | $T_C$ = 80°C | | | | 95 | A |
| **Symbol** | **Conditions** | | **Characteristic Values** | | | |
| | | | **min.** | **typ.** | **max.** | |
| $V_F$ | $I_F$ = 100 A; $V_{GE}$ = 0 V; | $T_{VJ}$ = 25°C | | 2.3 | 2.7 | V |
| | | $T_{VJ}$ = 125°C | | 1.7 | | V |
| $I_{RM}$ | $I_F$ = 75 A; $di_F/dt$ = -750 A/µs; | | | 80 | | A |
| $t_{rr}$ | $V_R$ = 600 V; $V_{GE}$ = 0 V; | $T_{VJ}$ = 125°C | | 220 | | ns |
| $R_{thJC}$ | (per IGBT) | | | | 0.45 | K/W |
| $R_{thJH}$ | with heatsink compound | | | 0.9 | | K/W |

| Temperature Sensor NTC (...T version only) | | | | | |
|---|---|---|---|---|---|
| **Symbol** | **Conditions** | **Characteristic Values** | | | |
| | | **min.** | **typ.** | **max.** | |
| $R_{25}$ | T = 25°C $\left\{R(T) = R_{25} \cdot e^{B_{25/100}\left(\frac{1}{T} - \frac{1}{298K}\right)}\right\}$ | | 2200 | | kΩ |
| $B_{25/100}$ | | | 3560 | | K |

| Module | | | | | | |
|---|---|---|---|---|---|---|
| **Symbol** | **Conditions** | | | | **Maximum Ratings** | |
| $T_{VJ}$ | operating | | | | -40...+150 | °C |
| $T_{stg}$ | | | | | -40...+125 | °C |
| $V_{ISO}$ | $I_{ISOL} \leq$ 1 mA; 50/60 Hz | | | | 4000 | V~ |
| $M_d$ | Mounting torque | (module, M6) | | | 2.25 - 2.75 | Nm |
| | | (terminal, M6) | | | 4.5 - 5.5 | Nm |
| **Symbol** | **Conditions** | | **Characteristic Values** | | | |
| | | | **min.** | **typ.** | **max.** | |
| $d_S$ | Creepage distance on surface | | 2 | | | mm |
| $d_A$ | Strike distance in air | | 2 | | | mm |
| **Weight** | | | | 250 | | g |

**Equivalent Circuits for Simulation**

**Conduction**

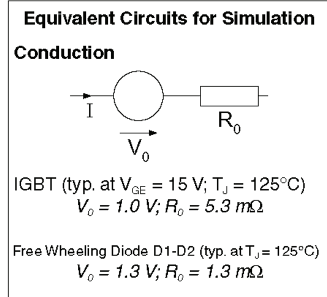


IGBT (typ. at $V_{GE}$ = 15 V; $T_J$ = 125°C)
$V_0$ = 1.0 V; $R_0$ = 5.3 mΩ

Free Wheeling Diode D1-D2 (typ. at $T_J$ = 125°C)
$V_0$ = 1.3 V; $R_0$ = 1.3 mΩ

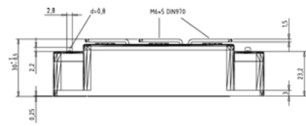

**Dimensions in mm (1 mm = 0.0394")**

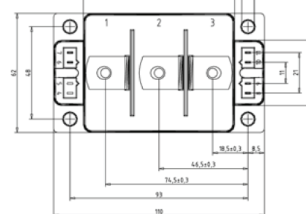

**Optional accessories for modules**

keyed twin plugs
(UL758, style 1385, CSA class 5851, guide 460-1-1)

- Type ZY180L with wire length 350mm
  – for pins 11 (yellow wire) and 10 (red wire)
- Type ZY180R with wire length 350mm
  – for pins 8 (yellow wire) and 9 (red wire)

IXYS reserves the right to change limits, test conditions and dimensions. 20070725a

© 2007 IXYS All rights reserved

# APPENDIX B: EFI Gate Driver [4]

# APPENDIX C: 20kW Laboratory Inverter [3]

## 6 KOBLINGSSKJEMA

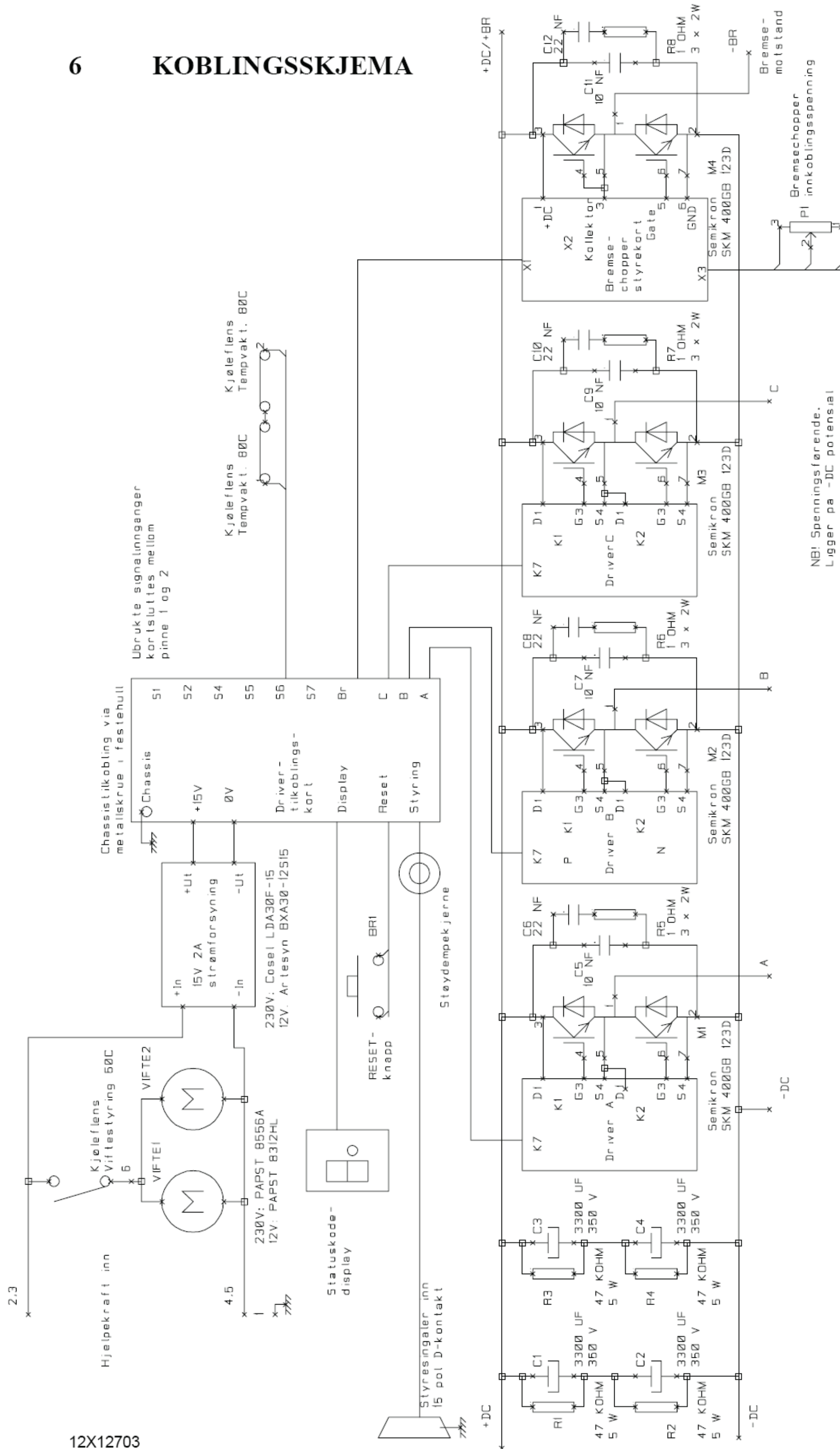


| FIL: Lab vekselretter skjema.scm | |
|---|---|
| UTLEGG REF. | PROSJ: 12x134 03 |
| KONSTRUERT: K.Ljøkelsøy | DATO: 17/4-2002 |
| SINTEF Energiforskning AS | 20 kW lab-vekselretterenhet. Variant 1 Seriekoblet kondensatorbank |

# APPENDIX D: Analog Current Control Board [13]

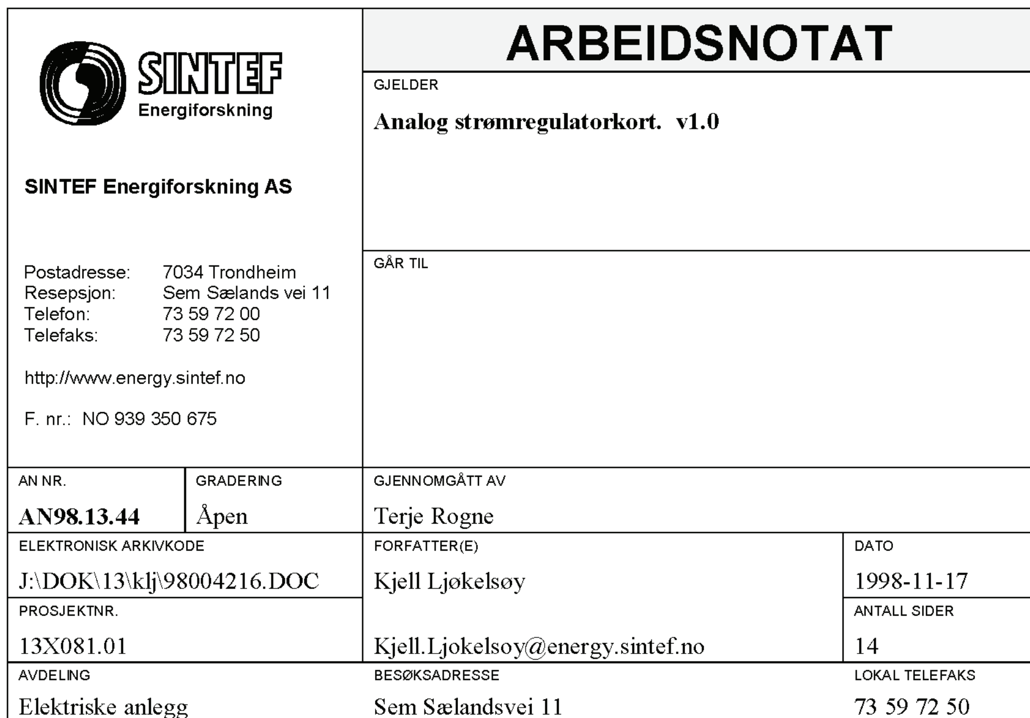

| SINTEF Energiforskning | ARBEIDSNOTAT | |
|---|---|---|
| **SINTEF Energiforskning AS**<br><br>Postadresse: 7034 Trondheim<br>Resepsjon: Sem Sælands vei 11<br>Telefon: 73 59 72 00<br>Telefaks: 73 59 72 50<br><br>http://www.energy.sintef.no<br><br>F. nr.: NO 939 350 675 | GJELDER<br>**Analog strømregulatorkort. v1.0**<br><br>GÅR TIL | |
| AN NR.<br>**AN98.13.44** / GRADERING<br>Åpen | GJENNOMGÅTT AV<br>Terje Rogne | |
| ELEKTRONISK ARKIVKODE<br>J:\DOK\13\klj\98004216.DOC | FORFATTER(E)<br>Kjell Ljøkelsøy | DATO<br>1998-11-17 |
| PROSJEKTNR.<br>13X081.01 | Kjell.Ljokelsoy@energy.sintef.no | ANTALL SIDER<br>14 |
| AVDELING<br>Elektriske anlegg | BESØKSADRESSE<br>Sem Sælandsvei 11 | LOKAL TELEFAKS<br>73 59 72 50 |

***Dokumentet inneholder: Skjema, komponentplassering, deleliste, tilkoblingsliste, kommentarer.***

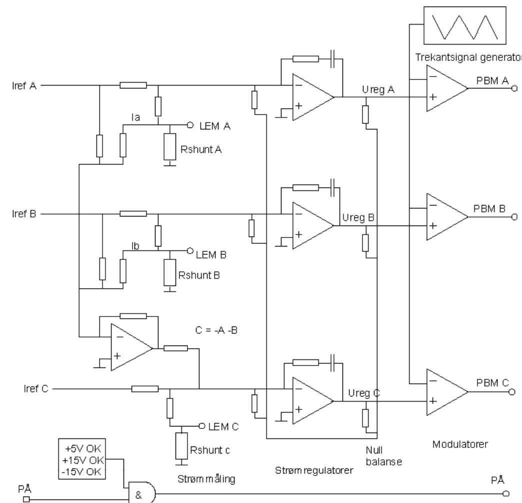


Kortet inneholder tre analoge strømregulatorer med tilhørende pulsbreddemodulatorer, samt shuntmotstander for strømmåling med LEM transfoshunter.

Regulatorinnstillinger og konfigurering bestemmes av et sett med strappinger.

Ved bruk i motorstyringer kan kortet konfigureres slik at kun to strømmålinger og referansesignaler benyttes. En nullpunktsbalanseringskrets sikrer da en midlere utstyring på 50%

Dette notat inneholder prosjektinformasjon og foreløpige resultater, som internt og uformelt underlag for endelig prosjektrapport fra SINTEF Energiforskning AS. SINTEF Energiforskning AS hefter ikke for notatets innhold, og resultater/ data vil i den godkjente prosjektrapport kunne avvike fra notatets opplysninger uten spesielt varsel eller henvisning til dette. Innholdet får ikke gjengis uten skriftlig tillatelse fra SINTEF Energiforskning AS.

## 2 SKJEMA

# 3 KOMPONENTPLASSERING

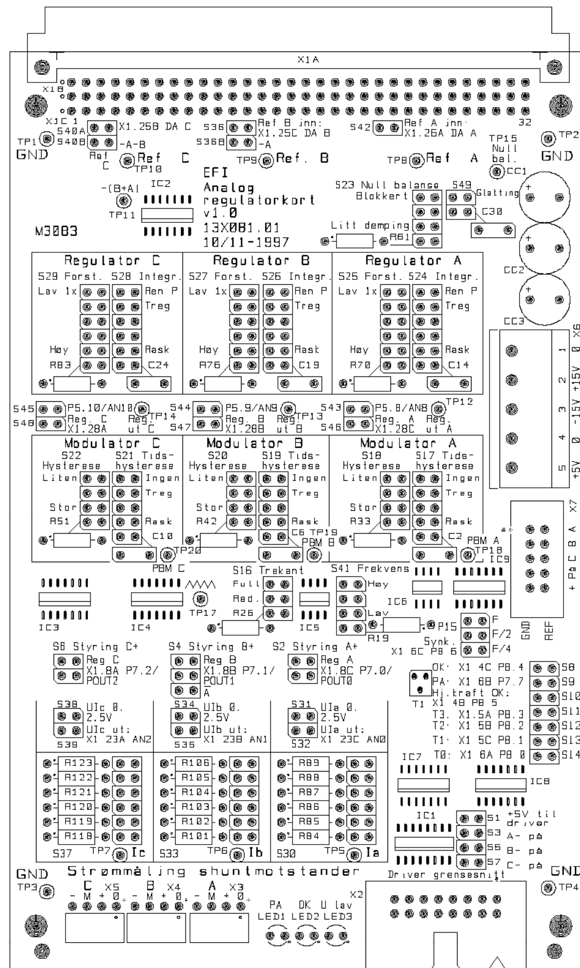


Komponentplassering overside.

# APPENDIX E: Midel 7131 datasheet [22]

## MIDEL® 7131

Technical Datasheet No 2

Dielectric Insulating Fluid
Product Overview

### Product description

MIDEL® 7131 is a dielectric insulating fluid for transformers, tapchangers and electrical control equipment. MIDEL® 7131 conforms to IEC 61099:1992 "Specifications for Unused Synthetic Organic Esters for Electrical Purposes". It is classified as type T1, a halogen-free pentaerythritol ester.

MIDEL® 7131 is an environmentally friendly alternative to conventional transformer fluids, being both readily biodegradable and classified as "non-hazardous to water " according to Umwelt Bundes Amt (UBA) in Germany.

MIDEL® 7131 transformer fluid has a high Fire Point of 322°C and a low net calorific value (<32 MJ/kg) and is therefore classified as a K3 class liquid according to IEC 61100. This, coupled with a slow heating rate due to its high specific heat and thermal conductivity, gives the product its noted resistance to ignition.

MIDEL® is supplied with a low dissolved gas content and moisture level.

### Areas of application

Areas of use include:
- power transformers up to 238 kV/ 135 MVA
- pole-type transformers
- distribution transformers in urban areas and buildings
- tapchangers
- thyristor cooling in power electronics

### Properties

In addition to the properties set out in IEC 61099:1992, MIDEL® 7131 is characterised by:

**Ecological compatibility**
- readily biodegradable
- classified as "non-hazardous to water" according to Umwelt Bundes Amt (UBA) in Germany
- low vapour pressure under operating conditions

**Low acute and chronic toxicity**
- non-toxic to aquatic life
- will not effect the degradation activity of activated sludge in biological sewage treatment plants
- not classified as hazardous.

**Good thermal properties**
- low thermal coefficient of expansion
- heat transfer properties comparable with mineral oil.

**Excellent dielectric properties**
- high breakdown strength
- low dependence of dielectric properties on the effects of moisture.

**Excellent fire resistance**
- high fire point (322°C)
- will not ignite in the event of a major electrical fault and transformer rupture.

MIDEL® 7131 is further noted for its very good lubricating properties. MIDEL® 7131 is compatible with all insulating materials used in conventional transformer construction.

### Retrofilling

MIDEL® 7131 is used to retrofill PCB and mineral oil filled distribution transformers. MIDEL® 7131's thermal characteristics, cooling performance and electrical properties are equivalent to those of mineral oil. This ensures that there is no need to make any alterations to the design of the transformer or to downrate it when retrofilling with MIDEL® 7131.

During retrofill, contamination with other insulating fluids has to be minimised to avoid lowering the fire point or endangering the "non-water hazardous" classification.

### Disposal

For disposal, it is recommended that used MIDEL® 7131 or remains of the insulating fluid be burnt in a suitable installation. Waste disposal code 130309 applies (readily biodegradable insulating and heat transmission oils).

### Regulations

MIDEL® is not subject to the regulations for land, sea and air transport. It does not require labelling in accordance with the Dangerous Substances Regulations.

THINK **RELIABLE** THINK **ENVIRONMENT** THINK **FIRE RESISTANCE** THINK **SAFETY**

www.midel.com

**Characterisation of type T1 transformer ester according to IEC 61099 and DIN VDE 0375**

| Property | Test method | Requirement | MIDEL® 7131 | Unit |
|---|---|---|---|---|
| **Physical properties according to IEC 61099** | | | | |
| Colour | ISO 2211 | max. 200 | 125 | HU |
| Appearance | IEC 61099 9.2 | clear, free from suspended matter and sediment | clear, free from suspended matter and sediment | - |
| Density at 20°C | ISO 3675 | max. 1.00 | 0.97 | kg/dm³ |
| Kinematic viscosity at 40°C | ASTM D 445 | max. 35.0 | 28 | mm²/s |
| Kinematic viscosity at -20°C | | max. 3000 | 1400 | mm²/s |
| Flash point | ISO 2592 | min. 250 | 275 | °C |
| Fire point | ISO 2592 | min. 300 | 322 | °C |
| Refractive index at 20°C | ISO 5661 | ± 0.01 of the value given by the manufacturer | 1.4555 | - |
| Pour point | ISO 3016 | Max. -45 | -60 | °C |
| Crystallisation | IEC 61099 9.9 | No crystals | No crystals | - |
| Velocity of sound in Midel at 20°C | - | - | 1385 | m/s |
| **Chemical properties according to IEC 61099** | | | | |
| Water content | IEC 60814 | max. 200 | 50 | mg/kg |
| Neutralisation | IEC 61099 9.11 | max. 0.03 | <0.03 | mg KOH/g |
| Oxidation stability | IEC 61125 | | | |
| - Total acid content | | max. 0.3 | 0.01 | mg KOH/g |
| - Total sludge content | | max. 0.01 | 0 | % mass |
| Net calorific value | ASTM D 240-02 | <32 | 31.6 | MJ/kg |
| **Dielectrical properties according to IEC 61099** | | | | |
| Breakdown voltage | IEC 60156 | min. 45 | >75 | kV |
| Dielectric dissipation factor Tan δ at 90°C and 50 Hz | IEC 60247 | max. 0.03 | <0.03 | - |
| Volume resistivity DC at 90°C | IEC 60247 | min. 2 | >50 | Gohm-m |

Data quoted above are typical values. It is the policy of M&I Materials Ltd to continually improve product quality. The published values above may be altered without notice and do not constitute a specification.

THINK **RELIABLE** THINK **ENVIRONMENT** THINK **FIRE RESISTANCE** THINK **SAFETY**

Any recommendation or suggestion relating to the use, storage, handling or properties of the products supplied by M&I Materials Ltd either in sales and technical literature or in response to a specific enquiry or otherwise is given in good faith but it is for the customer to satisfy itself of the suitability of the product for its own particular purposes. ® Registered Trade Mark
www.midel.com

September 2007